MASTER THESIS

MULTI-BEAM LIGHT-MATTER INTERACTIONS IN EPSILON-NEAR-ZERO MATERIALS AND NANOSCALE METASURFACES

Author:
THENG LOO LIM

Supervisor:
PROFESSOR ROBERT W.BOYD

A thesis submitted in fulfillment of the requirements for the degree of Master of Science degree in Physics

in the

DEPARTMENT OF PHYSICS

JANUARY 16, 2023

Declaration of Authorship

I, Theng Loo LIM, declared that this thesis was all written by myself. The contributors to this thesis are:

For the theory developed for two-beam coupling described in Chapter 2, The work was supervised by Prof. Robert Boyd, with direct oversight and direction provided by Dr. Zahirul Alam and Dr. Jeremy Upham. The simulation and derivation were jointly worked on with Mr. Yaswant Vaddi.

In Chapter 3, I conducted the corresponding experiments for Chapter 2 jointly with Mr. Yaswant Vaddi and Dr. Yiyu Zhou. The setup development was supervised by Dr. Zahirul Alam and Prof. Robert Boyd.

For Chapter 4, the experimental setup for metasurface measurement was built jointly with Mr. M. Saad Bin-Alam and Mr. Yaswant Vaddi. I have developed a simulation method for metasurface design jointly with Dr. Orad Reshef and Prof. Mikko J. Huttunen. The sample fabrication was done by Dr. Orad Reshef. This work was supervised by Dr. Jeremy Upham, Prof. Ksenia Dolgaleva, and Prof. Robert Boyd.

Chapter 5 contains the corresponding manuscript for the work described in Chapter 4. The involved authors are listed in the manuscript.

Signed:

Date:

Abstract

Light-matter interactions are essential for the development of many modern technologies and for fundamental science. Hence, many recent efforts have focused on understanding light-matter interaction in exotic classes of materials, particularly in subwavelength (nanometre scale) regimes. This Master's thesis focuses on two different types of materials whose interaction length is typically in the nanoscale. First, we studied and observed the energy transfer between two ultrashort beam pulses in the epsilon-near-zero (ENZ) spectral range of a material, classified where the real part of the material's electric permittivity has a magnitude much less than 1. Typically, such energy transfer in ordinary materials (such as fused silica) requires different wavelengths of both beams interacting in the material. However, ENZ materials have an unprecedentedly high optical nonlinearity, leading to self-manifesting energy transfer. This self-manifesting effect occurs in ENZ material due to the effective frequency shift known as adiabatic frequency conversion (AFC) caused by a significant change of refractive index from its large optical nonlinearity. Second, we studied a class of materials known as metasurfaces, which are built from an array of artificial engineered nano-antennas. Metasurfaces can enable custom wavefront control or the engineering of coupling to designated surface modes, which is not possible for naturally occurring optical surfaces. In this thesis, we developed a design scheme for constructing a metasurface that generates multiple lattice resonances at desired wavelengths. Such a design scheme is possible because we arranged the nano-antennas using Fourier analysis. This flexible scheme produces a metasurface design directly from the desired distribution of resonances.

Acknowledgements

Throughout my graduate studies, I would like to first express my most significant appreciation to my supervisor, Prof. Robert W. Boyd, a world-leading photonics expert. He has always been accommodating in developing my research career and establishing an excellent research group at the University of Ottawa, where I have a chance to work with top research scientists.

For example, our group manager, Dr. Jeremy Upham, has always given me valuable advice, which helped me make significant progress. Furthermore, Dr. Orad Reshef and Dr. M. Zahirul Alam, some of the most brilliant people I have ever met, have educated me on tackling cutting-edge research problems and trained me to generate feasible research ideas. I would like to extend my sincere thanks to my colleagues, Yaswant Vaddi, Saad-bin Alam, Cheng Li, Dr. Lin Cheng, Dr. Rasoul Alaee, Dr. Girish Kulkarni, Mahdieh Jabbari, Mohammad Karimi, Sisira Suresh, and Dr. Yiyu Zhou, who has been very important during my graduate life. I am incredibly grateful to have you.

I would also like to acknowledge the administrative support from Mr. Hugo Begin and Ms. Gloria Kaneza.

Finally, I would like to extend my deepest gratitude to my family in Malaysia. My achievement would not be possible without their patience and love.

Contents

List of Figures

List of Tables

List of Abbreviations

AFC	Adiabatic Frequency Conversion
BIC	Bound States in Continuum
CMOS	Complementary Metal–Oxide–Semiconductor
DDA	Discrete Dipole Approximation
DFWM	Degenerate Four Wave Mixing
ENZ	Epsilon-Near-Zero
FDTD	Finite-Difference Time-Domain
FLR	Fourier Lattice Resonance
FP	Fabry-Perot
FT	Fourier Transform
GVD	Group Velocity Dispersion
ITO	Indium Tin Oxide
LSA	Lattice Sum Approach
LSPR	Localized Surface Plasmon Resonance
OPA	Optical Parametric Amplifier
SLR	Surface Lattice Resonance
SPM	Self Phase Modulation
WNA	Weak Nonlinear Approximation
XPM	Cross Phase Modulation

Chapter 1

Introduction

In general, I am interested in studying light-matter interactions in classes of materials that exhibit unconventional optical properties. In this thesis, I study two different classes of materials: epsilon-near-zero (ENZ) thin films and metasurfaces. I discuss their particular properties of interest that lend themselves to particular types of efficient light manipulation. Section 1.1 is a brief introductions of ENZ materials, while section 1.2 is an introduction to plasmonic metasurfaces. The structure of this thesis is stated in the last section of this chapter.

1.1 Enhancing optical nonlinearity using ENZ material

Nonlinear optics is a sub-field of Laser physics, it studies what phenomena occur in a nonlinear optical medium when intense light field is applied into the system.

To mathematically formulate the optical nonlinear response of media, we first begin with Maxwell's equations. Consider a dispersion-less, isotropic, and nonmagnetic medium without free charges or free current. Maxwell's equations can thus be written as:

$$\nabla \cdot \tilde{\mathbf{D}} = 0, \tag{1.1}$$

$$\nabla \cdot \tilde{\mathbf{B}} = 0, \tag{1.2}$$

$$\nabla \times \tilde{\mathbf{E}} = -\frac{\partial \tilde{\mathbf{B}}}{\partial t}, \tag{1.3}$$

$$\nabla \times \tilde{\mathbf{H}} = \frac{\partial \tilde{\mathbf{D}}}{\partial t}, \tag{1.4}$$

where $\tilde{\mathbf{B}}$ is the magnetic density flux, since the medium is nonmagnetic, then $\tilde{\mathbf{B}} = \mu_0 \tilde{\mathbf{H}}$. Furthermore, the displacement field, $\tilde{\mathbf{D}}$, takes into account both the external electric field, $\tilde{\mathbf{E}}$, and the material's dipole moment per volume (or polarization vector), $\tilde{\mathbf{P}}$, that is induced by $\tilde{\mathbf{E}}$:

$$\tilde{\mathbf{D}} = \epsilon_0 \tilde{\mathbf{E}} + \tilde{\mathbf{P}}, \tag{1.5}$$

To consider the nonlinear responses of the material, we can express $\tilde{\mathbf{P}}$ as:

$$\tilde{\mathbf{P}} = \epsilon_0 [\chi^{(1)} \tilde{\mathbf{E}} + \chi^{(2)} \tilde{\mathbf{E}}^2 + \chi^{(3)} \tilde{\mathbf{E}}^3 + \ldots], \tag{1.6}$$

The linear optical response of a material is described by the $\chi^{(1)}$ term, whereas higher-order terms such as $\chi^{(2)}$, and $\chi^{(3)}$ are considered to be as the nonlinear optical responses of material. Now, we substitute Eq. 1.4 onto Eq. 1.3, and using vector calculus identity, one can express the wave equation in a medium as:

$$\nabla^2\tilde{\mathbf{E}} - \frac{1}{c^2}\frac{\partial^2}{\partial t^2}\tilde{\mathbf{E}} = \frac{1}{\epsilon_0 c^2}\frac{\partial^2\tilde{\mathbf{P}}}{\partial t^2}, \tag{1.7}$$

or it can be written in the more intuitive alternative form:

$$\nabla^2\tilde{\mathbf{E}} - \frac{\epsilon^{(1)}}{c^2}\frac{\partial^2}{\partial t^2}\tilde{\mathbf{E}} = \frac{1}{\epsilon_0 c^2}\frac{\partial^2[\chi^{(2)}\tilde{\mathbf{E}}^2 + \tilde{\chi}^{(3)}\tilde{\mathbf{E}}^3 + \ldots]}{\partial t^2} = \frac{1}{\epsilon_0 c^2}\frac{\partial^2\tilde{\mathbf{P}}^{NL}}{\partial t^2}. \tag{1.8}$$

where $\epsilon^{(1)} = 1 + \chi^{(1)}$ is first order (linear) relative permittivity, and $\tilde{P}^{NL}$ is nonlinear optical polarization of the material. Thus, Eq. 1.8 can be treated as a driven wave equation; the nonlinear optical reactions of the material act as a source term. From this equation, one can realize that the nonlinear optical responses modify the optical properties of the material if a high laser intensity is applied to a material.

In this section, we study the change of the refractive index due to the nonlinear optical response of a material to high laser intensity being pumped into the material. Let us consider when a linear polarized light beam propagates through a material that connects with a source that applies a static electric field, the light beam experiences an elliptical change of polarization and refractive index due to the static-electric-field-induced birefringence in the material. This modification is known as the DC Kerr effect, and the strength of this modification depends quadratically on the static electric field [19, 20]. Let's consider another scheme: if an intense beam of light is applied, the electric field of the beam itself induces a change of refractive index in the material without a static electric field [18, 21]. This effect of self-modification of the light beam is known as the optical Kerr effect, and its strength depends on the intensity of the light beam and third-order susceptibility $\chi^{(3)}$ of a material.

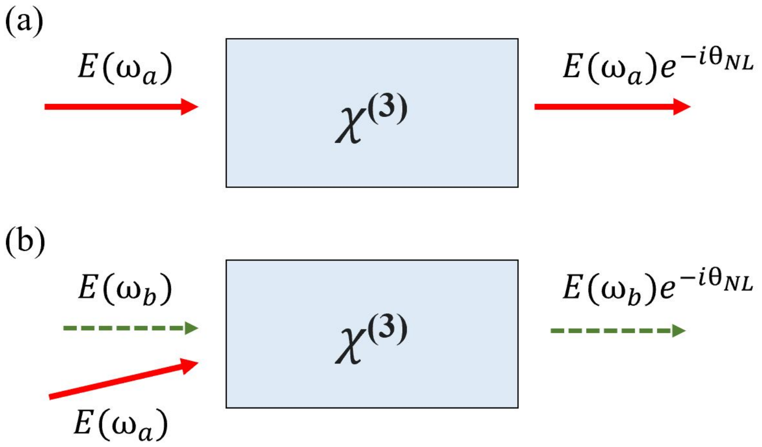

FIGURE 1.1: Schematic drawings of (a) self-phase modulation (SPM), and (b) cross-phase modulation (XPM). The red arrow indicates a strong laser beam, and the green dot arrow indicates a weak laser beam.

Table 1.1: Nonlinear refractive index n_2 of typical materials [18]

Materials	n_0	$\chi(3)$ (m^2/V^2)	n_2 (cm^2/W)
Fused silica	1.47	2.5×10^{-22}	3.2×10^{-16}
BK-7	1.52	2.8×10^{-22}	3.4×10^{-16}
GaAs	3.47	1.4×10^{-18}	3.3×10^{-13}
Ge	4.0	5.6×10^{-19}	9.9×10^{-14}
Si	3.4	2.8×10^{-18}	2.7×10^{-14}
ZnSe	2.7	6.2×10^{-20}	3.0×10^{-14}

One can describe the changes of the refractive index of a material due to the optical Kerr effect mathematically by considering the third-order nonlinear contribution of $\tilde{\mathbf{P}}^{NL}$:

$$\tilde{\mathbf{P}} = \epsilon_0\chi^{(1)}\tilde{\mathbf{E}} + 3\epsilon_0\chi^{(3)}|\tilde{\mathbf{E}}|^2\tilde{\mathbf{E}} = \epsilon_0\chi_{eff}\tilde{\mathbf{E}}, \tag{1.9}$$

we recall that $n = \sqrt{1+\chi_{eff}}$, using this relationship we can show that:

$$n = \sqrt{1+\chi_{eff}} = \sqrt{1+\epsilon_0\chi^{(1)} + 3\epsilon_0\chi^{(3)}|\tilde{\mathbf{E}}|^2}, \tag{1.10}$$

we assume that the nonlinear contribution is small compared to the linear contribution, then we can simplify this equation to:

$$n \approx n_o + \frac{3\chi^{(3)}|\tilde{\mathbf{E}}|^2}{2n_o}, \tag{1.11}$$

By substituting the light intensity equation ($I = 2n_o\epsilon c|\tilde{\mathbf{E}}|^2$), we obtain the change of refractive index due to the optical Kerr effect:

$$n = n_0 + \Delta n = n_0 + n_2 I, \tag{1.12}$$

where Δn is the change of refractive index, n_0 is linear refractive index, n_2 is nonlinear refractive index, and I is intensity of light beam. Assuming that the material is nonmagnetic ($n = \sqrt{\epsilon}$), n_2 can be expressed as:

$$n_2 = \frac{3}{4n_0^2\epsilon_0 c}\chi^{(3)} = \frac{3}{4(Re[\epsilon] + iIm[\epsilon])\epsilon_0 c}\chi^{(3)}. \tag{1.13}$$

where ϵ is the electric permittivity of the material. The changes of the refractive index, Δn caused by the nonlinear optical effect have many significant consequences. For example, Δn produces phase change on the laser beam itself, leading to a change of the frequency spectrum; this effect is known as self-phase modulation (SPM) (Fig. 1.1(a)). Also, a weak laser beam (probe beam) will experience a phase shift when another intense laser beam (pump beam) interacts with the sample within the duration of time response of the material; this modulation is referred to as cross-phase modulation (XPM) and is shown in (Fig. 1.1(b)). These and other self-action effects are under intensive studies in the photonics community, such as the self-focusing effect, self-trapping effect, and filamentation [18].

These light-induced effects have many important applications. For instance, SPM and XPM must be mitigated for high throughout optical communication through optical fibre networks, waveguides, and other photonic devices. Conversely, ultrafast laser system development relies on these self-actions effects. Also, understanding optical soliton generation, which is highly dependent on light-induced nonlinear effects, is essential to developing efficient optical communication.

In many cases, nonlinear optics applications suffer two problems: the first problem is that conventional materials have rather low n_2 [18] (Table 1.1). For example, n_2 of fused silica is about 3.2×10^{-16} cm^2/W and the damage threshold is about 2J/cm^2. Therefore, when the input laser intensity is at the damage threshold of fused silica, the corresponding Δn is only 0.006, which value is much smaller than its linear refractive index (n_0= 1.47). Figure 1.2 (a) shows how Δn is limited by damage threshold. For the second problem, assume both the damage threshold of material and the input laser intensity are very high, such that one does not need to worry about damaging the material; in this situation, the saturation behaviour of material usually limits the Δn to saturated value Δn_{max} (Fig. 1.2 (b)).

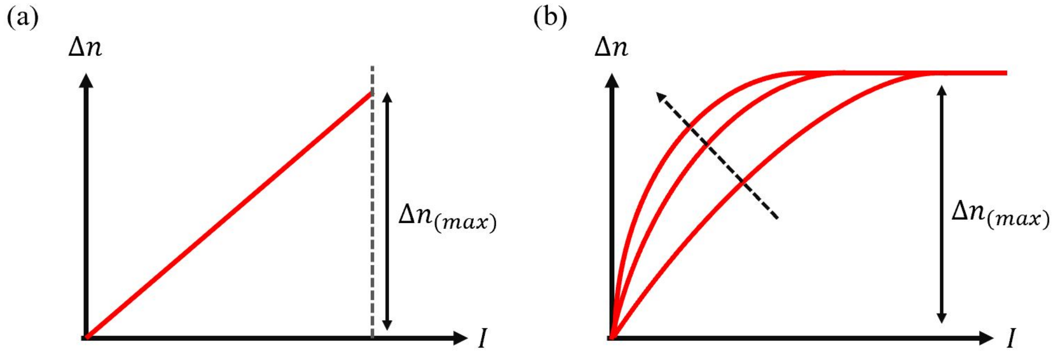

FIGURE 1.2: Limitation of changes in refractive index, Δn. (a) Δn as a function of input laser intensity I. Δn_{max} indicates that the maximum Δn can be achieved before the intensity reached to damage threshold of the material. (b) This case shows the limitation of Δn caused by the saturation behaviour of the material. The dashed arrow shows the effects of the field-enhancement mechanisms, which causes Δn increases more rapidly with respect to I. However, these effects do not increase Δn_{max}. Note: Δn is small in both cases.

Therefore, the nonlinear optical response is usually considered a weak-perturbation to the linear response, and the development of nonlinear photonics devices reached a bottle-neck due to these problems. Searching for materials with large optical nonlinearities has been a long-standing goal in this field of research. Recently, a new class of materials, known as epsilon-near-zero (ENZ) materials, have been shown to exhibit exceptionally high optical nonlinearities due to their vanishingly small permittivity [7, 22]. This reason can be understood as follows: if we consider Eq. 1.13, as the permittivity is close to zero, the $Re[n_0]$ also approaches zero since $n = \sqrt{\epsilon}$. Consequently, the real part of n_2 will diverge as its denominator approaches zero, and we then achieve unprecedentedly high nonlinearities which are not possible in the conventional materials stated in Table 1.1. We will further explain how one can physically obtain this condition in transparent metal oxides in Chapter 2.

1.2 Efficient light manipulation using metasurfaces

Many modern technology developments such as the cellphone, optical fibre, the personal computer, the camera, and the laser can attribute at least part of functionality to light-matter interaction. However, as the technologies relying on light are advancing, we are reaching a bottleneck where traditional optical elements are unable to improve due to their low efficiency of light-matter coupling and inefficient control of light. Therefore, much research effort has been made to develop a new class of materials, the so-called metamaterial [23]. This type of material is artificially constructed with patterns of multiple materials such as metals or dielectrics, with the size of the patterns usually being smaller or comparable to the wavelength of light. Such materials can enable novel and efficient light manipulation that conventional materials can not achieve. For example, metamaterials have achieved negative refraction [24], an invisibility cloak in the microwave region [25], and other applications [26, 27, 28].

This thesis is interested in a two-dimensional (2D) version of the metamaterial. It is referred to as a metasurface [29] and in our case this class of material consists of 2D arrays of sub-wavelength light scatterers. Metasurfaces enable efficient wavefront control by changing the spatial shapes of the scatterers [12], the spacing and the patterning of the structure [13], and using different materials [29]. Figure 1.3 shows the schematic drawing of a typical metasurface [1].

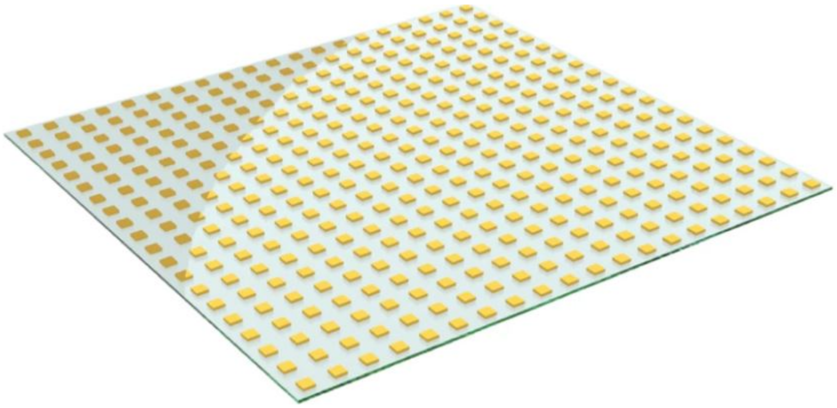

Figure 1.3: The schematic drawing of a typical metasurface. Each gold square represents a rectangular gold nanoparticle, which is on the order of 100 nm. Nanoparticles are embedded in a substrate, which typically made of glass. Image adapted from [1] with permission.

Since metasurfaces are usually a few orders of magnitude thinner than conventional optical elements, they can form more compact photonic elements such as optical filters, lenses, and polarizers.

Metasurfaces can be divided into two broad groups. The first one is all-dielectric metasurfaces. This group is mainly made of insulators or semiconductors. The main advantages of using all-dielectric metasurface are that the nonradiative loss of the materials is typically low; thus, one can develop low-loss photonic devices such as a compact lens that can replace traditional bulk lens in certain applications (Fig. 1.4c [4]). Other important applications for all-dielectric metasurfaces include boosting second harmonic efficiency [2] (Fig. 1.4a) and developing ultra-low-loss lasers [3] (Fig. 1.4b).

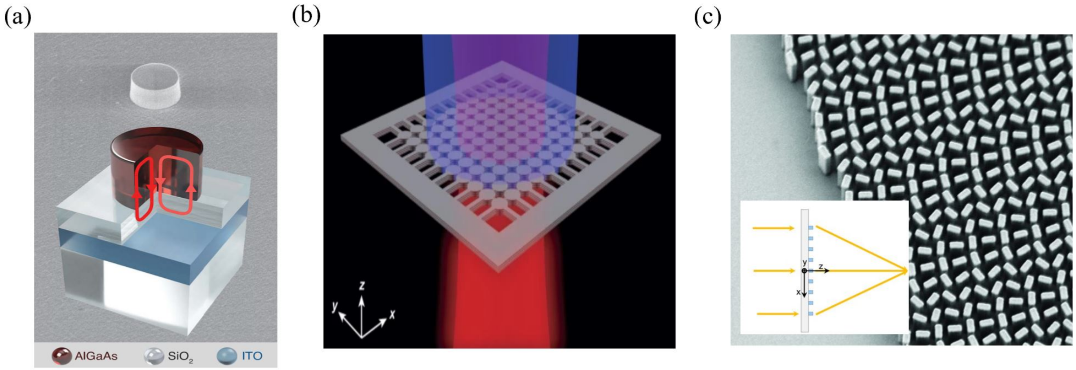

FIGURE 1.4: The examples of dielectric metasurfaces and their potential applications in boosting nonlinearity, lasing, and developing compact lens. Image adapted from [2, 3, 4] with permissions.

The second group is made of conductive materials such as gold or silver that can support plasmonic responses. Compared to dielectric materials, plasmonic materials have a superior scattering coefficient and exhibit larger field enhancement. These properties can easily be tuned by changing the size and the shape of the nanoparticle. With this property, many works have demonstrated efficient wavefront control by adjusting the size of nanoparticles in a single cell, leading to Snell's law generalization (Fig. 1.5a) [5, 6]. Furthermore, vortex beam generation is possible in a plasmonic thin film by changing the geometry of the nanoparticles (Fig. 1.5b). Furthermore, plasmonic metasurfaces are also an important platform for biosensing due to the high sensitivity of plasmon resonances. Many recent works have been using plasmonic metasurface to detect the SARS-CoV-2 virus [30].

In this thesis, we are focused on developing plasmonic metasurfaces that allow us to generate multiple optical resonances. Although we only investigate in plasmonic metasurfaces, our work can also apply to other metasurfaces. This topic will be discussed in Chapter 4 and 5.

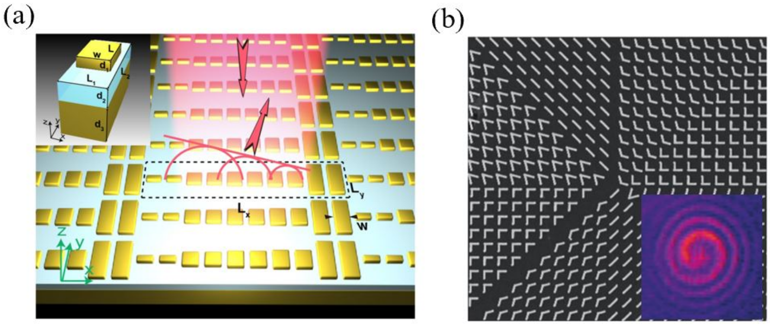

FIGURE 1.5: The examples of dielectric metasurfaces and their potential applications in generalizing Snell's law, and generating vortex beam. Images adapted from [5, 6] with permissions.

1.3 The structure of the thesis

In this thesis, we discuss two different topics that are trying to develop more efficient light-matter interaction at the nanoscale. The thesis consists of nine chapters, including this introduction.

Chapter 2 discusses the physical origin of a large optical nonlinearity induced by an ENZ material. Due to the high nonlinearity and ultrafast responses of an ENZ material, a strong time-varying effect can be observed in such material. We show recent research in this field, then, we discuss the passive energy transfer between two laser beams in a nonlinear media and introduce our proposal that self-manifested energy transfer is possible due to the strong time-varying effect in an ENZ material. Chapter 3 describes our experimental verification of the energy transfer process and discusses these results.

In Chapter 4, we introduce the current state of plasmonic metasurface research. We explain different plasmon resonance modes and describe the methods that induce and characterize these resonance modes. Then, we suggest a design scheme that enables us to generate and manipulate multiple plasmon resonance modes, and how their resonance wavelengths can be flexibly placed in a single metasurface. Also, we show the detailed fabrication and experimental setup. Chapter 5 consists of our published manuscript that demonstrates our proposed idea stated in Chapter 4.

Chapter 6 summarizes our work and suggests follow-up research directions. Appendix A shows the mathematical derivation of the energy transfer process in Chapter 2. Furthermore, we discuss the simulation tools we used for designing a metasurface in Appendice B and C.

Chapter 2

Two-Beam Coupling at Epsilon-Near-Zero Wavelengths

2.1 Observation of a large optical nonlinearity in ITO at ENZ wavelengths

The electrical permittivity of a material, $\epsilon(\omega)$, is a complex light-frequency-dependent quantity that describes light-matter interaction in the material. The real part of $\epsilon(\omega)$ depicts the polarization induced by the incident light field, whereas the imaginary part of $\epsilon(\omega)$ characterizes optical-induced losses while polarizing, which generally arises from interband transitions or electron-phonon interactions. The $\epsilon(\omega)$ over the spectrum of interest of mainly conducting materials can be well-described by the Drude model [31], which describes free electrons gas motion in metals with applied electric field:

$$\varepsilon(\omega) = \varepsilon_\infty - \frac{\omega_p^2}{\omega^2 + i\omega\gamma}, \tag{2.1}$$

where γ is the scattering rate of the material (or loss), ω is frequency of input light beam, ϵ_∞ is background permittivity, and ω_p is plasma frequency:

$$\omega_p = \sqrt{\frac{n_\mathrm{e} e^2}{m^* \varepsilon_0}}. \tag{2.2}$$

the plasma frequency is an important optical property of a material. At this frequency, the free charged carriers rapidly resonate with respect to their host ions. As expressed in Eq. 2.2, this quantity depends on the charged carriers density, n_e, and the effective mass of the charged carriers, m^*. Let us consider a material whose optical property can be well-described by the Drude model: a highly-doped semiconductor, indium tin oxide (ITO). Figure 2.1 shows the electrical permittivity of ITO with respect to incident light wavelength, λ. As incident light wavelength is getting closer to the plasma wavelength of ITO (~1240 nm), the electric permittivity of ITO is approximately zero. At this range of frequencies, the free charged carriers oscillate rapidly with the driving frequency of the light, which minimizes the resistance, resulting near-zero permittivity. Therefore, this frequency range is known as the epsilon-near-zero (ENZ) regime; it plays an important role in enhancing nonlinear optical response of ITO.

Specifically, the linear refractive index, n_0, depends on the electric permittivity: $n = \sqrt{\epsilon(\omega)}$. Thus, n_0 is approximately zero when the light frequency is in the ENZ range. This implies that n_2 will diverge according to Eq. 1.13, thus leading to extremely large optical nonlinearity. In a previous work [7], our group performed a

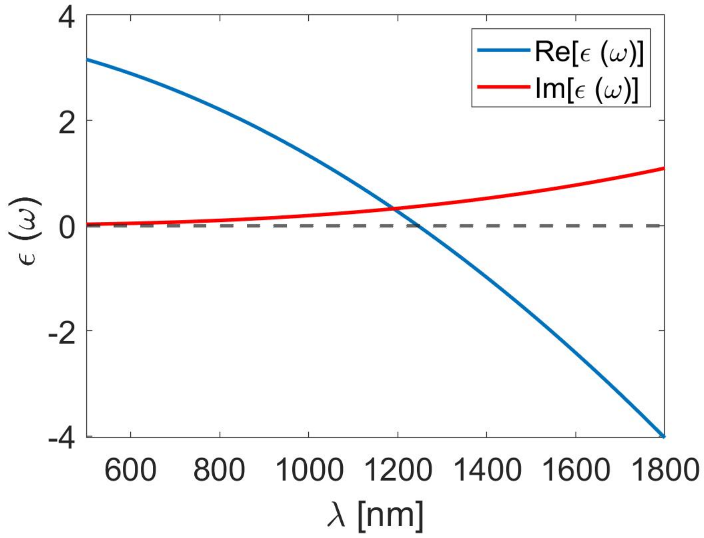

FIGURE 2.1: Dielectric function $\epsilon(\omega)$ of ITO film (thickness: 310nm). The real part of $\epsilon(\omega)$ is approximately zero with incident light wavelength is 1240 nm. At this wavelength, the imaginary part of $\epsilon(\omega)$ is about 0.4.

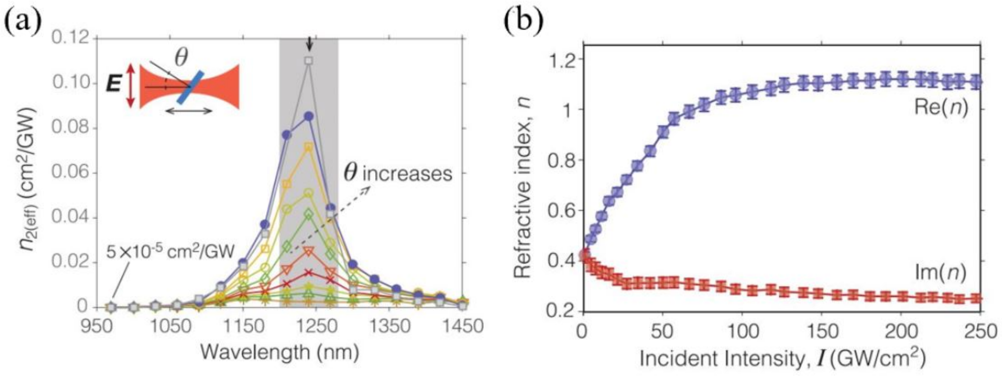

FIGURE 2.2: Nonlinear response of ITO. (a) The measured n_2 of ITO as a function of incident laser wavelength, different curves corresponds to measurements with different angles of incidence. The shaded region indicates the ENZ regions of the ITO sample, and the applied laser intensity is 66 GW/cm^2. (b) The real and imaginary parts of the refractive index as a function of incident laser intensity, the laser wavelength is 1240 nm and $\theta = 30^o$. Image adapted from [7] with permission.

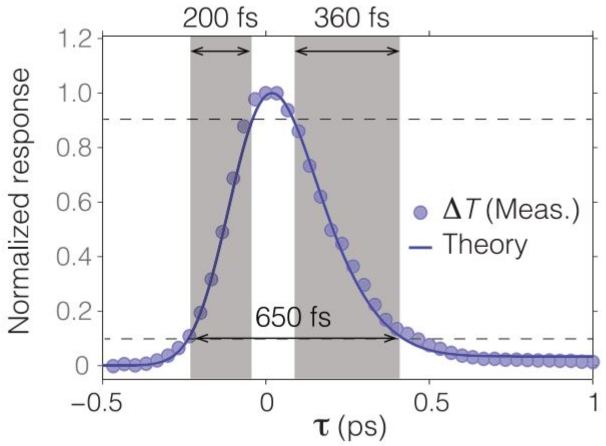

FIGURE 2.3: Time response of the ITO sample. The normalized transmittance of the ITO sample as a function of probe pulse laser delay time. Image adapted from [7] with permission.

standard Z-scan measurement to determine n_2 of ITO; they show that the n_2 is dramatically increasing when the incident laser wavelength is at ENZ wavelength of ITO (Fig. 2.2a). Strikingly, the change of the refractive index, Δn_{ITO}, is a dominating factor in the optical properties of ITO. Figure 2.2b shows the real and imaginary parts of the refractive index of ITO as a function of incident laser intensity at the ENZ wavelength, when the angle of incidence is close to 60^o. In this figure, we observe that the Re(Δn_{ITO}) started saturating when the laser intensity was higher than 100 GW/cm^2, and that the highest Re(Δn_{ITO}) obtained is about 0.72. This value is unprecedentedly large; it is about 170% of its linear refractive index. In other words, the nonlinear effect dominates the optical properties of ITO, which is impossible to observe in typical materials such as fused silica [18].

The other crucial optical feature of ITO in the ENZ regime is the ultra-fast temporal response of this nonlinear index change. Figure 2.3 shows the transmission of ITO as a function of delay time, τ, obtained by performing the pump-probe experiment (such experiment will be explained in Chapter 3). As we can see, the rise time of ITO took ∼200 fs, and the recovery time is within 360 fs. Such ultrafast response will not only be important for applications, such as all-optical modulation, but could also be a crucial platform for studying time-varying medium, which will be explained in the next section.

2.2 Adiabatic frequency conversion at ENZ wavelengths

As shown in the previous section, the large change of nonlinearity arises in a sub-picosecond time scale in this particular ENZ material. This property of ITO provides a new platform for researchers to study the effect of time refraction [8].

The concept of time refraction can be explained as follows (we follow closely to Ref. [8]): assuming a laser pulse with a wavelength of λ_1 and refractive index of n_1 propagates through a dispersion-less medium with a refractive index of n_2 (Fig. 2.4a). This leads to a change in wavevector of laser beam after propagating through the spatial boundary, and it can be described as $n_1\lambda_1 = n_2\lambda_2$. Let's consider the temporal

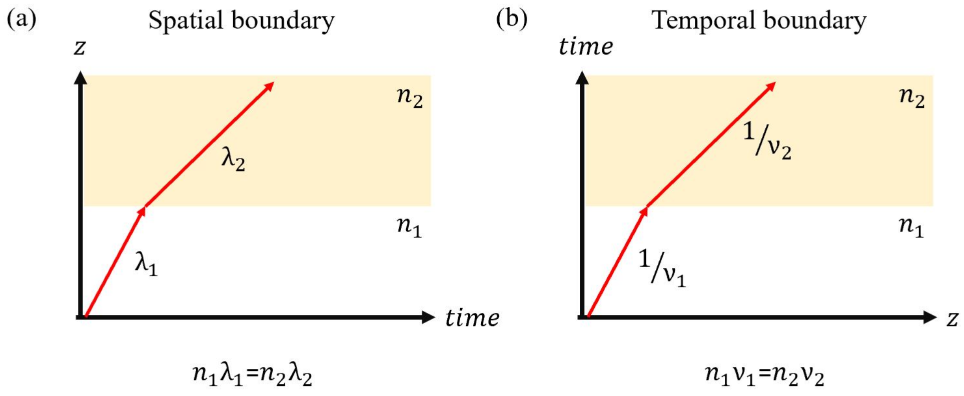

FIGURE 2.4: The time refraction. (a) When a light beam (red arrow) propagates through a spatial boundary defined by a refractive index change from n_1 to n_2, the light beam will experience a change in the wavevector. This effect can be described by $n_1\lambda_1 = n_2\lambda_2$. (b) As a light beam travels through a refractive index boundary defined in time, the light beam will experience a time-refraction effect described by $n_1\nu_1 = n_2\nu_2$.

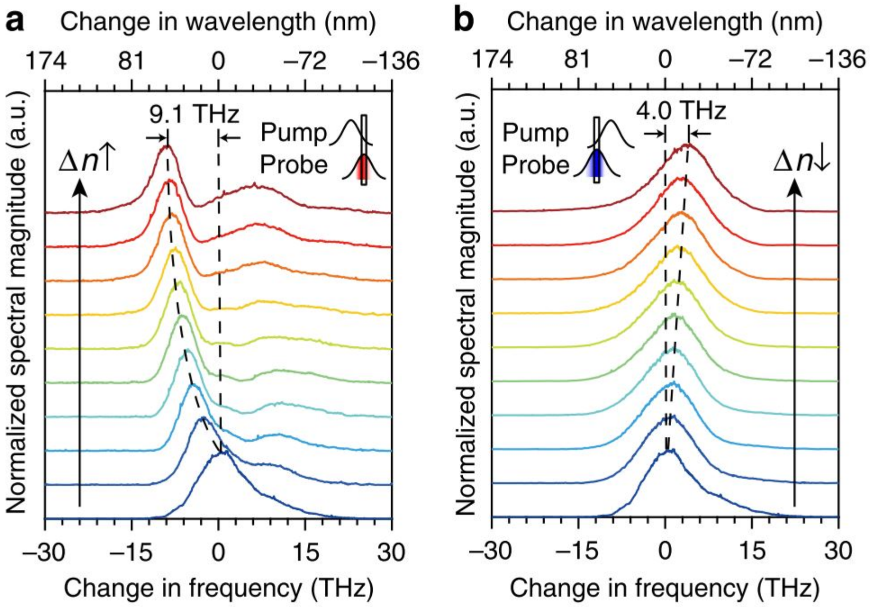

FIGURE 2.5: The adiabatic frequency shift from an ENZ material. (a and b) The frequency red-shifts (blue-shifts) are observed in a probe beam spectrum at the delay time,t_d, of -60 fs (60 fs). The incident laser wavelength is 1235 nm. The insets illustrate the pump and probe beams' relative timing. The top-most spectra to the bottom-most spectra in both panels indicate the change of the highest pump intensity (Δn) to zero pump intensity (Δn). Image adapted from [8].

boundary induced by the refractive index change in the time domain (Fig. 2.4b). The laser beam will experience a frequency shift due to the time translation symmetry breaking since the wavevector is unchanged while the refractive index is changing. Using the dispersion relation $c/\nu = n\lambda$, one can express the change of frequency as $n_1\nu_1 = n_2\nu_2 = (n_1 + \Delta n) * (\nu_1 + \Delta\nu)$, where Δn is the change of refractive index and $\Delta\nu$ is the change of frequency. If we consider a conventional material like silicon, the effect of time refraction is insignificant since n is small compared to the linear refractive index (typically $\sim 10^{-3}$). However, this effect is large in ITO since its Δn is close to unity at ENZ wavelengths. This frequency shift induced by time refraction is referred to as adiabatic frequency conversion (AFC).

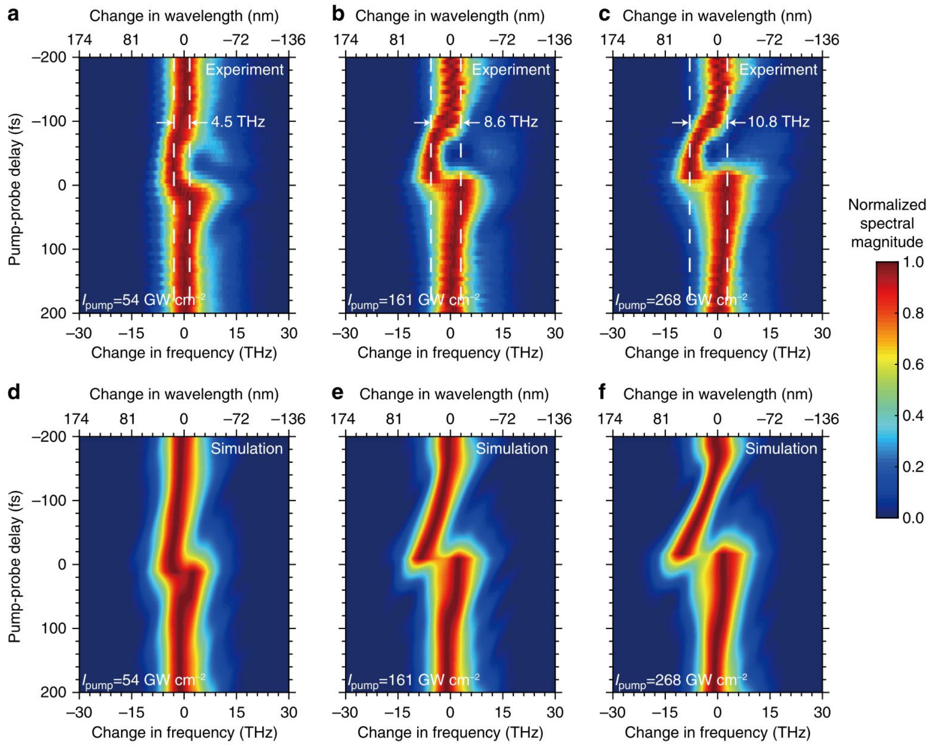

FIGURE 2.6: Experimental and calculated probe spectra at the incident wavelength of 1235 nm. (a–c) Experimental probe spectra with normalized magnitude with respect to the pump-probe delay time. These three sub-figures correspond to different pump intensities. (d–f) The corresponding calculated probe spectra using the nonlinear Schrödinger equation. The experimental results are in excellent agreement with the calculations. Image adapted from [8].

To observe AFC, our group performed a set of degenerate pump-probe experiments (see Chapter 3 for more information) on ITO with a thickness of 620 nm, and the incident laser wavelength is 1235 nm (ENZ wavelength of the sample). Figure 2.6 shows the experimental results of the probe pulse transmission spectrum. When a weak probe pulse arrived in the sample with a delay time of 60 fs before the strong pump pulse, the influence from the pump pulse started to induce Δn, as the pump pulse intensity increases, we observe that the frequency red-shifted accordingly. On the other hand, when the pump pulse arrives before the probe pulse with the same delay time (t_d = -60 fs), the probe spectrum is blue-shifted as the pump pulse's intensity increases. These experiments have experimentally demonstrated the effect of

AFC on an ENZ material.

In Fig. 2.6, the top three sub-figures shows the probe spectrum from the pump-probe experiments as a function of change in frequency (x-axis) and the delay time t_d (y-axis), these three sub-figures correspond to three different pump pulse intensities (I_{pump}= 54 GW/cm^2, 161 GW/cm^2, and 268 GW/cm^2). To theoretically predict AFC, the authors modelled the effect using the nonlinear Schrodinger equation. The bottom three sub-figures in Fig. 2.6 illustrate the calculated probe spectrum from the nonlinear Schrodinger equations, these calculations are in excellent agreement with the experimental results. In the next section, we describe the energy transfer between two beams in a nonlinear media and show that AFC could induce energy transfer between two laser beams.

2.3 Two-beam coupling effect

In general, when two laser beams with different frequencies (ω_1, ω_2) and wavevectors (k_1, k_2) are incident on the surface of a material, a moving transient grating would be formed on the surface. Such a system allows energy transfer between two beams, which the energy transfer rate is governed by the phase velocity of the moving grating (it is proportional to δ, and $\delta = \omega_2 - \omega_1$). This effect is known as the two-beam coupling (TBC) effect, and its basic geometry is illustrated in Fig. 2.7.

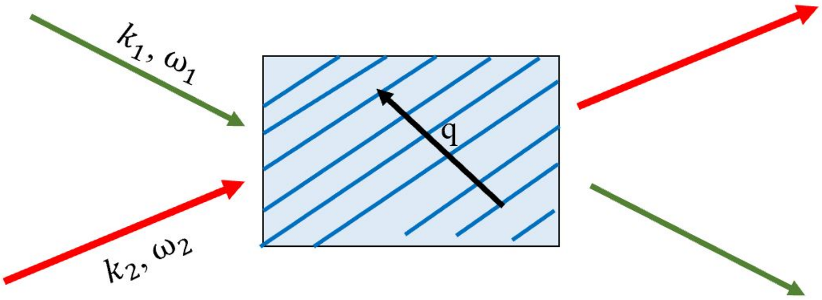

FIGURE 2.7: The schematics of two-beam coupling effect. Two laser beams with different wavelengths (ω_1 and ω_2) interact on the sample and form a moving transient grating. This moving grating effect leads to net energy transfer from one beam to the other beam. Also, q= $k_2 - k_1$.

To describe TBC model, we consider the intensity distribution of interference pattern and the nonlinear refractive index variation of non-instantaneous time response of material. This model works well with continuous-wave beams, thus it is referred as continuous-wave limit. The full mathematical treatment is shown in Appendix A. When we consider traditional materials such as fused silica, this type of material normally have weak nonlinear refractive index n_{NL} ($n_{NL} << n_0$), we refer it as weak nonlinear approximation (WNA). Using this approximation, the TBC equation can be written as:

$$\frac{dI_2}{dz} = \frac{2n_2\omega}{c}\frac{\delta\tau}{1+\delta^2\tau^2}I_1I_2, \tag{2.3}$$

where τ is the time response of a material, while I_1 and I_2 are the intensities of two beams. The left-hand side of the equation indicates how the beam's intensity transfers with respect to z, and the span of the z is the total length of the material. Furthermore, we assume that $|\delta| \ll \omega_1$ and ω_2, thus $\omega \approx \omega_1$ or ω_2 [18]. Let us consider the TBC effect in fused silica; we use n_2 value of fused silica on Table 1.1, and set $I_1 =$ 100 GW/cm^2 and $I_2 =$ 250 GW/cm^2, we then plot the mathematical evaluation result in Fig. 2.8. We can observe that the energy transfer between both beams depends on the direction of the phase velocity, and the highest TBC efficiency occurs when $\delta\tau = \pm 1$. This is a typical TBC signal.

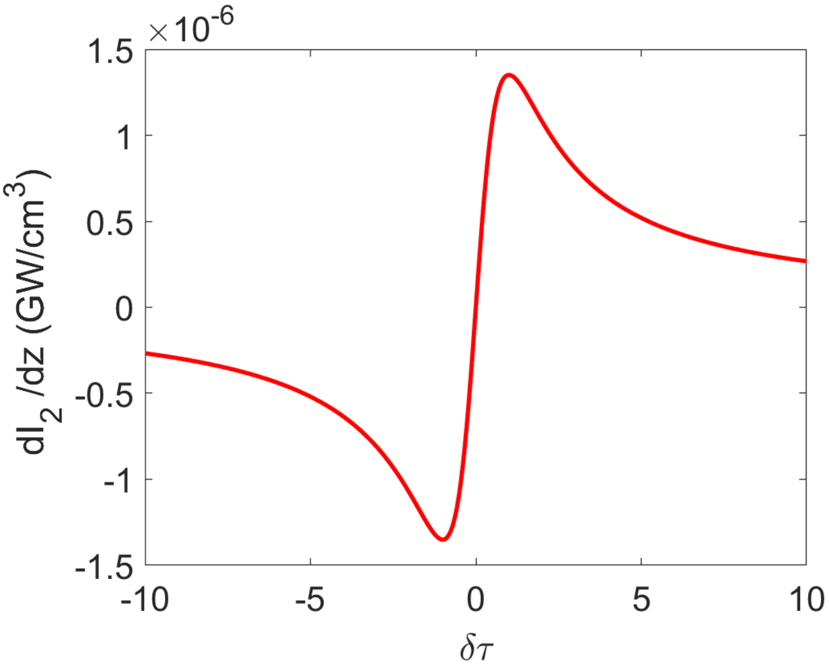

FIGURE 2.8: Mathematical evaluation of typical TBC signal using fused silica as a medium.

The TBC model with WNA works particularly well on the conventional materials, and it have been demonstrated in many works. For example, energy transfer between plasma gas [32], liquid methanol [33], and carbon disulfide [34].

When intensities are sufficient for nonlinear absorption to no longer be negligible, the nonlinear absorption of material needed to be taken into account for the TBC effect. For example, the energy transfer between two beams in a fluorescein-doped boric acid glass [35]. In this case, we modify Eq. A.4 by introducing the nonlinear absorption term β (the detailed derivation is shown in Appendix A):

$$\frac{dI_2}{dz} = \frac{2n_2\omega}{c}\frac{\delta\tau}{1+\delta^2\tau^2}I_1I_2 - \beta_2 I_2^2 - \beta_2 I_1 I_2 - \beta_2\frac{I_1I_2}{1+\delta^2\tau^2}. \tag{2.4}$$

As we can observe in Eq. 2.3 and 2.4, if the system is degenerate (δ =0), there will be no TBC, since the phase velocity is zero. In the next section, we show that, even for degenerate case, TBC can still occur in two laser pulses by introducing group velocity dispersion of the laser pulse.

2.4 Generating two-beam coupling with ultrafast laser pulses

While TBC theory shows no energy transfer if both beams have the same frequency, exchange can occur for two pulses with the same carrier frequency if other factors are adjusted. For example, when two laser pulses with same frequency interacting with a material, linear chirps of the pulses are induced. To clarify this, let us give a brief introduction on chirp of an ultra-fast pulse. When a laser pulse travels through a dispersive medium with a total length of L, a phase will accumulate throughout the medium, this phase can be expressed as:

$$\theta(\omega) = -\beta(\omega)L, \tag{2.5}$$

where $\beta(\omega)$ is known as propagation constant, if we apply a Taylor series expansion into this equation, we will obtain:

$$\beta(\omega) = \beta(\omega_0) + \frac{\partial\beta}{\partial\omega}(\omega-\omega_0) + \frac{1}{2}\frac{\partial^2\beta}{\partial\omega^2}(\omega-\omega_0)^2 + ... \tag{2.6}$$

where $\frac{\partial\beta}{\partial\omega}$ is the inverse of the group velocity, which is the velocity that energy is carried through the medium, and $\frac{\partial^2\beta}{\partial\omega^2}$ is the group velocity dispersion (GVD) of a dispersive medium, which is respects to the incident laser wavelength. As the laser pulse travels through the medium, the GVD causes some portions of the laser pulse with different frequency components travel with a different speeds, leading to the laser pulse spatially broadening or shortening, depending on the sign of GVD (assuming the laser pulse is not already Fourier-transform-limited). We can now define chirp, C, as follows:

$$C = \frac{GVD}{\tau_p^2}L, \tag{2.7}$$

where τ_p is the pulse duration of the laser pulse. By considering linear chirp, we can understand that when two laser pulses with same wavelengths are introduced, the chirp effect and their overlap in time and in the material, will lead to an effective frequency difference being induced at that moment of time, since the laser pulses are interacting with different frequency components. This will lead to the TBC effect. The effective frequency shift induced by linear chirp can explained as:

$$\delta = \frac{-tC}{\tau_p^2(1+C^2)}. \tag{2.8}$$

where τ_p is unchirped laser pulse duration.

For the mathematical model to describe the TBC effect using laser beam pulses, we have to consider the beam profile in time, which is typically Gaussian. We adapted the mathematical treatment used in Ref. [36], and the final form of the energy transfer can be expressed in term of change of transmittance of the measured beam:

$$\frac{\Delta T}{T}(\tau,\delta) = \frac{2}{\sqrt{3}}\exp\left(\delta^2\tau_{res}^2/6\right)\exp\left[-2(\tau)^2/3\tau_{res}^2\right]\times[2\Delta\Phi\sin(2\delta\tau/3) - q\cos(2\delta\tau/3)], \tag{2.9}$$

where δ is the change of frequency, τ is the time delay, τ_{res} is time response of a material. The nonlinear phase shift of a material, $\Delta\Phi$, which is defined as $kn_2I_{\text{pump}}L$, while q is associated with the nonlinear absorption of a material, define as $\beta_2I_{\text{pump}}L$. In typical experiments, δ is induced by introducing linear chirp, which is described in

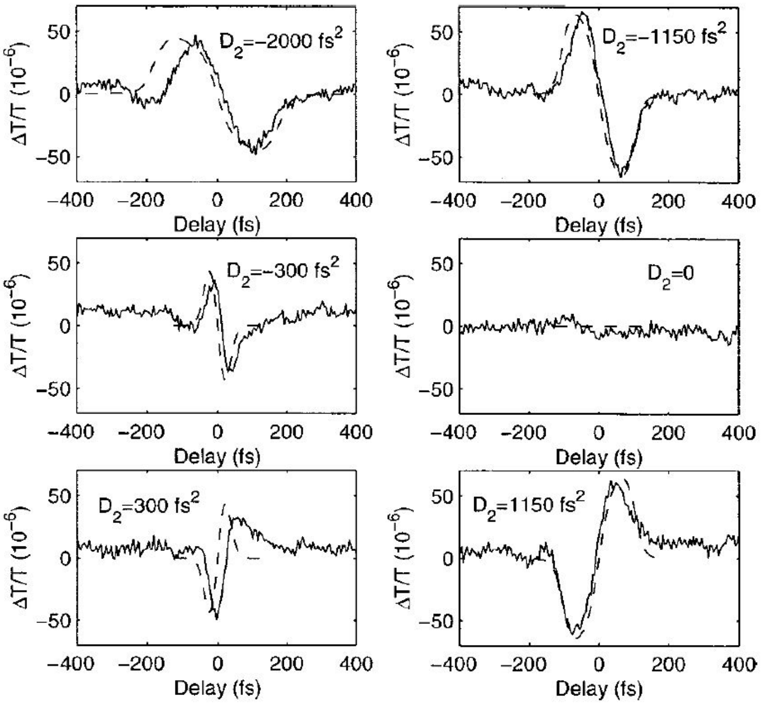

Figure 2.9: The two-beam coupling effect on fused silica by introducing linear chirp into the laser pulse. Adapted with permission from [9] © The Optical Society.

Eq. 2.8.

Many works have demonstrated TBC effect using laser pulses with linear chirp on different mediums such as fused silica [9], argon gas [32], and other semiconductors [37]. Figure 2.9 shows the experimental results of pump-probe experiments using fused silica as a medium [9]. In the experiments, both laser pulses have an initial pulse duration of 30 fs, and they used prism pairs to introduce and tune the chirps of both pulses. As we can see from the experimental data, the TBC signal is highly dependent on the chirp parameter they introduced, and there is almost no TBC signal when the chirp is zero. In the next section, we will show how the TBC effect can be induced without introducing external chirp by inducing AFC.

2.5 Self-manifesting the TBC effect with AFC

In order to predict how TBC would be manifested by AFC, we used the experimental results from Ref. [8]. To be specific, we extract the AFC frequency shift, δ, from Fig. 2.6b and c, and plot them in Fig. 2.10a and c, which corresponds to the AFC shifts with input pump intensity of 161 GW/cm^2 and 268GW/cm^2, respectively. Furthermore, the response time of ITO is 85 fs, which obtained from Ref. [10].

To determine TBC signal, we use Eq. 2.9. Since nonlinear parameter (n_2 and β_2) are not provided for the sample used in the paper [8], we approximate these parameters using Ref. [7]. In Table 2.1, we show different nonlinear parameters used for I_{pump} = 161 GW/cm^2 and I_{pump} = 268 GW/cm^2 (Note: the probe intensity for both cases was kept low to avoid SPM), then we obtained the TBC signal for both

TABLE 2.1: Parameters used for simulations

Parameters	I_{pump} = 161 GW/cm^2	I_{pump} = 268 GW/cm^2
n_2 (cm^2/W)	0.0007	0.0005
β (cm/W)	-30	-20

cases, and show the calculations in Fig. 2.10b and d. In these results, we observe that AFC-induced TBC features are different from the ones in Fig. 2.9. Since β_2 of ITO is much higher than fused silica and the different time-scales of electron-phonon interactions, the energy transfer is not symmetric. Furthermore, the predicted TBC exchange rate ($\Delta T/T \sim 0.5$) is several orders of magnitude higher than TBC on fused silica without chirp ($\Delta T/T \sim 10^{-9}$ [9]).

Therefore, we are motivated to use ITO as a medium to study the TBC effect. Our goal is to measure the AFC-induced TBC effect on ITO without introducing chirp, and use these results to determine the transmission profile in the time domain with a varying range of input pump intensities. In the next chapter, we perform a series of pump-probe experiments with different input intensities for this purpose.

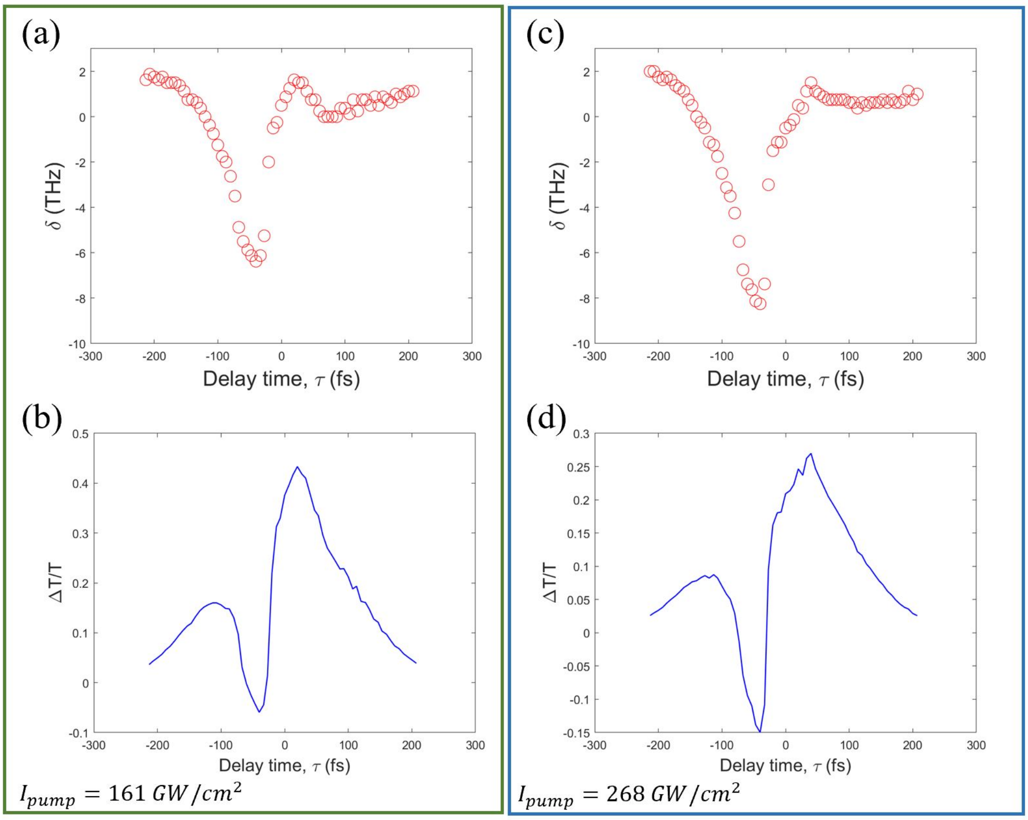

FIGURE 2.10: The two-beam coupling effect on ITO induced by AFC. (a) and (b) are the AFC shift in ITO with the input pump intensity of $I_{pump} = 161$ GW/cm^2 and $I_{pump} = 268$ GW/cm^2, respectively. The corresponding calculated relative changes in transmittance are (b) for $I_{pump} = 161$ GW/cm^2, and (d) for $I_{pump} = 268$ GW/cm^2. The wavelength of pump laser pulse is 1235 nm, and the response time of ITO is 85 fs [10].

Chapter 3

Experiment and discussions for AFC-induced TBC

3.1 Experimental setup for degenerate four-wave mixing

In this section, the experimental setup mainly used is the so-called degenerate pump-probe setup. This is a standard tool to determine optical properties of a material by measuring its optical responses. Figure 3.1 shows the basic geometry of the pump-probe setup [38], and it is worth noting that this geometry is equivalent to a degenerate four-wave mixing (DFWM) geometry. It works as follows: a pump laser pulse interacts with a targeted medium to excite it. This excitation causes a change in the optical property of the medium and the magnitude of nonlinear optical response can be tuned by the intensity of the pump pulse. Next, a probe laser pulse sent with a short delay time relative to the pump pulse, τ, to interact with the sample. A detector is used to collect the transmitted probe laser pulse as a function of the pump intensity and the time delay between pump and probe. The probe laser pulse intensity is much weaker than the pump laser pulse to avoid unnecessary probe laser changes. By measuring either probe laser pulse or by measuring specific effects raised from the interaction of two pulses with the medium, it is possible that one can extract the full time response of the medium after performing a series of experiments with different τ values.

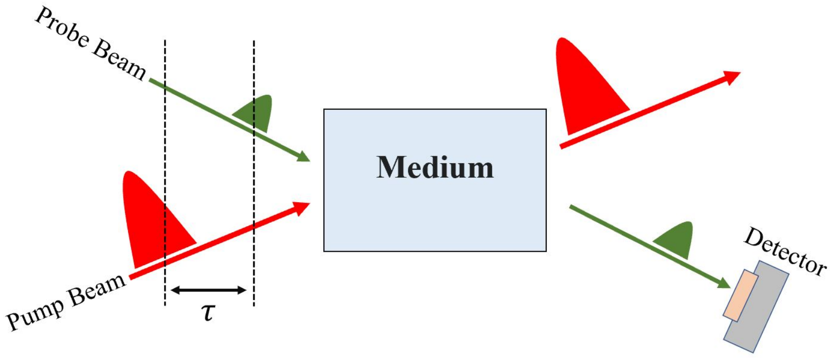

FIGURE 3.1: Basic scheme for pump-probe setup.

We can hypothesize a lot about the temporal response by observing the change of intensity, direction, and spectrum of the probe beam under the influence of the pump beam, such as electron-electron and electron-phonon interactions of the material, the relaxation time of the photo-excited states, and the self-focusing effect. We are interested in studying the nonlinear optical response of an ENZ material. In particular, we ensure two ultrafast laser pulses overlap each other spatially and temporally to form an interference pattern on ITO's surface. This pattern acts as a diffraction grating; thus, diffracted laser beams propagate from ITO. Detectors are used to measure the first-order diffracted beams, zeroth-order beams, and input beams to study the response dynamics of ITO.

First, the calibration of the experimental setup will be explained, then we will briefly discuss how to optimize the experimental setup to obtain maximum TBC efficiency. Finally, we will discuss the experimental results.

3.2 Beam preparation and alignment

3.2.1 Calibrating input laser beam power

In a nonlinear optical experiment, it is important to know how much laser power is generated from the laser system and impinging on the sample. Therefore, we installed a glass slide on the experimental setup to calibrate the input laser power. Figure 3.2 demonstrates the calibration setup for the input beam, the input laser, P^{in}, is focused by a lens and incident on a thin glass slide. A small portion of the beam, R, is reflected by the glass slide, and then a photodetector (918D-IG-OD3R, Newport) collects a portion of the beam. The remaining light is transmitted, T, through the glass and collected by a photodetector. We know that:

$$P^{in} = T + R, \tag{3.1}$$

therefore, by measuring the transmitted light and reflected light, we will then calibrate the glass and determine the input power.

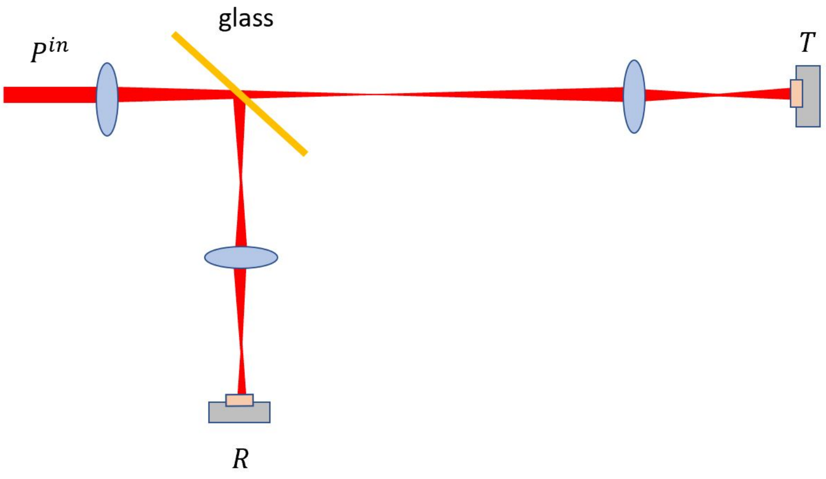

FIGURE 3.2: Experimental setup for glass calibration for determining the input laser power.

3.2.2 Calibrating laser beam intensity

Understanding how the laser beam profile evolves while it propagates through space or a medium is essential for calibrating its intensity. Laser beam shape is typically well-described by considering a Gaussian profile. The Gaussian intensity distribution can be shown as:

$$I(r,z) = I_0\left(\frac{W_0}{W(z)}\right)\exp\left(-\frac{2r^2}{W^2(z)}\right), \tag{3.2}$$

where z is the axial distance from the beam center, W_0 is the beam waist when z$=0$ and r is radial position. When z$\neq 0$, the laser beam will then evolve with respects to $W(z)$:

$$W(z) = W_0\sqrt{1+\left(\frac{z}{z_0}\right)^2}, \tag{3.3}$$

where z_0 is the Rayleigh range of the beam ($z_0 = \frac{\pi w_o^2}{\lambda}$), it is defined as the location which the Gaussian beam waist expands by a factor of $\sqrt{2}$.

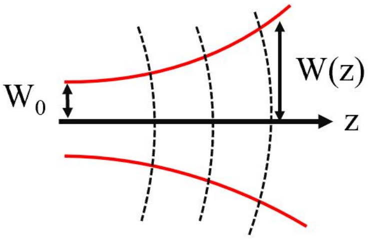

Figure 3.3: The evolution of the Gaussian beam waist W(z) along the axial direction, z. Image is from [11].

We are interested in determining the location where the beam size is minimum which would provide us with the highest intensity since the laser intensity is inversely proportional to the beam size. We employ a CMOS camera (Thorlabs, DCC1545M-GL) to capture the laser beam image. The experimental setup is shown in the left panel of Fig. 3.4. The laser beam is first generated by the OPA and Ti: Sapphire laser system and is focused by a lens with a focal length of 120 mm. Then, we gradually tuned the camera's position by a translational stage and determined the beam's location at a focal point. The right panel of Fig. 3.4 shows the actual image captured by the camera. We then used the camera software to determine the beam size. Once we measured the beam size, we then used an IR photodetector to measure the average beam power, P_{ave}, and calculated the laser beam intensity using the following equation [11]:

$$I_{\text{peak}} = \frac{2P_{\text{ave}}}{\pi\sqrt{\pi}w_o^2\tau R}, \tag{3.4}$$

where τ is the pulse duration, which is 110 fs for our laser system, and R is the repetition rate, which is 1000 Hz in our case.

3.2.3 Temporal overlap calibration

An essential step for setting up an ultrafast pump-probe experiment is to determine the temporal overlap of the pump and probe beams.

The experimental setup is illustrated in the left panel of Fig. 3.5. A wavelength-tunable optical parametric amplifier (OPA) is used to generate a laser beam with a time duration of 110 fs (TOPAS prime, Spectra Physics) pumped by an amplified

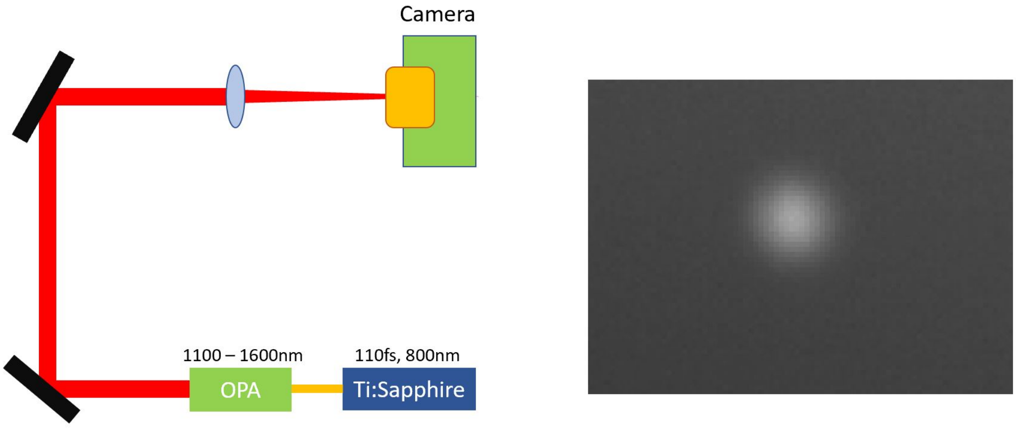

FIGURE 3.4: Capturing a laser beam. Left panel: the experimental setup for capturing laser beam. Right panel: the actual image of an ultrafast laser pulse beam.

Ti:sapphire laser for the experiments. The OPA is an optical device that converts the frequency of an input laser beam into two output laser beams (typically named signal and idler) of lower frequencies by using a second-order nonlinear process ($\chi(2)$) in the medium. We can tune our OPA's signal wavelength from 1100 to 1600 nm and use it as the input of our TBC experiment. We first installed a pellicle beam splitter (BP245B3, Thorlabs) to split the input laser beam from the OPA into two paths, P_1^{in} and P_2^{in}. Then, we installed a high-precision translation stage (DDSM100, Thorlabs) in the P_2^{in} path. Next, we adjust both beams to spatially overlapping them by monitoring them through the camera. To ensure the temporal overlap of both beams, we measured the distance of both paths, ensuring that the difference can not be larger than the travel of the translational stage. Finally, we gradually changed the stage position. When the lengths of both paths are the same, temporal overlap occurs and the interference pattern between the beams is visible on camera. The actual image of the temporal overlap of both beams is shown in the right panel of Fig. 3.5. In the next section, we discuss the procedure for optimizing the experimental setup in order to obtain the clear, repeatable experimental results.

3.3 Optimizing the experimental setup

After all calibrations are done, we introduce the ITO sample at the position of spatial and temporal overlap of the beams and add multiple detectors to observe the TBC effect and optimize for clear, repeatable experimental results.

Figure 3.6 displays the full experimental setup for probe-pump experiment. We installed Glen-Taylor polarizers and half-wave plates mounted on the rotational stages on both paths to control the beam intensities, and both beams are rendered p-polarized. Then, we placed an ITO thin film (thickness: 310 nm) at the location where spatial and temporal overlapping occur. To ensure the sample is at the location, we gradually tuned the sample along the z-direction. When the surface of the sample reaches the ideal location, we observed first-order diffracted beams appear at P_1^{1st} and P_2^{1st} detectors.

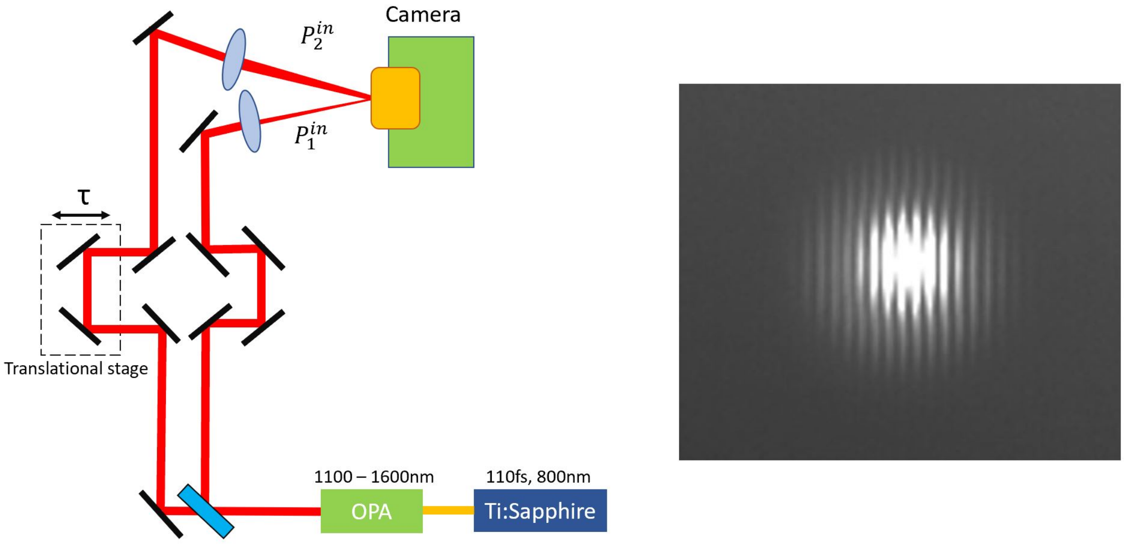

Figure 3.5: Temporal overlapping of both beams. Left panel: the experimental setup for capturing laser beams. Right panel: the actual image of a temporal overlap of both beams.

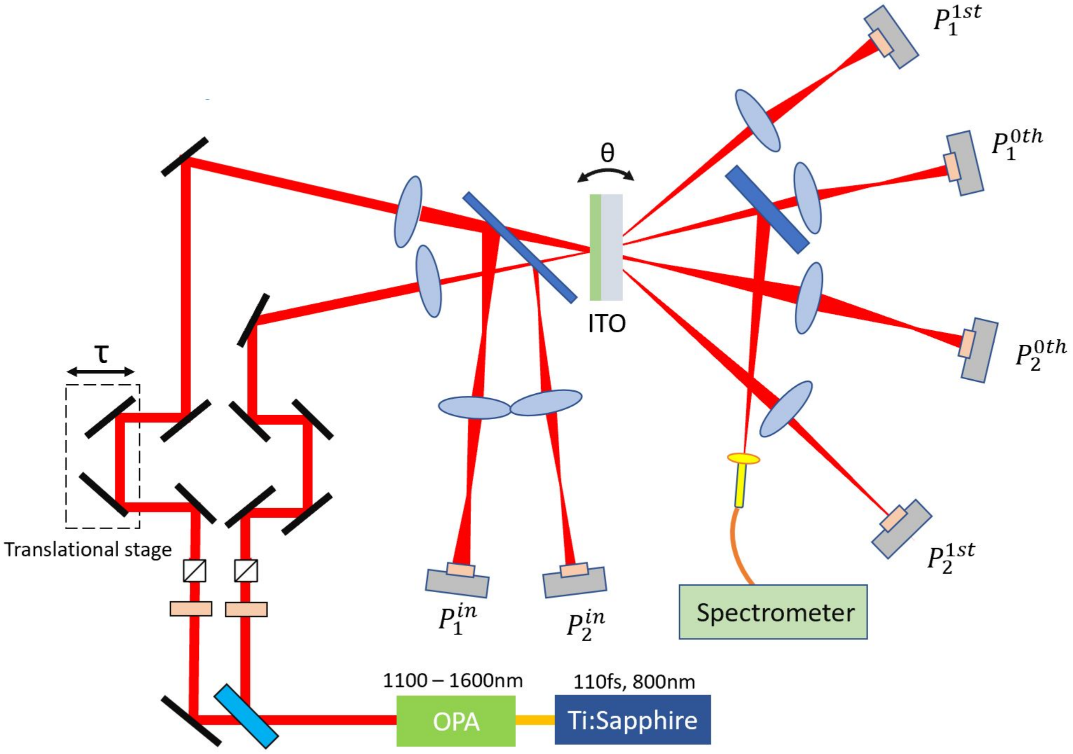

Figure 3.6: Full experimental setup for DFWM in ITO. The detailed explanation is in the main text.

Figure 3.7 shows the image of the observed first-order diffracted beams ($P_{1,2}^{1st}$) and the zeroth-order beams ($P_{1,2}^{0th}$) simultaneously captured by a high resolution IR camera. After observing the diffracted beams, six InGaAs photodetectors (918D-IG-OD3R, Newport) are placed and aligned to measure 1st order, zeroth-order, and input beam powers. To obtain maximum energy transfer through TBC effect, we further tuned the sample position such that maximum transfer to the first-order detectors is achieved, we defined first-order efficiency as:

$$\text{Efficiency } = \frac{P_{1,2}^{1st}}{P_{1,2}^{\text{in}}}. \tag{3.5}$$

In the next section, we discuss the obtained experimental results after the optimization, and demonstrate AFC-induced TBC effect.

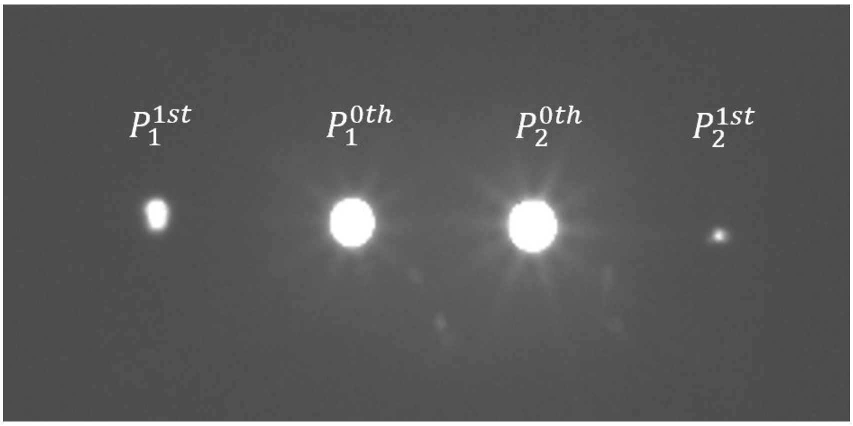

FIGURE 3.7: Observation of first-order beams ($P_{1,2}^{1st}$) and zeroth-order beams ($P_{1,2}^{0th}$). This image is captured by a high resolution IR camera.

3.4 Results and discussion

3.4.1 Experimental results of first-order diffracted beam measurements

We first discuss the experimental results of the first-order diffracted beam measurements. Figure 3.8 shows the measured efficiency of the first-order diffracted beam of P_1^{1st} as function of delay time, τ with various input intensities of P_1^{in} using Eq. 3.5. The input intensity of P_2^{in} is fixed at 500 GW/cm^2. As we can observe, the measured efficiency gradually increases as input intensity increases, and the peaks of each plot occur at the same delay time that we set to be $\tau = 0$ fs. The highest efficiency obtained saturates at about 0.8 % where its input intensity is 334 GW/cm^2, which is a repeatable result across multiple measurements. Therefore we have confirmed an observation of TBC from degenerate beams without any linear chirp.

3.4.2 Experimental results of zero-order diffracted beam measurements

After we ensured the coupling between two beams are optimized by maximizing the first-order efficiency, we next measured the zero-order diffracted beams.

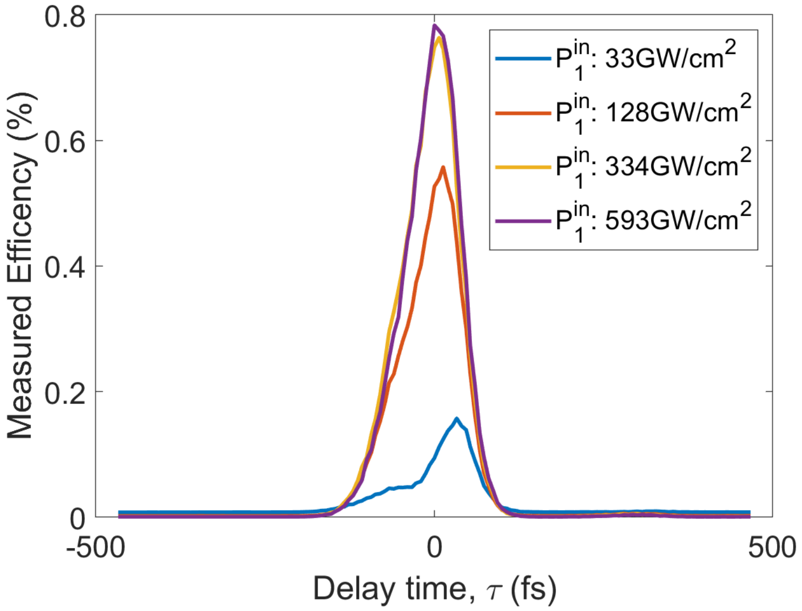

FIGURE 3.8: The measured efficiency of the first-order beams in P_1^{1st} detector as a function of delay time, τ with various input intensity of P_1^{in}. The input intensity of P_2^{in} is fixed at 500 GW/cm^2.

Before showing and discussing our complete set of experimental results, we first demonstrate the measured AFC shift of P_1^{0th} (input intensity is 236.7 GW/cm^2) with an input pump intensity of 292.2 GW/cm^2 from P_2^{0th} to gain a clearer picture for our results. We define the measured wavelength of the peak of the spectrum at $\tau=$ -500 fs as reference wavelength and extract the change of wavelength as a function of τ. This value is selected so that the two beams are entirely temporally separated and therefore, no AFC would be induced at this time difference.

We then plot the change of wavelength as a change of frequency, δ, and plotted it in Fig. 3.9a, thus making analogous plot to the changes in frequency due to AFC shown in Fig. 2.10a and c from our previous work [8]. Figure 3.9a confirms that the AFC shift occurs within a similar time frame that is consistent with the temporal response of ITO shown before and the extrema for δ ($\sim$8 THz) are also comparable to the AFC shift shown in that work [8].

Next, we plotted the corresponding measured transmittance, T, in Fig. 3.9b. Different processes that happen with different delay times in the P_1^{0th} beam are indicated as regions (I), (II), (III), and (IV). In region (I), P_2^{0th} separated from P_1^{0th} in time. Thus, we observed that the transmittance stays constant throughout this region. As P_1^{0th} beam arrives at the sample first before P_2^{0th} beam, both beams start interacting and forming an interference pattern in the region (II). This interaction leads to an increase of refractive index, and thus AFC is induced, which causes red-shifting of the wavelength of the P_1^{0th} beam. As a result, we observed a drop in transmittance of P_1^{0th} because a portion of energy transferred to P_2^{0th} due to AFC-induced TBC. In region (III), both beams still form the interference pattern. However, the AFC starts causing blue-shifting to P_1^{0th} beam, thus the phase velocity of the moving transient

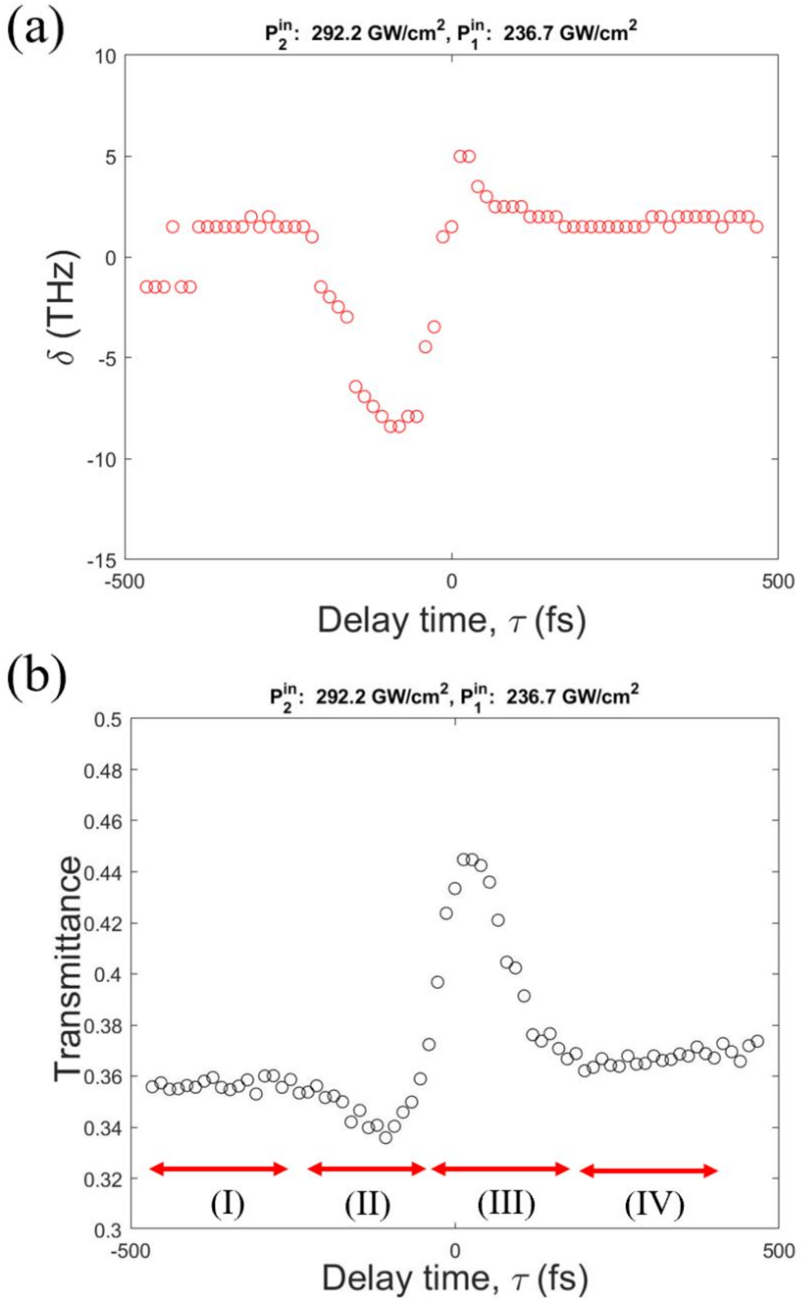

FIGURE 3.9: The representative experimental results. (a) the measured change of frequency due to AFC effect, δ, as a function of delay time, τ. (b) the experimental transmittance, T, as a function of delay time (black dots), the labels in different timings indicate various processes that occur in ITO. The detailed explanations are in the main text. The title of both graphs shows the input intensities for P_1^{in} and P_2^{in}.

grating changes to the opposite direction, so a portion of the energy of P_2^{0th} beam couples to P_1^{0th} instead. Finally, P_2^{0th} beam is significantly early than P_1^{0th} beam. Thus both beams do not interfere in the region (IV). However, some induced changes (e.g. saturable absorption) caused by P_2^{0th} remain and are witnessed by P_1^{0th}, resulting in the transmittance of P_1^{0th} is slightly higher than in region (I).

We repeated this experiment while varying the input intensities of P_1^{in} and P_2^{in} (see their individual titles) to show the evolution of the transmittance of P_1^{0th} in Fig. 3.10. Figure 3.10 contains 21 subplots, and each represents T (y-axis for each subplot) as a function of delay time, τ (x-axis for each subplot). The subplots are organized such that the input intensity of P_2^{in} increases from the top to bottom row, while the input intensity of P_1^{in} increases from the left to the right column.

By plotting all these TBC responses together, we can begin to see trends. For instance, we focus on a row of subplots for a single P_2^{in} intensity (such as 293 GW/cm^2). As input intensity of P_1^{in} increases, we can observe that the transmittance increases of P_1^{0th}, in the region (I) where only P_1^{0th} beam is interacting with the material. This effect is likely due to saturable absorption of high intensity of P_1^{in}. Also, we can observe that the dip in the region (II) of each subplot starts developing as the input intensity of P_1^{in} increases suggesting greater coupling from P_1^{0th} to P_2^{0th}. Next, let's look at a column subplots for a single P_1^{0th} value (such as 174 GW/cm^2) as P_2^{in} increases. Here we observed slight increases of the peak in region (III) as the input intensity of P_2^{in} increases. Furthermore, we also do not observe significant saturable absorption induced by P_2^{0th}, this suggests that the nonlinear response does not strongly depend on the input intensity of P_2^{0th} beam.

While these results suggest that TBC induced by AFC are indeed being experimentally observed. In order to compare this to the model described in Chapter 2 (Eq. 2.9), we need to consider the normalized change of transmittance, $\Delta T/T$. Thus, we plotted the measured $\Delta T/T$ in Fig. 3.11, using the standard equation used in many related works [36, 39, 37]:

$$\frac{\Delta T}{T}(\tau) = \frac{P_{1,2}^{0th}(\tau) - P_{1,2}^{0th}(\tau = -500\ fs)}{P_{1,2}^{0th}(\tau = -500\ fs)}. \tag{3.6}$$

Using Eq. 3.6, the nonlinear contribution from the P_1^{0th} beam will be cancelled out by normalizing the transmittance, thus we only have to consider nonlinearity from P_2^{0th}.

The experimental $\Delta T/T$ of P_1^{0th} for the listed input intensities are plotted as blue dots. Next, we used the measured δ from Fig. 3.9a, and Eq. 2.9 to see how well our model described the resulting TBC response. Our TBC fit (red line) is shown in Fig. 3.11. As we can observe, our model predicts all regions mentioned in Fig. 3.9b. This close agreement with expermential result, including the large magnitude of the energy transfer and the significant asymmetry of the response due to absorption, suggests that our AFC model can likely explain the observed TBC effect in an ENZ material.

We then re-normalized our data from Fig. 3.10 as the $\Delta T/T$ plots to show the evolution of the change in transmittance due to TBC in Fig. 3.12. The layout of Fig. 3.12 is the same as Fig. 3.10. Across all cases, the experimental $\Delta T/T$ are shown as a blue dot, and our TBC models for each data are shown as a red line by fitting

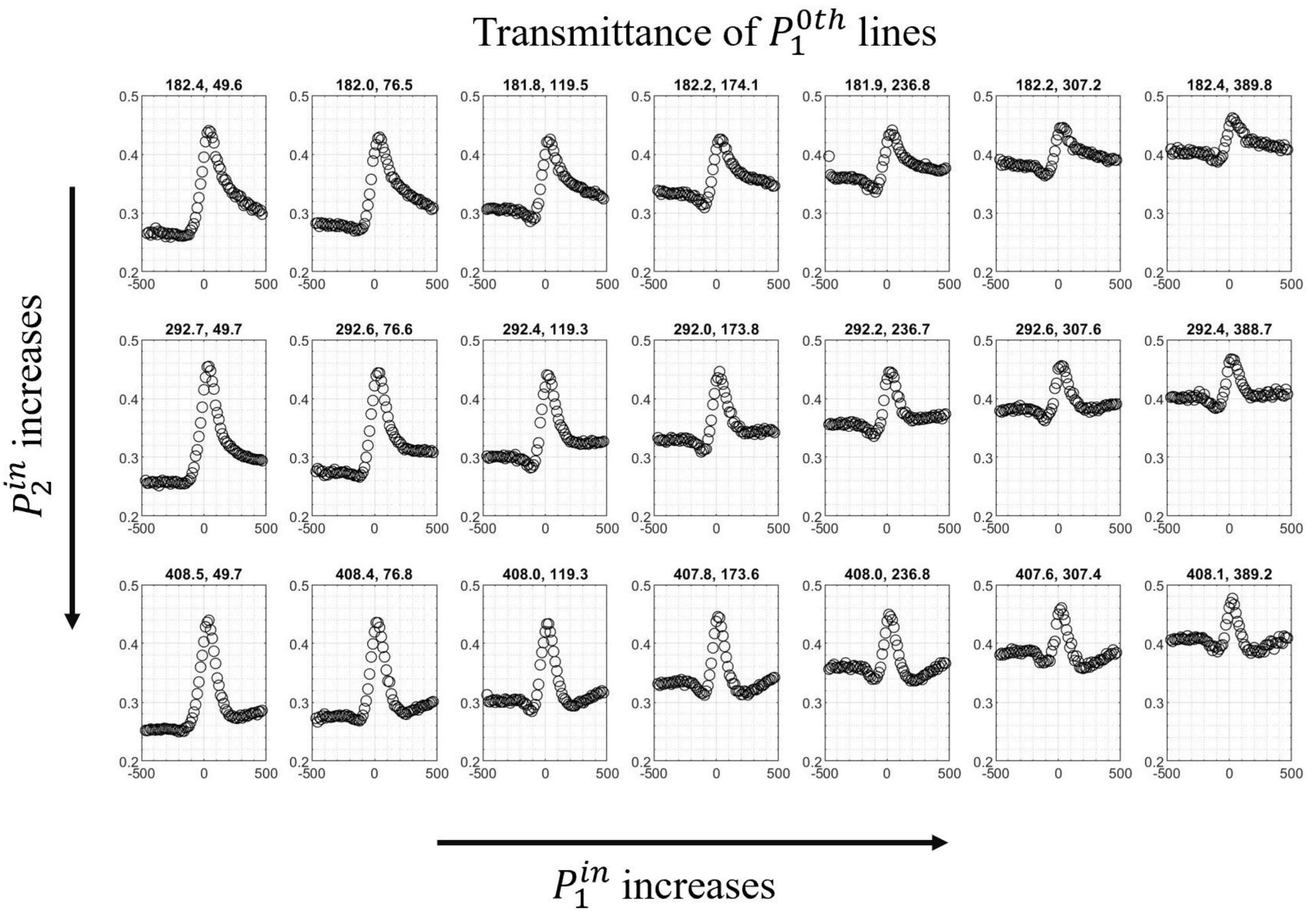

FIGURE 3.10: The evolution of transmittance with different input intensities. There are 21 subplots in this figure, each represents T of P_1^{0th} (vertical axis) as a function of delay time, τ (horizontal axis). The title of each subplot shows the applied input intensities (GW/cm^2) for P_2^{in} and P_1^{in}.

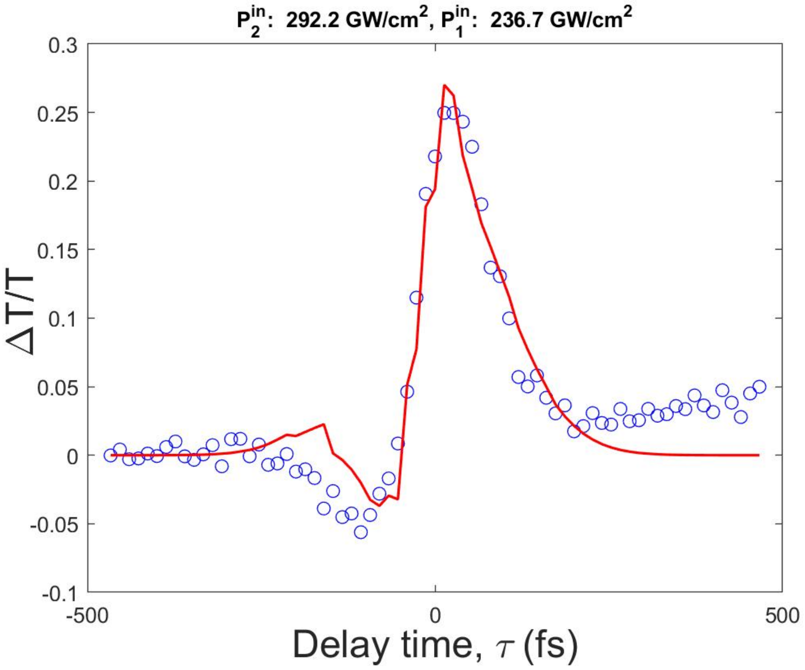

FIGURE 3.11: The AFC-induced TBC. The experimental change in transmittance, ΔT/T, as a function of delay time using Eq. 3.6 (blue dots). We use Eq. 2.9 with δ to fit the experimental result and plot the fit as the red line. The good agreement with the experimental results shows that the TBC effect indeed occurs due to the AFC shift. The title of the graph show the input intensities for P_1^{in} and P_2^{in}.

n_2 and β_2 values for each set of input powers, showing reasonable agreement with the experimental results.

By plotting all these TBC responses together, we can observe the trends. For instance, as P_2^{0th} increases, we can observe that the change of transmittance decreases. This is due to saturable absorption because the transmittance of the probe beam increases as probe intensity increases (which we have shown in Fig. 3.10), leading to the denominator of the $\Delta T/T$ increasing.

Furthermore, our model is a better fit for the experimental results with high input intensities. The reason is as follows: with low intensities for both beams, the frequency shift induced by AFC is not significant in generating the TBC effect, and our model considers only the TBC effect and neglects other effects, such as electron-phonon interaction. Therefore, as input intensities get higher, the AFC would be more pronounced, leading to significant energy transfer, hence better fittings.

Because the nonlinear responses n_2 and β_2 were fitted for different input intensities, we plot them as a function of P_1^{0th} in Fig. 3.13. In this figure, we can observe that n_2 and β_2 quickly converge due to the saturable absorption. The both parameters quickly saturate to constant values of n_2= 6×10^{-4} cm^2/GW and β_2= -18 cm/GW as the input intensity increases.

At input intensity of P_1^{0th}= ~70 GW/cm^2, we observed that the nonlinear parameters are n_2= 1.1×10^{-3} cm^2/GW and β_2= -75 cm/GW. As for the magnitude of these values, they are smaller than the corresponding values measured in our previous Z-scan measurements with same input intensity [7], where values of n_2= 0.11 cm^2/GW and β_2= -7131 cm/GW were recorded. This can be explained by difference in the set-ups: In this TBC experiment the incident beams at almost perpendicular to ITO, while the values recorded in Ref.[40] had the beam striking the sample in the Z-scan measurement at a 60^o angle of incidence.

However, our results for n_2 and β_2 are still off by a factor of ~2 with the Z-scan measurement [7] when the sample is perpendicular to the incident laser beam (2.2×10^{-3} cm^2/GW and 159 cm/GW, respectively). The reason is as follows: the experimental results obtained by Z-scan measurement were slightly overestimated because the measurement ignores the change in reflectivity caused by Δn. Hence an additional factor of ~1.8 should be taken into account [7].

Therefore, our results are still consistent with the Z-scan measurement [7] when the sample is perpendicular to the sample. Hence, our results appear to not only confirm that the observed TBC is caused by AFC but could also be a reliable technique for extracting n_2 and β_2 values from an ENZ material.

Going forward, much attention has been shifting to developing ultrafast temporal holograms using ENZ material as a medium [41, 42]. Since TBC has been applied to boost hologram efficiency [43], we believe that our AFC-induced TBC scheme could also be similarly applied for ultrafast temporal holograms.

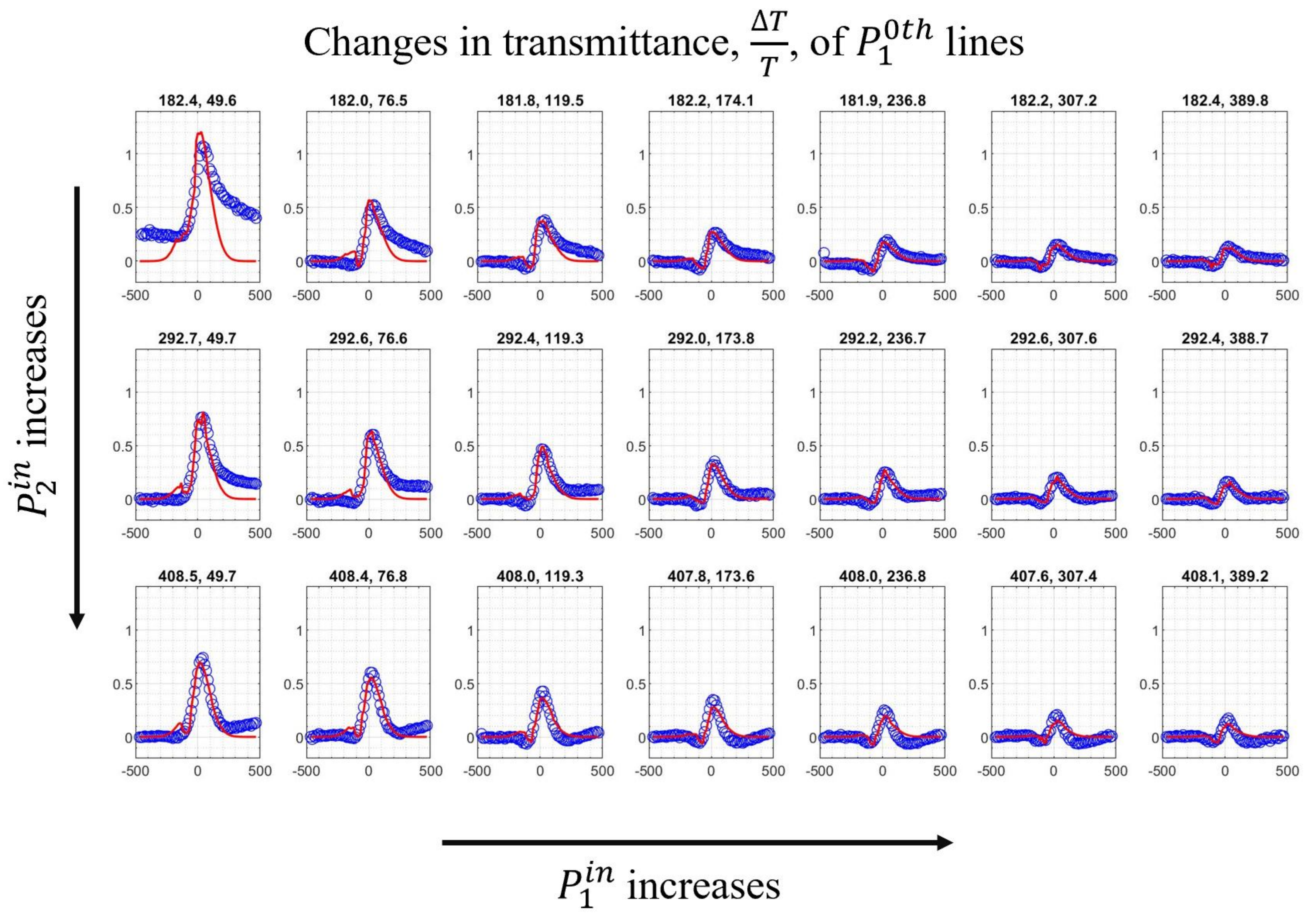

FIGURE 3.12: The evolution of TBC signal with different input intensities. There are 21 subplots in this figure, each represents $\Delta T/T$ of P_1^{0th} (vertical axis) as a function of time delay, τ (horizontal axis). The title of each subplot shows the applied input intensities (GW/cm^2) for P_2^{in} and P_1^{in}. In each subfigure, the experimental result is plotted as blue dots, and the theoretical fitting is plotted as red line.

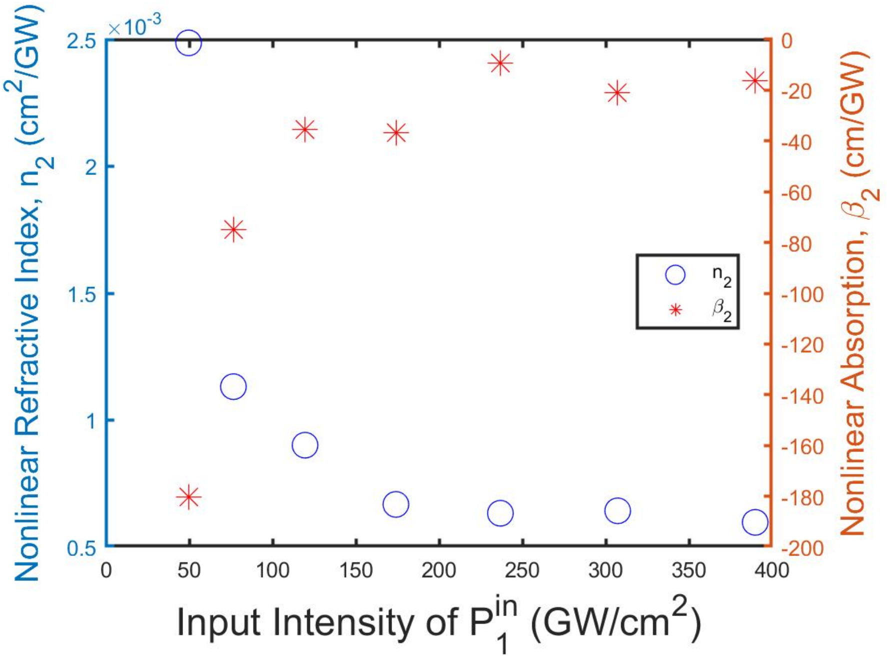

FIGURE 3.13: The extracted nonlinear refractive index, n_2, and nonlinear absorption term, β_2, as functions of input intensity of P_1^{0th} (GW/cm^2).

Chapter 4

Background knowledge of Fourier-Engineered Plasmonic Lattice Resonances

In this chapter, I will introduce the plasmonic metasurface, in which a sub-wavelength-order arrangement of metal nanoantennas enables unconventional light manipulation, beyond what conventional materials can achieve. First, I introduce the optical response of a single plasmonic nanoparticle and then contrast that with the collective optical responses of multiple plasmonic nanoparticles. Next, I will explain the fabrication process of our plasmonic metasurfaces and the experimental setup used for optical characterization in the thesis. This background knowledge provides context to better understand the published manuscript in the next chapter.

4.1 Localized surface plasmon resonance

First, we begin with understanding light interaction with a single plasmonic nanoparticle. A sufficiently small, bar-shaped nano-antenna will have a single plasmonic resonance mode called a local surface plasmon resonance (LSPR). LSPRs can be tuned to different resonant wavelengths and to have higher order modes by changing the shape of the nanoparticle [44].

The physical origin of the LSPR can be understood as follows: when a metallic nanoparticle experiences an excitation from a light beam with a wavelength that is comparable to the nanoparticle size, the oscillating field from the light beam will drive the free electrons of the nanoparticle to oscillate when oscillation matches the natural resonant frequency of the nanoparticle, the light couples optimally into the plasmon resonance mode, because the localized plasmon frequency depends on the dimension of the nanoparticle, different particle dimension will couple different frequencies of light [12, 45]. Figure 4.1 shows simulated scattering spectra of aluminum rectangular nanoparticle [12]. As the particle length increases, one can observe that the LSPR wavelength moves to longer wavelengths. Additionally, LSPRs confine light in the nanoscale by having small mode volumes that are tightly confined to the surface of the nanoparticle, leading to significant local-field enhancements [46]. These important properties of LSPR benefit many applications in broad range of research areas [47, 48, 49, 50].

However, the applications of LSPRs are limited by the intrinsic absorption loss of metals. To quantify how well a resonator traps light, a dimensionless parameter known

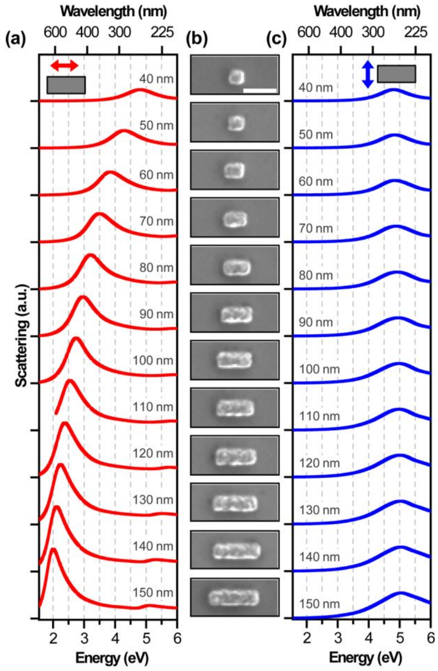

FIGURE 4.1: **Localized Surface Plasmon Resonance.** Simulated scattering spectra of aluminium rectangular nanoparticle with increasing length for (a) longitudinal and (c) transverse polarization. The localized surface plasmon resonance (LSPR) wavelength is red-shifted as the particle length increases. Image adapted from [12] with permission.

as the quality-factor (Q-factor) is often used. This quantity is defined as the ratio of resonance frequency of a resonator to its corresponding resonance bandwidth when an oscillating field is applied to the resonator. A higher Q-factor also corresponds to a lower damping rate, leading to longer trapping time of the applied oscillating field. The Q-factor can be expressed mathematically as:

$$Q = \frac{\omega_{res}}{\Delta\omega} \tag{4.1}$$

where ω_{res} is the resonance wavelength and $\Delta\omega$ is the resonance bandwidth. Using this figure of merit, we can state that the resonance modes of LSPRs are typically short lived and spectrally-broad, with Q-factor less than 10 [51, 13].

Many methods have been proposed to improve the Q-factor of plasmon resonances [52]. Gold or silver are frequently used as a plasmonic material, but alternative materials such as graphene and aluminum usually have lower extinction loss at the target wavelengths [53]. Furthermore, One can use the interaction between nanoparticle and substrate to improve the Q-factor. Since the collision of electrons contributes to the extinction loss, cooling down the temperature leads to lower loss and a higher Q-factor is also considered [52]. Moreover, other more exciting ideas have also been demonstrated. For example, considering the hybrid system [54], adding gain medium into the metasurface [55]. For this work, we study a collective response of multiple nanoparticles, which induces a resonance mode known as surface lattice resonance (SLR). The detail of this resonance mode is explained in the next section.

4.2 Surface lattice resonance

SLRs are resonance modes that correspond to the collective optical responses induced by light-matter interaction of multiple nanoparticles [56]. Such resonance mode highly depends on the lattice arrangement, and its resonance wavelength is related to the periodic spacing difference between the nanoparticles in a periodic lattice. SLRs have been a potential candidate for improving plasmonic devices because these modes typically do not have most of their electromagnetic fields in close proximity to the nanoantennas themselves, reducing absorption losses. Consequently, they can have relatively high Q-factors compared to LSPRs [13, 16].

Figure 4.2 displays the calculated transmission spectra of a system consisting of nanospheres with a radius of 80 nm. For Fig. 4.2a, a single nanosphere is considered, and the only plasmon resonance is the LSPR. As expected, the Q-factor is low ($Q \sim 10$), resulting in a spectrally broad dip in transmission. However, when an 1D array of nanospheres is considered (insert in Fig. 4.2b), an additional surface lattice resonance is induced. The corresponding lattice resonance wavelength, λ_{SLR}, can be shown as:

$$\lambda_{SLR} = n_{BG}P, \tag{4.2}$$

where P is the periodic spacing of the particles, and n_{BG} is the refractive index of the surrounding medium. In the case of Fig. 4.2b, the periodic spacing is 640 nm, and n_{BG}= 1. Thus, the SLR wavelength is at 640 nm using Eq. 4.2. We can observe that the bandwidth of the resonance mode is much narrower than the LSPR; hence the Q-factor is significantly improved (~100)[13]. It is worth noting that the LSPR still remains, but it is super-imposed by the spectral response of the SLR.

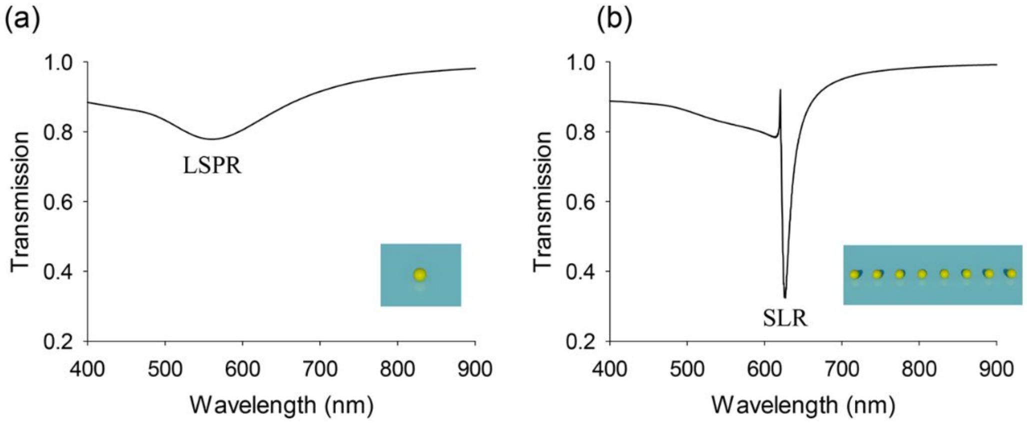

FIGURE 4.2: Transmission spectra for localized surface plasmon resonance and surface lattice resonance. (a) the calculated transmission spectra of a single nanospehre particle. Only LSPR is induced. (b) the calculated transmission spectra of an array of nanospheres with periodic spacing of 640 nm. Both LSPR and SLR are induced. In both cases, the size of nanoparticles is the same: their radius is 80 nm. Image adapted from [13].

Designing a metasurface with a particular SLR requires simulating the combined, response of multiple nanoantennas based on their relative positioning. A standard simulation method known as the three-dimensional finite-difference time-domain (3D FDTD) is well-known for solving electrodynamics of a system numerically by discretizing the Maxwell equation in the time domain using central-difference approximation (sometimes referred to as Yee lattice) [57, 58].

The details of the method are explained in Appendix B. Although this method can produce accurate predictions of metasurface performance, a high resolution, volumetric simulation of an entire metastructure (300 μm x 300 μm x 40 μm with 1 nm resolution) over sufficient time to observe the ring down of high Q resonant modes, can take significant computation time (e.g. 5-10 hours for a desktop computer) and therefore makes iterative designing difficult.

Therefore, we also employ a second simulation method known as the lattice sum approach (LSA)[59, 60] to calculate the transmission spectra. In this model, we calculate a single particle's effective polarizability by considering the change in the local field experienced by the particle due to the contribution of the surrounding neighbour particles in the lattice. Using this model, we can calculate the transmission spectra using the effective polarizability, and many works have confirmed the accuracy of the LSA model [14, 16]. The simulation time of LSA (typically $\sim$5 minutes) is much faster than FDTD (typically few hours). The explanation of the method is explained in Appendix C.

Using the LSA method to quickly explore the parameter space and FDTD to numerically confirm promising designs, we could rapidly optimize the Q-factor of the plasmonic metasurface. In Fig. 4.3a [14], a metasurface consisting of rectangular gold nanoparticles was proposed to produce a very high-Q SLR. Using FDTD and LSA model, they gradually tuned the size and the periodic spacing in x- and y-axis (P_x and P_y, respectively) to optimize the Q-factor of SLR. Since the light is x-polarized with respect to the metasurface (shown in Fig. 4.3a), the SLR wavelength depends on the P_y and the background refractive index, n_{BG} (As mentioned in Eq. 4.2). The authors set P_y= 1063 nm so that the SLR wavelength would occur at the telecom wavelength. After a series of simulations, they optimized the particle size to be L_y= 200 nm and L_x= 130 nm. These devices were fabricated and the authors used a supercontinuum laser source to excite these metasurfaces of nanoparticles to induce both the LSPR and SLR. This work produced thee highest experimental Q-factor of 2340, the highest observed to date in a plasmonic metasurface. Furthermore, this experimental result is in excellent agreement with the LSA calculation (Fig. 4.3b). In the next section, we discuss the methods that generate multiple SLR modes.

4.3 Generating multiple SLRs

We are interested in a plasmonic system that can generate multiple surface lattice resonances, with each lattice resonance being independently set. The motivation is simple: many applications require multiple, particular resonances. For instance, frequency comb generation [61, 62], bio-sensing [63], fluorescence enhancements [64], and nonlinear four-wave mixing process[18]. The mentioned applications also require that the resonance wavelengths be easily set.

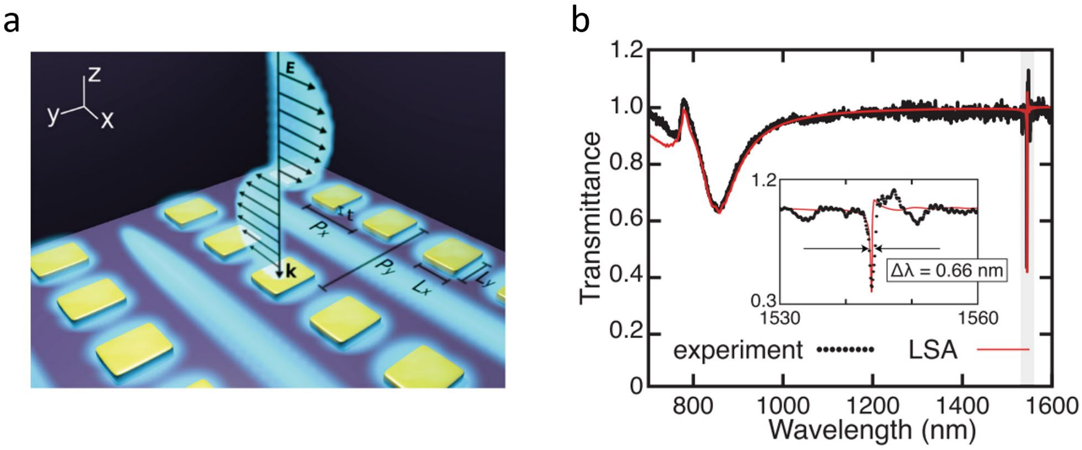

FIGURE 4.3: High-Q plasmonic metasurface(a) the illustration of the system. the metasurface consists of multiple rectangular nanoparticles with the size defined as L_x and L_y. The periodic spacing between particles in x- and y-axis is labelled as P_x and P_y respectively. (b) The experimental transmission spectra (black dots) and the LSA-calculated transmission spectra (red line). The insert figure shows the zoom-in plot of SLR. The corresponding Q-factor is 2340. Image adapted from [14].

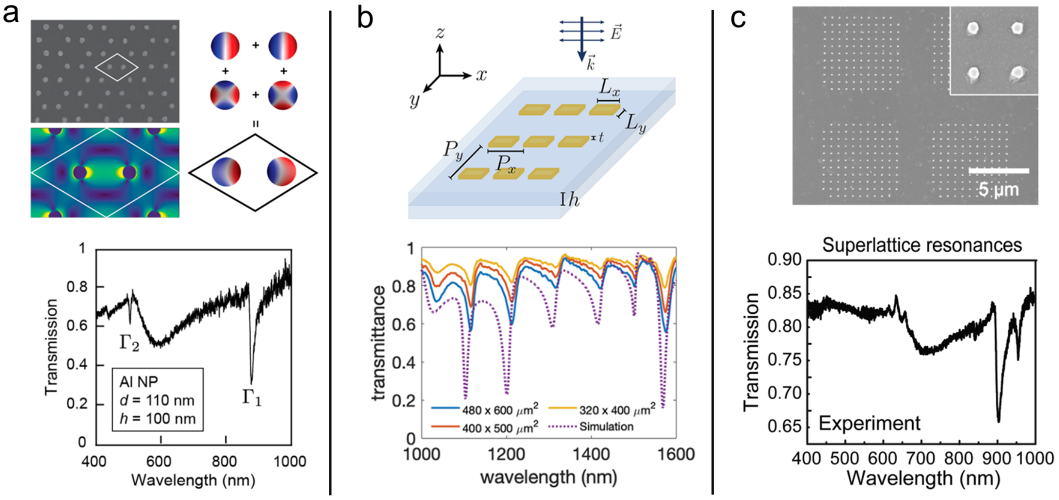

FIGURE 4.4: Various proposed methods to generate multiple SLRs. Images adapted from [15, 16, 17] with permission.

There are many techniques used to generate and tailor multiple SLRs [65, 16, 17, 15]. Figure 4.4 shows some examples of the techniques that generate and manipulate multiple lattice resonances. First, Li et al. have studied the optical properties of a system of plasmonic nanoparticles arranged in the honeycomb pattern (Fig. 4.4a, top panel) [15]. Due to the honeycomb lattice arrangement, the particle experienced anisotropic near-field distributions enhancement, leading to the generation of multiple SLR modes. They measured the transmission spectra as a function of incident laser wavelengths (Fig. 4.4a, bottom panel), and the SLR modes labelled as Γ_1 and Γ_2 were observed. However, the spectral positions of these two resonances can not be independently manipulable. Independent control of the resonant wavelength of each SLR mode would be necessary to produce tailored metasurfaces for particular applications.

Next, our group has experimentally induced multiple SLRs by adding a thin layer of cladding [16]. The top panel of Fig. 4.4b illustrates the basic concept of their proposed system. The system consists of a metasurface with periodic lattice arrangement and a cladding layer with a thickness of h. Since the cladding has a finite thickness and acted as an effective Fabry-Perot (FP) cavity, some portions of the light are trapped and repeatedly interacted with the nanoparticles, inducing multiple SLRs. These unique SLR modes are referred to as FP-SLR modes. They fabricated a set of metasurfaces with different lattice size and measured their transmission spectra. The measured transmission spectra are shown in the bottom panel of Fig. 4.4b, and the experimental results are in good agreement with the FDTD simulation. However, the regular spacing (in the frequency domain) between each FP modes is dictated for each mode by the slab thickness, so each modes resonant wavelength cannot be individually tuned for a particular application.

The third example of existing multiple SLRs strategies considers superlattice plasmons. Wang et al. have fabricated a set of metasurfaces with a superlattice arrangement (top panel of Fig. 4.4c) [17]. Consider a single-patch lattice in the figure; it is equivalent to a periodic lattice. When a few single-patch lattices are close to each other, a coupling is induced between each lattice, leading an additional SLR mode generation. The authors have shown that this coupling can be described by the interaction between single-patch lattice plasmons and Bragg modes determined by the periodic spacing of the patch. They have measured the transmission spectra of the metasurface and shown the confirmation of the additional SLR mode (bottom panel of Fig. 4.4c). However, this strategy has similar limitations to the previous two examples: the resonance wavelengths can not be independently tuned.

There are also other efforts to produce multiple SLRs in a single metasurface, such as introducing periodic vacancy [66], and using V-shaped antenna [67]. However, most of these proposed metasurfaces suffer a similar problem: the SLR wavelengths are restricted in the spectral positions, meaning that the lattice resonance wavelengths can not be chosen freely.

We propose an alternative approach: generate multiple lattice resonances by breaking the periodicity of the lattice. If we can produce a design protocol where the breaks in symmetry can produce resonances at specified wavelengths, this would give us the design freedom the aforementioned applications might require. Specifically, we start by considering how such arrays can be quickly simulated by LSA. In addition to this brief explanation, a more detailed derivation of LSA itself is presented in Appendix C. Initially, we make the assumption that the array is infinite with identical particles, such that we obtain the polarization, $\mathbf{P}$, of any particle in the array as:

$$\mathbf{P}(\omega) = \frac{\epsilon_0 \alpha(\omega) \mathbf{E}_0}{1 - \epsilon_0 \alpha(\omega) S(\omega)}, \tag{4.3}$$

where $\alpha(\omega)$ is the polarizibility of single particle, $\mathbf{E}_0$ is the applied light field, and $S(\omega)$ can be understood as the contribution of all neighbouring particles. $S(\omega)$ depends on the physical positions of the neighbouring particles, and it gives us the outcome of the spectral position of the lattice resonance. In other words, spectral position of the lattice resonance is inter-related to the physical position of the particles. We will show that such relationship can be connected by considering Fourier transform of a lattice with the details of this method explained in Chapter 5. We refer to this technique as Fourier lattice resonance (FLR) and using this technique, we are able to generate multiple lattice resonances in a single metasurface and freely choose the lattice resonance wavelengths of interest. In the next section, we discuss the fabrication process we used.

4.4 Metasurface fabrication

For this work, we fabricated metasurfaces consisting of gold rectangular nanoparticles using a standard lift-off method. The fabrication procedure is as follows (Fig. 4.5): We first started with a fused silica substrate and deposit a positive-tone resist bilayer, this bilayer is made of PMMA with two different molecular weights (Fig. 4.5a and b). Then, we used standard electron-beam lithography to create a desired pattern for the gold nanoparticles on a fused silica substrate (Fig. 4.5c).

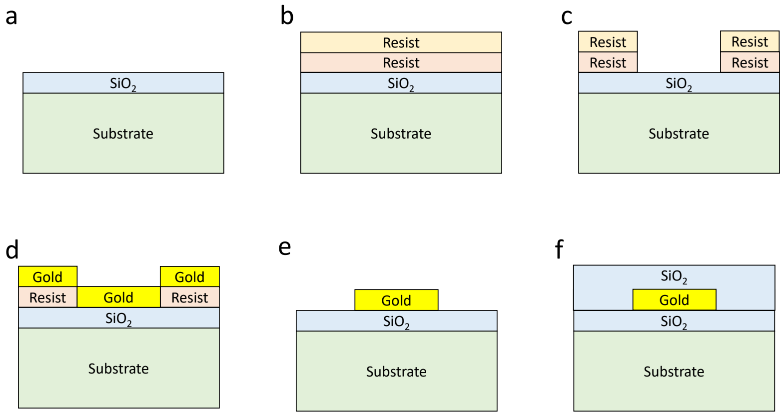

FIGURE 4.5: Fabrication procedures of the metasurface.

After the electron-beam lithography process, we deposited gold using thermal evaporation, and the remaining resists are removed using a lift-off method (Fig. 4.5d and e). Finally, we deposited a layer of silica cladding on top of the metasurface using sputtering technique (Fig. 4.5f).

We also coated an anti-reflective layer on top of the silica top layer with a thickness of 1430 nm to minimize (-30 dB with the wavelength range from 1050 nm to 1700 nm) substrate-related etalon fringes on the backside of the silica substrate.

In Fig. 4.6, the image of a representative device is presented. Each rectangular nanoparticle has a dimension of L_x= 110 nm and L_y= 180 nm, and the spacing between particles is periodic, with P_y= 1063 nm and P_x= 500 nm. The lattice dimensions are $150 \times 150\,\mu\text{m}^2$.

For this work, we are interested in generating multiple lattice resonances using metasurfaces where the spacings between nanoparticles are no longer periodic. The

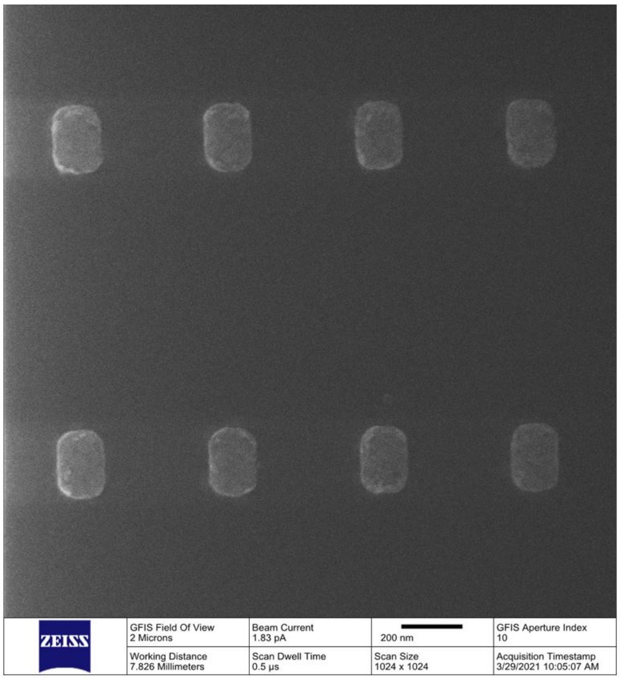

FIGURE 4.6: Helium ion microscopic images of the fabricated metasurface prior to cladding deposition. $P_y = $ 1063 nm

particle locations are predicted by the FLR method. Thus, we fabricated a few sets of metasurfaces to verify our FLR model. The images of the metasurfaces are shown in the paper presented in Chapter 5. In the next section, we describe the experimental setup we implement for our work.

4.5 Experimental setup

We performed a series of linear transmission experiments to measure the transmission spectra of the fabricated metasurfaces. A schematic drawing of the experimental setup is shown in Fig. 4.7.

First, the incident light to excite the metasurfaces is generated from a supercontinuum laser source with a broad wavelength bandwidth (400– 2400 nm). To optimize the experimental results, we have to ensure the light is collimated, meaning that the light has minimal divergence while travelling. To do so, we used a lens to collimate the light source by gradually tuning the lens to its focal length (f= 150 mm).

Next, the collimated light is vertically polarized using a linear polarizing optical filter. The transmitted light propagated through a 4f imaging setup to image the metasurface and used a CMOS camera to capture the image. Once we had located the target metasurface in the image, we isolate it with a pinhole of diameter 100 μm at the middle of the 4f imaging setup and isolate the transmission through the metasurface, otherwise the background light would obscure the lattice resonances. Since we are interested in collecting normalized transmission spectra for our metasurfaces, we also measure the background spectra through just the glass substrate and record the difference of the spectra of these two measurements directly in our optical spectrum

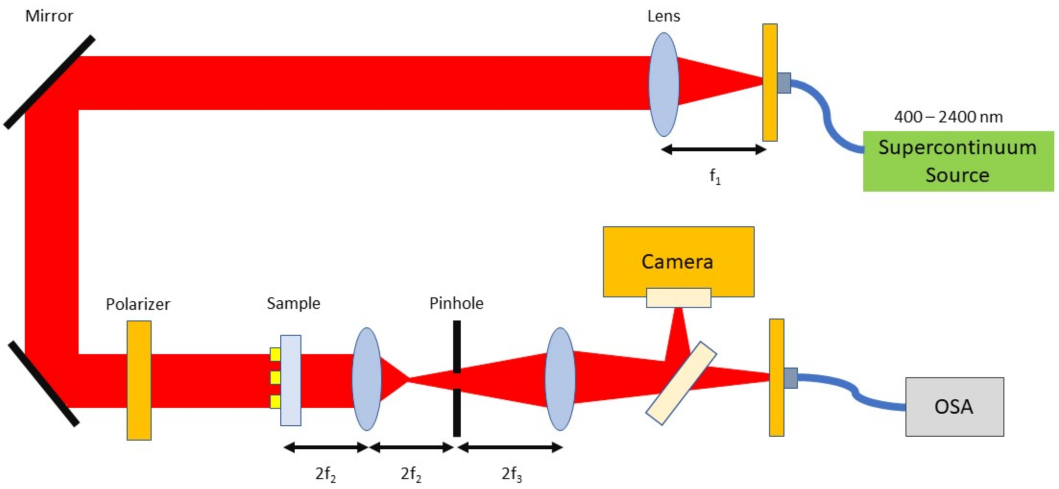

FIGURE 4.7: Experimental setup for transmission spectra measurement.

analyzer (OSA).

The normalized transmission spectra can be shown as:

$$T_{\text{normalized}} = 10\log_{10}\frac{P_{\text{Metasurface}}}{P_{\text{Background}}} \tag{4.4}$$

Where $P_{metasurface}$ is the measured power with metasurface and glass substrate, and $P_{Background}$ is the measured power with only glass substrate. The experimental results and discussion are shown in Chapter 5.

Chapter 5

Fourier-Engineered Plasmonic Lattice Resonances

5.1 Contribution statement

Building on our group's recent successes demonstrating high-Q SLRs in plasmonic metasurfaces, Dr. Orad Reshef suggested investigating the effect of modulated lattice arrangements on SLRs. I used the lattice sum approach (LSA) method to calculate the transmission spectra of modulated lattices, first using a parameter, σ, to break the periodicity of a lattice and observe how an additional SLR mode is generated. Therefore, I plotted Fig. 1 and Fig. 2 using the corresponding FDTD simulation results with their field profiles in the article. Through fruitful discussions, we realized that we could use the Fourier transform of the lattice to model the spectra of these SLR modes. I then performed the calculations which are shown in Fig. 3.

Together, we quickly realized that we could consequently perform an inverse Fourier transform of a particular spectrum of SLR resonances at desired wavelengths to completely determine the necessary nanoparticle positions in the metasurface necessary to produce this spectrum. I generated metasurface designs from arbitrarily selected spectra, which Dr Reshef fabricated (the results are shown in Fig. 4 and Fig. 5). M. Saad Bin-Alam, Yaswant Vaddi, and I designed the experimental setup. Yaswant and I performed the measurements. Dr. Lin Cheng and Dr. Rasoul Alaee calculated the polarizibility of a single nanoparticle for our LSA and FDTD calculations. Dr. Jeremy Upham, Professor Mikko J. Huttunen, Professor Ksenia Dolgaleva, and Professor Robert Boyd supervised the research. I wrote the first draft of the manuscript, which Dr Reshef and the other co-authors revised over several iterations. This work has been published in ACS Nano.

ACS NANO
www.acsnano.org

Fourier-Engineered Plasmonic Lattice Resonances

Theng-Loo Lim, Yaswant Vaddi, M. Saad Bin-Alam, Lin Cheng, Rasoul Alaee, Jeremy Upham, Mikko J. Huttunen, Ksenia Dolgaleva, Orad Reshef,* and Robert W. Boyd

Cite This: *ACS Nano* 2022, 16, 5696−5703 **Read Online**

ACCESS | Metrics & More | Article Recommendations | Supporting Information

ABSTRACT: **Resonances in optical systems are useful for many applications, such as frequency comb generation, optical filtering, and biosensing. However, many of these applications are difficult to implement in optical metasurfaces because traditional approaches for designing multiresonant nanostructures require significant computational and fabrication efforts. To address this challenge, we introduce the concept of Fourier lattice resonances (FLRs) in which multiple desired resonances can be chosen *a priori* and used to dictate the metasurface design. Because each resonance is supported by a distinct surface lattice mode, each can have a high quality factor. Here, we experimentally demonstrate several metasurfaces with flexibly placed resonances (e.g., at 1310 and 1550 nm) and *Q*-factors as high as 800 in a plasmonic platform. This flexible procedure requires only the computation of a single Fourier transform for its design, and is based on standard lithographic fabrication methods, allowing one to design and fabricate a metasurface to fit any specific, optical-cavity-based application. This work represents a step toward the complete control over the transmission spectrum of a metasurface.**

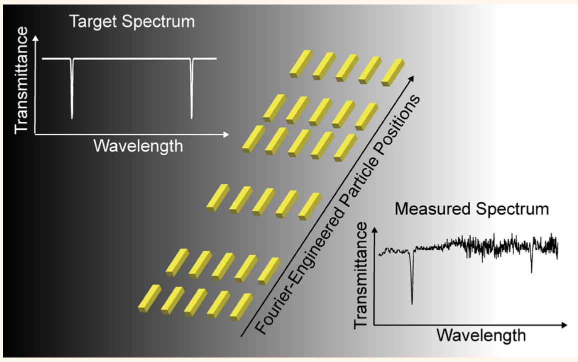

KEYWORDS: *plasmonics, metasurfaces, lattice resonances, nanoparticle arrays, nanophotonics*

Plasmonic nanoparticles are essential tools for the manipulation of light beams in metasurfaces because of the flexibility of the placement of their localized surface plasmon resonances (LSPRs).[1] The LSPR wavelength can be easily tailored since it is highly dependent on the size and the shape of the nanoparticle.[2] Additionally, LSPRs confine light in the nanoscale, leading to significant local-field enhancements.[3] Thanks to these desirable properties, many applications have been realized in a broad range of research fields such as optical filtering,[4,5] harmonic generation,[6] and biosensing.[7] However, the applications of LSPRs are limited by the intrinsic absorption loss of metals; the quality-factor of LSPRs is low (*Q*-factor <10).[8,9] One method to improve the *Q*-factor of resonant plasmonic systems is to consider instead collective optical responses of multiple nanoparticles in a periodic lattice arrangement; such metasurface-scale responses are known as surface lattice resonances (SLRs).[9−12] Unlike the LSPR, the SLR wavelength is defined by the periodicity of the positions of the nanoparticles in a periodic lattice, and this collective response has a relatively high *Q*-factor. For example, our recent work has experimentally demonstrated a *Q*-factor of 2340 around an operating wavelength of 1550 nm.[11]

In addition to improving the *Q*-factor of a lattice response, it is also highly desirable to be able to freely choose the resonance wavelengths of the metasurface.[13,14] The reason is simple: carefully tailoring multiple resonances in a metasurface allows one to customize a metasurface to specific applications, such as frequency comb generation,[15,16] ultrasensitive biosensing,[17] and fluorescence enhancements.[18] For example, methods have been proposed to tune the resonance wavelength by manipulating the dimensions of multiple particles in a single cell,[19] through plasmonic hybridization,[20] and using bound-state-in-the-continuum (BIC) modes.[21] In metasurface systems, several methods have been studied to generate and tailor multiple lattice resonances, such as utilizing multiple materials,[22] adding cladding layers to induce Fabry−Pérot SLR modes,[12] removing nanoparticles periodically,[23] using all-

Received: December 2, 2021
Accepted: March 25, 2022
Published: March 31, 2022

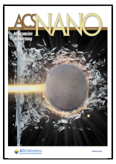

https://doi.org/10.1021/acsnano.1c10710
ACS Nano 2022, 16, 5696−5703

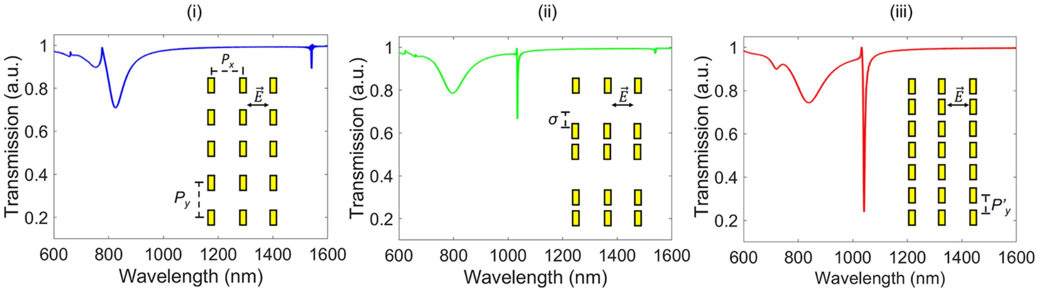

Figure 1. Bipartite Surface Lattice Resonance modes. The transmission profiles of three different lattice arrangements (i), (ii), and (iii) with their corresponding schematic drawings (see the inset figures). These lattice arrangements are made of rectangular nanoparticles, where P_y or P_y' and P_x are the lattice periodicity in the *y*-axis and *x*-axis, respectively. The incident electric field is polarized along the *x*-axis. (i) and (iii) are periodic arrays with lattice constants of P_y and P_y', respectively. For the modulated lattice arrangement (ii), every second row of particles in the array in (i) is translated by spacing $\sigma = P_y/3$. Such a system resembles the array of (iii) but with vacancies.

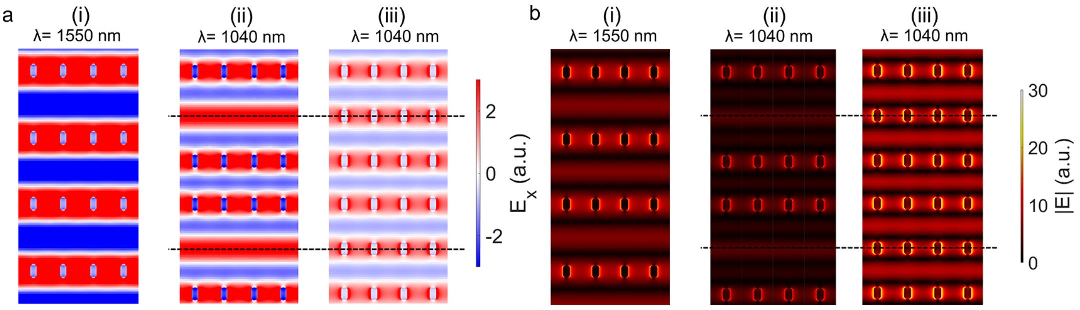

Figure 2. Near-field profiles of the lattice modes. (a) The normalized *x*-polarized electric field profiles of lattice arrangements from Figure 1, their respective SLR resonances of 1550 nm for (i) and 1040 nm for (ii) and (iii). The vacancies in every second row of the unit cell (ii) are aligned with every second row of the particles of the unit cell in (iii) (the black dashed line). The electric fields in (ii) resemble those of (iii), indicating that a similar mode is being excited. (b) The electric field amplitude profiles of the lattice arrangements, showing the field enhancement at the resonances. These results also demonstrate that all of the SLR modes possess a field enhancement within the same order of magnitude.

dielectric Mie-resonance metasurfaces,[24] and superlattice arrays.[25] Each of these methods can support multiple resonance modes; however, they are all limited in the spectral position or number of these resonances. Some methods have been developed that can define any number of resonances in flexible locations in a metasurface. In this work, we tackle this issue by exploiting a different approach: by breaking the lattice periodicity, we show that we can simultaneously introduce multiple lattice resonances with tunable resonance wavelengths. With this knowledge, we introduce and experimentally demonstrate the concept of Fourier lattice resonances (FLRs), which are a natural generalization of SLRs that can support multiple lattice resonances at desired operation wavelengths.

RESULTS AND DISCUSSION

Interpretation of Fourier Lattice Resonances (FLRs).

For conceptual clarity, we begin by exploring how perturbations in translational symmetry introduce resonances. This demonstration helps interpret the physical origin of FLRs. Note that the main goal of this manuscript is *not* to reintroduce bipartite lattices,[26−29] but to motivate the theory that we will develop later on for FLRs. Consider a metasurface consisting of rectangular gold nanoparticles with a periodic lattice arrangement. The lattice is embedded in a homogeneous background of silica glass ($n \sim 1.45$), with particle dimensions of L_x = 110 nm and L_y = 180 nm and periodicities of P_x = 500 nm and P_y = 1063 nm (see the inset in Figure 1(i)). The predicted transmission spectrum for an *x*-polarized beam is calculated by the finite-difference time-domain (FDTD) method and is shown in Figure 1(i). The LSPR mode of the metasurface occurs at an operating wavelength of 830 nm, and the SLR is at 1550 nm ($\lambda_{\mathrm{SLR}} \approx nP_y$). Next, we break the symmetry of the rectangular lattice by displacing every second row of particles by a distance $\sigma = P_y/3$ (see the inset in Figure 1(ii)). The calculated transmission profile of the metasurface is altered by this modulation (Figure 1(ii)): an additional collective resonance arises at 1040 nm. The origin of this resonance is clear when looking at Figure 1(iii), where we show a rectangular lattice of periodicity $P_y' = 2P_y/3$; the altered lattice in Figure 1(ii) resembles a sparser version of Figure 1(iii). The additional resonance is, therefore, just an SLR corresponding to the effective periodicity P_y', with an additional resonant wavelength $\lambda_{\mathrm{SLR}}' = nP_y'$. This is further supported by examining Figure 1(iii), which shows the corresponding transmission profile with $P_y' = 2P_y/3$. Hence, the altered lattice arrangement can be viewed as combinations between two different periodic lattice arrangements. Such bipartite array lattice systems[26−29] have extensively been studied, and our numerical results are consistent with these studies.

We next examine the near-field profile of the metasurface. Figure 2a illustrates the *x*-polarized electric field of all three lattices shown in Figure 1. If we compare the electric field profile in Figure 2a (ii) with that of another perfect lattice arrangement with a periodicity of $2P_y/3$ at a wavelength of 1040 nm (Figure 2a (iii)), the same SLR modes are excited at the same wavelength. Hence, the additional SLR can be

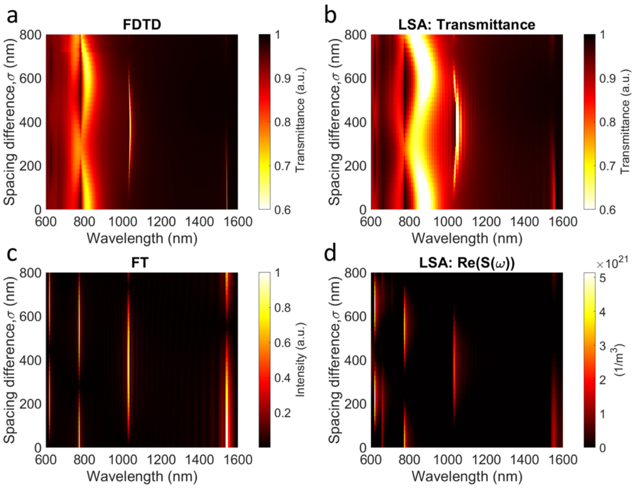

Figure 3. The evolution of the aperiodic SLR mode. (a) The FDTD-calculated transmission profiles with respects to the spacing difference σ. (b) LSA-simulated transmission spectra plotted as a function of σ. The calculated LSPR and SLR modes are largely consistent with the calculations in (a). (c) The FT-calculated power spectra with varying σ. (d) The LSA-simulated real part of lattice sum function, Re($S(\omega)$), plotted as a function of σ. The spectral features are consistent with the FT calculations in (c).

regarded as an SLR mode with a periodicity of $2P_y/3$, but missing particles.

To observe the emergence of this SLR mode, we perform a series of FDTD simulations as a function of σ. We present the simulation results in Figure 3a. As shown in this figure, for σ = 0 nm, the new SLR does not appear at 1040 nm since the lattice arrangement is still rectangular. As σ gradually increases, the periodic SLR mode at 1550 nm starts to vanish due to the cancellation produced by the particle in the unit cell being located at the antinodes of the electric field with opposite sign, and a different SLR mode begins to appear when σ is changed from 80 to 640 nm at a wavelength of 1040 nm. The most pronounced resonance occurs when $\sigma \approx 354$ nm since this corresponds to approximately a period of $2P_y/3$.

We employ the lattice sum approach (LSA)[30,31] to gain further insight into these metasurfaces. In this model, the effective polarizability induced in a single particle can be calculated by taking into account the change in the local field experienced by the particle due to the rescattered fields of the surrounding neighbor particles in the lattice. One of the main advantages of this method is that the computation time is much faster compared to a standard FDTD simulation with a superlattice element with periodic boundary conditions.[11,12] On a standard desktop computer, the LSA simulations of a 150 × 150 μm^2 lattice for the 2790 antenna placements shown in Figure 3a took ~1 min for the entire spectral sweep (600−1600 nm), whereas the FDTD simulations of two-particle superlattices with periodic boundary condition took ~1 h. Clearly, the FDTD calculation of complete metasurfaces is computationally prohibitive. In this paper, we modify the lattice sum by including the effect of σ with a lattice size of 150 × 150 μm^2, and perform the corresponding calculations concerning σ, as illustrated in Figure 3b (see also Methods). By comparing this result with that shown in Figure 3a, we demonstrate that the transmission spectra obtained by LSA calculations are in excellent agreement with FDTD simulations in terms of predicting the resonance wavelengths for the LSPR and SLR.

We are now ready to introduce the theory behind FLRs. The two SLRs in our example originate from the various periodicities present in the lattice (P_y and $2P_y/3$). Any discussions of periodicities naturally suggest the possibility of using Fourier series; indeed, we find that taking a Fourier transform (FT) of the particle locations may reveal the positions of the resonances. This idea is the essence of the design methodology of FLR metasurfaces. To demonstrate this idea by way of an example, we represent the lattice using the function $f(y)$; this function consists of a series of Gaussian profiles centered at the y-coordinates of individual nanoparticles, with a spacing corresponding to the periodicity of the actual lattice, P_y, between each profile (see Methods). We generate a series of different $f(y)$ functions for a range of values of σ (σ = 0 to 800 nm); these different $f(y)$ functions each represent a different lattice with increasing amounts of symmetry-breaking. We then take the FTs of each of these functions, and plot the resulting power spectra in Figure 3c. We compare this result to that of Figure 3d, which shows the LSA-simulated real part of lattice sum function, Re($S(\omega)$), also as a function of σ (see eq 2). The resemblance between these two figures is evident upon inspection: the power spectrum (Figure 3c) in the FT calculation has peaks in the exact wavelengths where the Re($S(\omega)$) calculation (Figure 3d) features the lattice resonances. This agreement indicates that these additional SLRs can be predicted with a simple FT of the perturbed lattices; we call this predictive design approach the Fourier lattice resonance (FLR) method. Although the SLRs for this particular lattice geometry can also be trivially explained using the Rayleigh Anomalies (RA),[32] our model introduces an additional degree of freedom in designing metasurfaces. Given that the RA model depends on periodic structures, there are many lattice arrangements which it can not treat. We can therefore view our treatment, which can consider even aperiodic lattices, as a generalization of the RA model. The additional degree of freedom will be discussed in a subsequent section.

Experimental Verifications of FLRs. To experimentally verify the FLR model, we fabricated two sets of metasurfaces consisting of rectangular nanoparticles. In Figure 4a, the images of the devices are presented; each subfigure in Figure 4a represents the actual device with different values of σ, and with a P_y of 1063 nm. This set of metasurfaces has nanoparticle dimensions of L_x = 110 nm and L_y = 180 nm, and lattice sizes of 150 × 150 μm^2. The calculated transmission spectra for these devices are shown in Figure 4b and are in good agreement with the experimental data in Figure 4c. The experimental setup and procedure are described in the Methods. As predicted, the periodic SLR mode at 1040 nm vanishes as σ decreases. Furthermore, a new SLR starts arising when σ = 88 nm, and is most prominent when σ = 354 nm, which agrees with the LSA and the FDTD simulations, supporting our theoretical interpretation. Notably, the Q-factors of this set of devices range from 80 to 90, and the sharpest aperiodic SLR dip has a Q-factor of 90 with P_y = 1063 nm and σ = 354 nm.

Our model also works with different values of P_y. Here, we fabricated another set of metasurfaces with P_y = 1598 nm (Figure 4d) and the same nanoparticle sizes as the first set of the devices. Similarly to the first set of metasurfaces, the simulated transmission profiles of the second set of

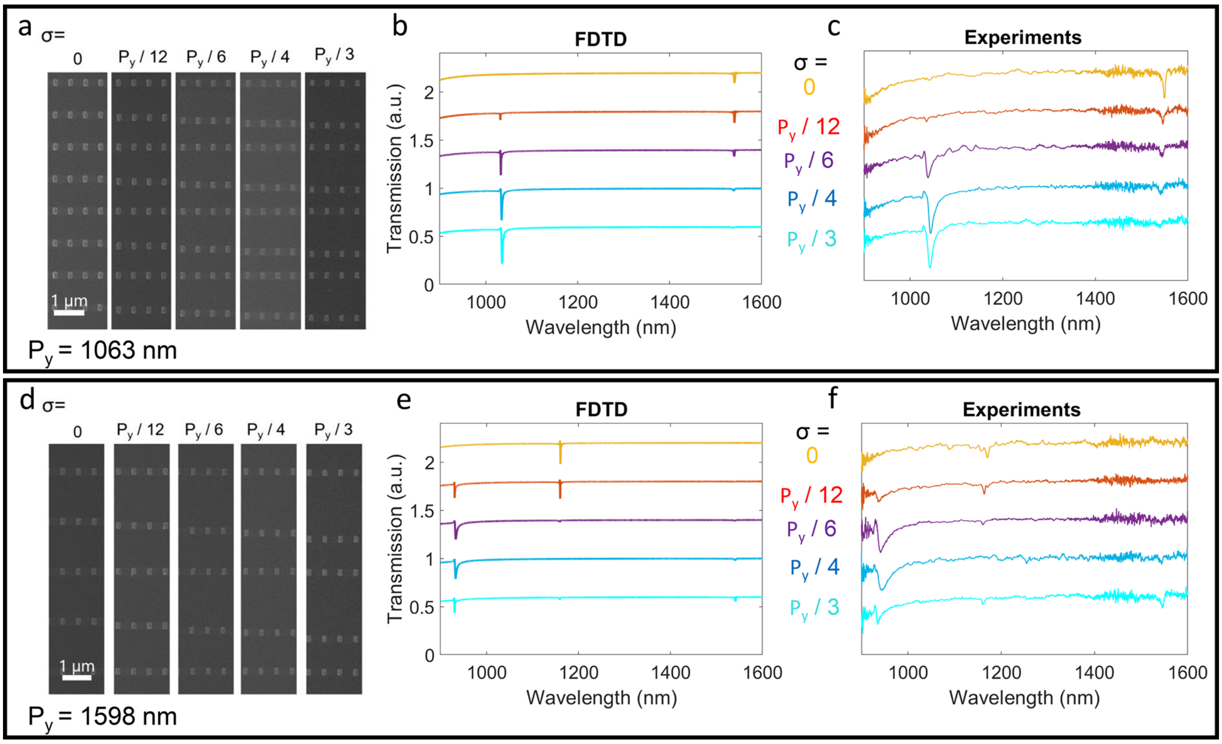

Figure 4. Experimental observation of metasurfaces with multiple SLR modes. (a,d) Helium ion microscopic images of the fabricated metasurfaces prior to cladding deposition. Each subfigure corresponds to an image with a different σ. For (a), all metasurfaces have P_y = 1063 nm, whereas for the metasurfaces in (d), P_y = 1598 nm. (b,e) The simulated transmittance of the corresponding metasurfaces with (b) P_y = 1063 nm and (e) P_y = 1598 nm. (c,f) The measured transmission spectra of the metasurfaces with (c) P_y = 1063 nm and (f) P_y = 1598 nm.

metasurfaces (P_y = 1598 nm) in Figure 4e are also in good agreement with the experimental data (Figure 4f), where a new SLR mode for this system is predicted to occur at 1550 nm and σ = 354 nm. Despite the extinction coefficients of the resonances in these metasurfaces being smaller than the first set, the *Q*-factors of these devices are relatively higher. The *Q*-factors range from 170 to 220, where the lattice resonance with the highest *Q*-factor appears at 1150 nm and σ = 532 nm. In the first set of devices, the spectral distance between the SLR at 1550 nm and the second SLR in our spectrum was 504 nm, in the second set, the distance is only 381 nm. This hints at the flexibility of modulated lattices to place SLRs at flexibly spectral locations.

We have just shown that the LSA succeeds at describing the transmission spectra of a modified lattice arrangement. However, a discrepancy arises in the *Q*-factor predicted by this method when compared to FDTD simulations and the experimental results, which we attribute to the difference in array size.[33,34] Because the nanoparticle density in the second set of metasurfaces is smaller although the array size is the same, the extinction ratio and *Q*-factor are lower than in the first set, making the second set of metasurfaces harder to characterize.

Reverse-Engineering of FLRs. Since the properties of the SLRs in bipartite lattices can be predicted by using the FLR method, in principle, the process can be reverse-engineered: one could begin with the desired transmission profile, then use the FT of that spectrum to directly engineer the nanoparticle placement to generate the desired spectrum. To demonstrate this idea, we first select a set of desired resonance wavelengths and create a virtual spectrum (Figure 5a), where we are deliberately placing two SLRs at 1150 and 1220 nm. We also include replicas of these two desired resonances represented as integer Nth harmonics in this virtual spectrum because there will naturally appear higher-order diffraction terms at $\lambda_{SLR}/2$, $\lambda_{SLR}/3$, *etc* for any lattice resonance (see Methods). Thus, the FT-simulated transmission profile of a lattice must reproduce these corresponding features. We then take the inverse FT (IFT) of the virtual spectrum (Figure 5a), which is shown in Figure 5b. Furthermore, we acquired the corresponding particle locations using a peak-finder function in Figure 5b and calculated the transmission spectra of the IFT-generated lattice arrangement using LSA with the obtained particle locations (see also Methods for more details). We observe that the corresponding SLR modes for each set are induced at the desired wavelengths (Figure 5d).

Experimental Demonstration of Reverse-Engineered FLRs. To experimentally demonstrate the reverse-engineering capabilities of the FLR method, we fabricate two devices with different sets of resonance wavelengths, one with resonances at λ = 1150 and 1220 nm (FLR1) and another, equivalent lattice prepared for resonances at λ = 1310 and 1550 nm (FLR2), where the array size is 100 × 400 μm^2 for both devices. Figure 5c shows images of subsets of the lattices for the FLR1 and FLR2 metasurfaces. After performing the measurements on these devices, we compare the LSA simulations (Figure 5d) with the experimental data (Figure 5e). The predicted resonance wavelengths from the LSA simulations are in good agreement with the experimental results of both devices. This agreement suggests that this method can be used to design resonance wavelengths flexibly. We also experimentally measured the *Q*-factors for these lattice resonances for both

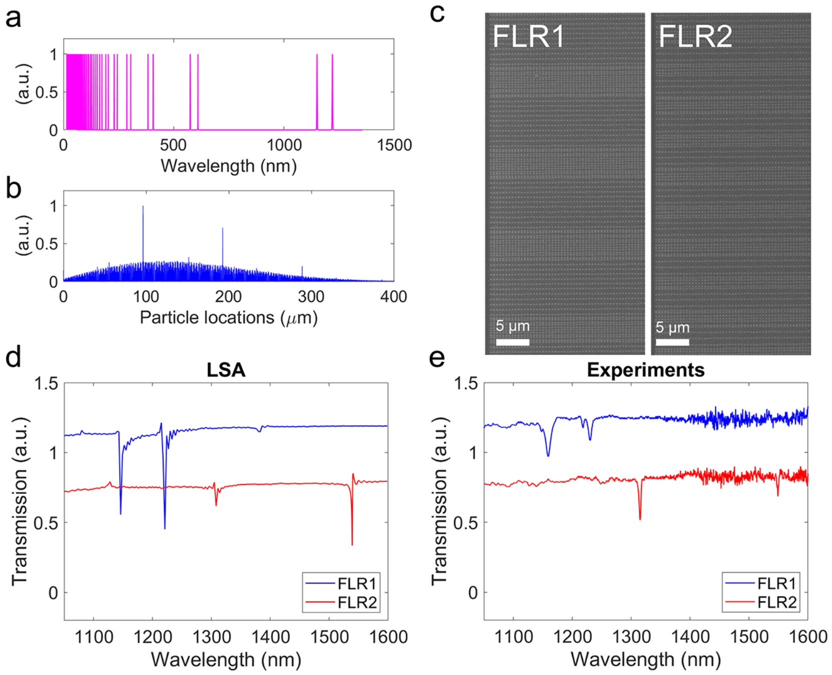

Figure 5. The FLR metasurface. (a) The generated virtual spectrum. We created a spectrum with resonance wavelengths of 1150 and 1220 nm, including their corresponding harmonics since each lattice resonance will naturally generate higher-order diffraction terms. The vertical axis of the figure is the virtual beam intensity, which we set to unity. (b) The IFT of the virtual spectrum. The *x*-axis of the diagram indicates the corresponding particle locations for the desired wavelength combination. The vertical axis of the figure is IFT power spectrum intensity; we employ a peak-finder function with a small threshold (0.015) to determine the particle locations. The superlattice for FLR1 is nonrepeating over ~20 antenna in *y*-axis (here equivalent to ~6 μm^2), making FDTD simulation of this device prohibitive, but still possible with LSA. (c) SEM images of subsets of the lattices for FLR1 and FLR2 metasurfaces. (d) Calculated transmission spectra of the FLR metasurfaces using LSA method. The SLRs arise at the desired wavelengths. (e) The measured transmission spectra of the corresponding FLR metasurfaces.

samples. The experimental *Q*-factors of the lattice resonances in the FLR1 metasurface are 130 at λ = 1150 nm and 200 at 1220 nm, and the experimental *Q*-factors for the FLR2 metasurface are 400 at λ = 1310 nm and 800 at 1550 nm. Fabricating the same device with a larger array size would likely increase the depth and *Q*-factor of the resonances.[11,12,34] These agreements also imply that the LSA model can be used for calculations of aperiodic lattice array.[9,11,12]

The highest Q-factor of these FLRs is 800 (FLR2, at a wavelength of 1550 nm), which is 2 orders of magnitude higher than those associated with the LSPRs of the individual nanoparticles and an order of magnitude higher than that of Fabry−Pérot SLR modes.[12] With such high Q-factors and the strong optical nonlinearity of metals,[35] the FLR metasurfaces could find applications in nonlinear processes, such as nondegenerate four-wave mixing (FWM).[36]

To consider how existing approaches could be complemented by our FLR method, we consider a few recent, key examples from the literature: a recent work showed that a single dielectric nanoparticle could be engineered to have multiple resonances, some of which showed *Q*-factors ~190.[37] This required careful simulation of the nanoparticle dimensions and precise fabrication. By comparison, our FLR method could likely design a metasurface with similar multiple resonances from the spectrum itself. Obviously the nature of the resonators themselves are very different, but this exemplifies the ease of our design approach. Other related attempts in generating multiple resonances such as inducing Fabry−Pérot SLRs using a cladding,[12] and using orthogonal polarizations[38,39] in the lattice are often restricted to resonances that are periodic in frequency. Our method is not restricted to periodic resonances, and it only assumes dipole effects of the particles, leading to more straightforward computations.

Designing the FLR metasurface using standard FDTD simulations would be exceptionally challenging because the lack of symmetry in the lattice eliminates the possibility of simulating a small supercell, and the computational time increases with the size of the lattice arrangement.[40] In contrast, the computational time required by the FLR method is reasonable (typically within 3 min), necessitating the computation of only a single FT per lattice.

Other recent work has computed FTs to determine the 3D structure of a surface for applications in optical wavefront shaping; thus, fabricating such structure requires more sophisticated techniques.[14,41] By contrast, our work aims to find a desired transmission spectrum, and our method only utilizes standard electron-beam lithography techniques instead of 3D structures, which leads to a more straightforward fabrication.

Other related work has extensively demonstrated designing multilayer thin film stacks using FTs for applications in optical filtering.[42] Noting the similarity of our work to the study of ref.,[42] we believe that our methodology could be further extended to 3D lattices by combining our design method with the developed analytical method.

Future work on this platform could look into modifying the nanoparticle geometries to tune the width and depth of the individual resonances. Furthermore, we only took the position of the particle locations and ignored the magnitude of the peaks in the power spectrum when performing the IFTs. Some information is encoded in these magnitudes on the scattering amplitude of individual nanoparticles in the array. This information could perhaps be incorporated in future metasurfaces to modulate the individual extinction ratio of each resonance. Moreover, other more complex systems can be examined using our method, but are left for future studies. For example, the system could consist of arrays with complex unit cells in which the particles are placed at positions with arbitrary x- and y-coordinates, or we could consider excitation at an oblique incidence, or with the polarization not aligned to one of the array axes.

The Q-factor of the FLRs can be increased further by using dielectric particles. However, in those cases, higher-order multipoles would need to be taken into consideration.[37] In this work, we did not modify the arrangement of the particles in the x-direction. We note that such modifications should give rise to a different set of resonances that could be excited by using orthogonal polarization, that is, y-polarized light.[38] One possible application would be to modify the LSA calculations to generate orbital angular momentum (OAM) modes by introducing particle size disorders or different particle geometries.

CONCLUSIONS

We have theoretically proposed and experimentally demonstrated the concept of FLRs. The fabricated devices in this paper enable SLRs at multiple simultaneous wavelengths, and the experimental results are in good agreement with our FLR calculations. Additionally, these devices require only a standard fabrication procedure, and they can be easily expanded upon to generate multiple resonances that can be placed nearly flexibly within a spectral octave. From a broader perspective, this method is possible because we exploit a previously ignored degree of freedom by breaking the lattice periodicity, and this modeling is only possible thanks to large-scale modeling techniques like LSA. We anticipate that this design method will become significant in realizing resonant metasurfaces for many optical applications.

METHODS

Simulation. *FDTD Simulations.* A commercial three-dimensional finite-difference time-domain (FDTD) software package is utilized to perform full-wave simulations for single rectangular nanoparticles, periodic metasurfaces, and modulated metasurfaces. For the single nanoparticle simulations, the total-field scattered-field (TFSF) method is used to extract the single particle polarizability in all three dimensions: α_{xx}, α_{yy}, and α_{zz}.[43] For the periodic and modulated metasurfaces, a single unit cell was simulated using periodic boundary conditions in the in-plane dimensions and perfectly matched layers in the out-of-plane dimension. All three cases were modeled using fully dispersive optical material properties for silica and for gold.[44] Minimal artificial absorption ($\mathrm{Im}(n) \approx 10^{-4}$) was added to the background medium to reduce numerical divergences.

Lattice Sum Approach. The lattice sum approach (LSA) is a simplified version of the discrete-dipole approximation (DDA) method.[30,31] The main difference between these two methods is that the LSA assumes that the dipole moments of all interacting nanoparticles are identical. Thus, the dipole moment of any nanoparticle can be simplified as

$$\mathbf{p} = \frac{\epsilon_0 \alpha(\omega) \mathbf{E}_{\mathrm{inc}}}{1 - \epsilon_0 \alpha(\omega) S(\omega)} \equiv \epsilon_0 \alpha^*(\omega) \mathbf{E}_{\mathrm{inc}}, \tag{1}$$

where the effect of interparticle coupling is incorporated in the lattice sum $S(\omega)$, $\alpha^*(\omega)$ is the effective polarizability, and $\alpha(\omega)$ is the single nanoparticle polarizability obtained from the TFSF method. The $S(\omega)$ can be written as

$$S(\omega) = \sum_{j=1}^{N} \frac{\exp(\mathrm{i}kr_j)}{\epsilon_0 r_j} \left[k^2 + \frac{(1 - \mathrm{i}kr_j)(3\cos^2\theta_j - 1)}{r_j^2} \right] \tag{2}$$

where r_j is the spacing to the jth dipole, k is the wavenumber, and θ_j is the angle between r_j. For a periodic metasurface, r_j is just the periodicity P_v multiplied by j and the indices v indicates the x- or y-axis.

Fourier Transform of the Function f(y). The function $f(y)$ that mimics the lattice arrangement is considered by producing a series of Gaussian profiles. Each Gaussian profile represents a nanoparticle, and the Gaussian peak intensity is set to 1. We set the bandwidths of these Gaussian profiles to be significantly smaller than the spacing between the particles (bandwidth-to-spacing ratio is ∼100); thus, we can assume that the particles act like point-like dipoles under the applied incident field, similar to the assumption made in the LSA model. Next, the spacing between each Gaussian profile is P_y in the periodic case. When we considered a modulated lattice arrangement, the position of every second nanoparticle was shifted by σ. Then, we performed FT of the function with respects to y-axis, and we obtained the density plot in Figure 3c.

Combining LSA and IFT Calculations. We generate a function $f(y)$ as explained in the main text and previous subsection. This function contains a series of Gaussian peaks: two of them are placed at the desired resonance wavelengths (e.g., 1150 and 1220 nm); the remaining ones are placed at the integer harmonics for each resonance (e.g., 575 nm, 383.3 nm, 287.5 nm, ...and 610 nm, 406.7 nm, 305 nm, ..., respectively). These resonances correspond to the Rayleigh anomalies (RA) for $m = 0$:

$$\lambda \sim \frac{n}{\sqrt{\left(\frac{j}{P_y}\right)^2 + \left(\frac{m}{P_x}\right)^2}}, \tag{3}$$

where n is the refractive index, and j and m are the RA orders along the y- and x-axis, respectively. As we only consider $m = 0$ cases to simplify our model, only x-polarized beams are taken into account and P_y makes the only contribution to the system. All profiles have the same intensity, and the full width at half-maximum (fwhm) of the profiles are significantly smaller than their separation (the fwhm-to-spacing ratio is ∼100). Hence, we obtain the plot shown in Figure 5a.

We then perform an IFT of $f(y)$ (Figure 5b). The x-axis is inverted so that we are plotting against units of length instead of inverse-length. We identify the locations of the peaks in Figure 5b using a peak-finder function. The resulting list of locations correspond to the locations of the centers of the nanoparticles needed to generate the spectrum in Figure 5a.

To avoid overlap between neighboring particles, and to ensure the possibility of nanofabrication, we enforce a minimum distance between the centers of nanoparticles, here set to 250 nm. We also truncate the total number of particles at the ends of the arrays to obtain a desired array size, here 400 μm.

To determine the transmission spectra of the IFT-simulated lattice arrangement, we insert the calculated particle locations (Figure 5b) into r_j in the y-axis in eq 1. We obtain the corresponding effective $S(\omega)$ which we use to calculate α^* to determine the effective dipole moment using eq 2. We finally use α^* to obtain the transmission spectra shown in Figure 5d.

Fabrication. The metasurfaces are fabricated using a standard metal lift-off process and a positive-tone resist bilayer. We started with a fused silica substrate and defined the pattern using electron-beam lithography with the help of a commercial conductive polymer. The mask was designed using shape correction proximity error correction[45] to compensate for corner rounding. Following the development, gold was deposited using thermal evaporation. The final silica cladding layer was deposited using sputtering. The backside of the silica substrate was coated with an antireflective coating to minimize substrate-related etalon fringes.

Experimental Setup. A collimated broadband supercontinuum laser source was used to illuminate the devices with a wavelength spectrum ranging from 470 to 2400 nm. We used a linear polarizing optical filter to control the light beam polarization. Then, the light beam was transmitted through the device and a lens imaged the sample onto the detector array. We placed a pinhole with a diameter of 100 μm in the image plane to choose the desired metasurface. After that, the remaining light beam was guided into a multimode fiber with a diameter of 400 μm, which was coupled into an optical spectrum analyzer. Finally, we normalized the transmission spectrum of the light beam to a background trace of the substrate without gold nanostructures.

ASSOCIATED CONTENT

Supporting Information

The Supporting Information is available free of charge at https://pubs.acs.org/doi/10.1021/acsnano.1c10710.

> Multiple simulated transmission profiles for a series of FLR metasurfaces with different combinations of arbitrarily selected resonance wavelengths have been demonstrated (PDF)

AUTHOR INFORMATION

Corresponding Author

Orad Reshef − *Department of Physics, University of Ottawa, Ottawa, Ontario K1N 6N5, Canada;* orcid.org/0000-0001-9818-8491; Phone: +1 (613) 562-5800 ×7138; Email: orad@reshef.ca

Authors

Theng-Loo Lim − *Department of Physics, University of Ottawa, Ottawa, Ontario K1N 6N5, Canada*
Yaswant Vaddi − *Department of Physics, University of Ottawa, Ottawa, Ontario K1N 6N5, Canada*
M. Saad Bin-Alam − *School of Electrical Engineering and Computer Science, University of Ottawa, Ottawa, Ontario K1N 6N5, Canada*
Lin Cheng − *School of Instrument and Electronics, North University of China, Taiyuan 030000, China*
Rasoul Alaee − *Department of Physics, University of Ottawa, Ottawa, Ontario K1N 6N5, Canada;* orcid.org/0000-0003-2187-4949
Jeremy Upham − *Department of Physics, University of Ottawa, Ottawa, Ontario K1N 6N5, Canada*
Mikko J. Huttunen − *Photonics Laboratory, Physics Unit, Tampere University, Tampere FI-33014, Finland;* orcid.org/0000-0002-0208-4004
Ksenia Dolgaleva − *School of Electrical Engineering and Computer Science, University of Ottawa, Ottawa, Ontario K1N 6N5, Canada*
Robert W. Boyd − *Department of Physics, University of Ottawa, Ottawa, Ontario K1N 6N5, Canada; Institute of Optics and Department of Physics and Astronomy, University of Rochester, Rochester, New York 14627, United States;* orcid.org/0000-0002-1234-2265

Complete contact information is available at: https://pubs.acs.org/10.1021/acsnano.1c10710

Author Contributions

T.L. and O.R. conceived the basic idea for this work. T.L. and Y.V. conducted the transmission measurements. T.L., O.R., and M.S.B.A. designed the experiment. R.A. and L.C. calculated single particle's polarizability. T.L. and O.R. carried out the simulations. O.R. fabricated the devices. T.L., O.R., Y.V., and J.U. analyzed the experimental results. R.W.B., J.U., M.J.H., and K.D. supervised the research and the development of the manuscript. T.L. and O.R. wrote the first draft of the manuscript, and all authors subsequently took part in the revision process and approved the final copy of the manuscript.

Notes

The authors declare no competing financial interest.

ACKNOWLEDGMENTS

We acknowledge the help of Sabaa Rashid with imaging. We thank Brian T. Sullivan and Graham Carlow for fruitful discussions. Fabrication in this work was performed in part at the Centre for Research in Photonics at the University of Ottawa (CRPuO). This research was undertaken thanks in part to funding from the Canada First Research Excellence Fund and the Canada Research Chairs program. L.C. acknowledges the support of the China Scholarship Council. M.J.H. acknowledges the Flagship of Photonics Research and Innovation (PREIN) funded by the Academy of Finland (Grant No. 320165). R.A. acknowledges support from the Alexander von Humboldt Foundation through the Feodor Lynen Return Research Fellowship. We acknowledge the support of the Natural Sciences and Engineering Research Council of Canada (NSERC) (funding reference number RGPIN/2017-06880, RGPIN/2020-03989, 950-231657, and STPGP/521619-2018). A prereview version of the manuscript has been published on the arXiv preprint server: Theng-Loo Lim; Yaswant Vaddi; M Saad Bin-Alam; Lin Cheng; Rasoul Alaee; Jeremy Upham; Mikko J Huttunen; Ksenia Dolgaleva; Orad Reshef; Robert W Boyd, *Fourier-Engineered Plasmonic Lattice Resonances*, 2021, 2112.11625, arXiv.org, https://arxiv.org/abs/2112.11625 (accessed December 22, 2021).

REFERENCES

(1) Hutter, E.; Fendler, J. H. Exploitation of localized surface plasmon resonance. *Adv. Mater.* **2004**, *16*, 1685−1706.

(2) Maier, S. A. *Plasmonics: Fundamentals and Applications*; Springer: New York, 2007.

(3) Oldenburg, S. J.; Averitt, R. D.; Westcott, S. L.; Halas, N. J. Nanoengineering of optical resonances. *Chem. Phys. Lett.* **1998**, *288*, 243−247.

(4) Yokogawa, S.; Burgos, S. P.; Atwater, H. A. Plasmonic color filters for CMOS image sensor applications. *Nano Lett.* **2012**, *12*, 4349−4354.

(5) Zeng, B.; Gao, Y.; Bartoli, F. J. Ultrathin nanostructured metals for highly transmissive plasmonic subtractive color filters. *Sci. Rep.* **2013**, *3*, 2840.

(6) Palomba, S.; Danckwerts, M.; Novotny, L. Nonlinear plasmonics with gold nanoparticle antennas. *J. Opt. A: Pure Appl. Opt.* **2009**, *11*.114030

(7) Qiu, G.; Gai, Z.; Saleh, L.; Tang, J.; Gui, T.; Kullak-Ublick, G. A.; Wang, J. Thermoplasmonic-Assisted Cyclic Cleavage Amplification for Self-Validating Plasmonic Detection of SARS-CoV-2. *ACS Nano* **2021**, *15*, 7536−7546.

(8) Doiron, B.; Mota, M.; Wells, M. P.; Bower, R.; Mihai, A.; Li, Y.; Cohen, L. F.; Alford, N. M. N.; Petrov, P. K.; Oulton, R. F.; Maier, S. A. Quantifying Figures of Merit for Localized Surface Plasmon Resonance Applications: A Materials Survey. *ACS Photonics* **2019**, *6*, 240−259.

(9) Kravets, V. G.; Kabashin, A. V.; Barnes, W. L.; Grigorenko, A. N. Plasmonic Surface Lattice Resonances: A Review of Properties and Applications. *Chem. Rev.* **2018**, *118*, 5912−5951.

(10) Utyushev, A. D.; Zakomirnyi, V. I.; Rasskazov, I. L. Collective lattice resonances: Plasmonics and beyond. *Reviews in Physics* **2021**, *6*, 100051.

(11) Bin-Alam, M. S.; Reshef, O.; Mamchur, Y.; Alam, M. Z.; Carlow, G.; Upham, J.; Sullivan, B. T.; Ménard, J.-M.; Huttunen, M. J.; Boyd, R. W. Ultra-high-Q resonances in plasmonic metasurface. *Nat. Commun.* **2021**, *12*, 974.

(12) Reshef, O.; Saad-Bin-Alam, M.; Huttunen, M. J.; Carlow, G.; Sullivan, B. T.; Ménard, J. M.; Dolgaleva, K.; Boyd, R. W. Multiresonant High- Q Plasmonic Metasurfaces. *Nano Lett.* **2019**, *19*, 6429−6434.

(13) Molesky, S.; Lin, Z.; Piggott, A. Y.; Jin, W.; Vucković, J.; Rodriguez, A. W. Inverse design in nanophotonics. *Nat. Photonics* **2018**, *12*, 659−670.

(14) Lassaline, N.; Brechbühler, R.; Vonk, S. J.; Ridderbeek, K.; Spieser, M.; Bisig, S.; le Feber, B.; Rabouw, F. T.; Norris, D. J. Optical Fourier surfaces. *Nature* **2020**, *582*, 506−510.

(15) Okawachi, Y.; Saha, K.; Levy, J. S.; Wen, Y. H.; Lipson, M.; Gaeta, A. L. Octave-spanning frequency comb generation in a silicon nitride chip. *Opt. Lett.* **2011**, *36*, 3398.

(16) Kippenberg, T. J.; Holzwarth, R.; Diddams, S. A. Microresonator-based optical frequency combs. *Science* **2011**, *332*, 555−559.

(17) Menezes, J. W.; Ferreira, J.; Santos, M. J.; Cescato, L.; Brolo, A. G. Large-area fabrication of periodic arrays of nanoholes in metal films and their application in biosensing and plasmonic-enhanced photovoltaics. *Adv. Funct. Mater.* **2010**, *20*, 3918−3924.

(18) Vecchi, G.; Giannini, V.; Gómez Rivas, J. Shaping the fluorescent emission by lattice resonances in plasmonic crystals of nanoantennas. *Phys. Rev. Lett.* **2009**, *102*, 2−5.

(19) Fradkin, I. M.; Dyakov, S. A.; Gippius, N. A. Nanoparticle lattices with bases: Fourier modal method and dipole approximation. *Phys. Rev. B* **2020**, *102*, 045432.

(20) Baur, S.; Sanders, S.; Manjavacas, A. Hybridization of Lattice Resonances. *ACS Nano* **2018**, *12*, 1618−1629.

(21) Abujetas, D. R.; Olmos-Trigo, J.; Sáenz, J. J.; Sánchez-Gil, J. A. Coupled electric and magnetic dipole formulation for planar arrays of particles: Resonances and bound states in the continuum for all-dielectric metasurfaces. *Phys. Rev. B* **2020**, *102*, 125411.

(22) Hsu, C. W.; Zhen, B.; Qiu, W.; Shapira, O.; DeLacy, B. G.; Joannopoulos, J. D.; Soljačić, M. Transparent displays enabled by resonant nanoparticle scattering. *Nat. Commun.* **2014**, *5*, 3152.

(23) Zundel, L.; May, A.; Manjavacas, A. Lattice Resonances Induced by Periodic Vacancies in Arrays of Nanoparticles. *ACS Photonics* **2021**, *8*, 360−368.

(24) Kuznetsov, A. I.; Miroshnichenko, A. E.; Brongersma, M. L.; Kivshar, Y. S.; Luk'yanchuk, B. Optically resonant dielectric nanostructures. *Science* **2016**, *354*. DOI: 10.1126/science.aag2472

(25) Wang, D.; Yang, A.; Hryn, A. J.; Schatz, G. C.; Odom, T. W. Superlattice Plasmons in Hierarchical Au Nanoparticle Arrays. *ACS Photonics* **2015**, *2*, 1789−1794.

(26) Kravets, V.; Schedin, F.; Grigorenko, A. Extremely narrow plasmon resonances based on diffraction coupling of localized plasmons in arrays of metallic nanoparticles. *Physical review letters* **2008**, *101*, 087403.

(27) Humphrey, A.; Barnes, W. Plasmonic surface lattice resonances in arrays of metallic nanoparticle dimers. *Journal of Optics* **2016**, *18*, 035005.

(28) Mahi, N.; Leveque, G.; Saison, O.; Marae-Djouda, J.; Caputo, R.; Gontier, A.; Maurer, T.; Adam, P.-M.; Bouhafs, B.; Akjouj, A. In depth investigation of lattice plasmon modes in substrate-supported gratings of metal monomers and dimers. *J. Phys. Chem. C* **2017**, *121*, 2388−2401.

(29) Cuartero-González, A.; Sanders, S.; Zundel, L.; Fernández-Domínguez, A. I.; Manjavacas, A. Super-and subradiant lattice resonances in bipartite nanoparticle arrays. *ACS Nano* **2020**, *14*, 11876−11887.

(30) Draine, B. T.; Flatau, P. J. Discrete-Dipole Approximation For Scattering Calculations. *Journal of the Optical Society of America A* **1994**, *11*, 1491.

(31) Zou, S.; Janel, N.; Schatz, G. C. Silver nanoparticle array structures that produce remarkably narrow plasmon lineshapes. *J. Chem. Phys.* **2004**, *120*, 10871−10875.

(32) Rayleigh, L. On the dynamical theory of gratings. *Proceedings of the Royal Society of London. Series A, Containing Papers of a Mathematical and Physical Character* **1907**, *79*, 399−416.

(33) Rodriguez, S. R.; Schaafsma, M. C.; Berrier, A.; Gómez Rivas, J. Collective resonances in plasmonic crystals: Size matters. *Physica B: Condensed Matter* **2012**, *407*, 4081−4085.

(34) Zundel, L.; Manjavacas, A. Finite-size effects on periodic arrays of nanostructures. *JPhys. Photonics* **2019**, *1*.015004

(35) Bin-Alam, M. S.; Baxter, J.; Awan, K. M.; Kiviniemi, A.; Mamchur, Y.; Lesina, A. C.; Tsakmakidis, K. L.; Huttunen, M. J.; Ramunno, L.; Dolgaleva, K. Hyperpolarizability of plasmonic meta-atoms in metasurfaces. *Nano Lett.* **2021**, *21*, 51−59.

(36) Boyd, R. W. *Nonlinear Opt.*; Academic Press: Cambridge, 2020.

(37) Koshelev, K.; Kruk, S.; Melik-Gaykazyan, E.; Choi, J. H.; Bogdanov, A.; Park, H. G.; Kivshar, Y. Subwavelength dielectric resonators for nonlinear nanophotonics. *Science* **2020**, *367*, 288−292.

(38) Huttunen, M. J.; Reshef, O.; Stolt, T.; Dolgaleva, K.; Boyd, R. W.; Kauranen, M. Efficient nonlinear metasurfaces by using multiresonant high-Q plasmonic arrays. *Journal of the Optical Society of America B* **2019**, *36*, No. E30.

(39) Bin-Alam, M. S.; Reshef, O.; Ahmad, R. N.; Upham, J.; Huttunen, M. J.; Dolgaleva, K.; Boyd, R. W. *Cross-polarized surface lattice resonances in a rectangular lattice plasmonic metasurface*. 2021, *2111*.02472, arXiv.org, DOI: 10.48550/arXiv.2111.02472 (accessed 2021/11/3).

(40) Lesina, A. C.; Vaccari, A.; Berini, P.; Ramunno, L. *FDTD method and HPC for large-scale computational nanophotonics*; Springer: Dordrecht, 2017.

(41) Mamin, H. J.; Rugar, D. Thermomechanical writing with an atomic force microscope tip. *Appl. Phys. Lett.* **1992**, *61*, 1003−1005.

(42) Dobrowolski, J. A.; Lowe, D. Optical thin film synthesis program based on the use of Fourier transforms. *Appl. Opt.* **1978**, *17*, 3039.

(43) Alaee, R.; Albooyeh, M.; Rockstuhl, C. Theory of metasurface based perfect absorbers. *J. Phys. D: Appl. Phys.* **2017**, *50*.503002

(44) Johnson, P. B.; Christy, R. W. Optical Constant of the Nobel Metals. *Phys. Rev. B* **1972**, *6*, 4370−4379.

(45) Schulz, S. A.; Upham, J.; Bouchard, F.; De Leon, I.; Karimi, E.; Boyd, R. W. Quantifying the impact of proximity error correction on plasmonic metasurfaces [Invited]. *Optical Materials Express* **2015**, *5*, 2798.

Supporting information for Fourier-Engineered Plasmonic Lattice Resonances

Theng-Loo Lim,[†] Yaswant Vaddi,[†] M. Saad Bin-Alam,[‡] Lin Cheng,[¶]
Rasoul Alaee,[†] Jeremy Upham,[†] Mikko J. Huttunen,[§] Ksenia Dolgaleva,[‡]
Orad Reshef,[*,†] and Robert W. Boyd[†,‖]

†*Department of Physics, University of Ottawa, 25 Templeton St, Ottawa, ON, K1N 6N5, Canada*

‡*School of Electrical Engineering and Computer Science, University of Ottawa, 25 Templeton St, Ottawa, ON, K1N 6N5, Canada*

¶*School of Instrument and Electronics, North University of China, Taiyuan, 030000, China*

§*Photonics Laboratory, Physics Unit, Tampere University, Korkeakoulunkatu 3, Tampere, FI-33014, Finland*

‖*Institute of Optics and Department of Physics and Astronomy, University of Rochester, 500 Wilson Blvd., Rochester, New York 14627, USA*

E-mail: orad@reshef.ca
Phone: +1 (613) 562-5800 Ext. 7138

Below is the supplementary information for Fourier-Engineered Plasmonic Lattice Resonances by Theng-Loo Lim, Yaswant Vaddi, M. Saad Bin-Alam, Lin Cheng, Rasoul Alaee, Jeremy Upham, Mikko J. Huttunen, Ksenia Dolgaleva, Orad Reshef, and Robert W. Boyd. It contains one section, in which we demonstrate multiple simulated transmission profiles for a series of FLR metasurfaces with different combinations of arbitrarily-selected resonance wavelengths.

Different combinations of selected wavelengths

In this section, we use the LSA to simulate FLR metasurfaces with several different combinations of selected wavelengths. These metasurfaces all consist of arrays of gold nanoparticles dimensions of 110 by 180 nm^2. These simulations prove the flexibility of the FLR method to design a variety of transmission profiles.

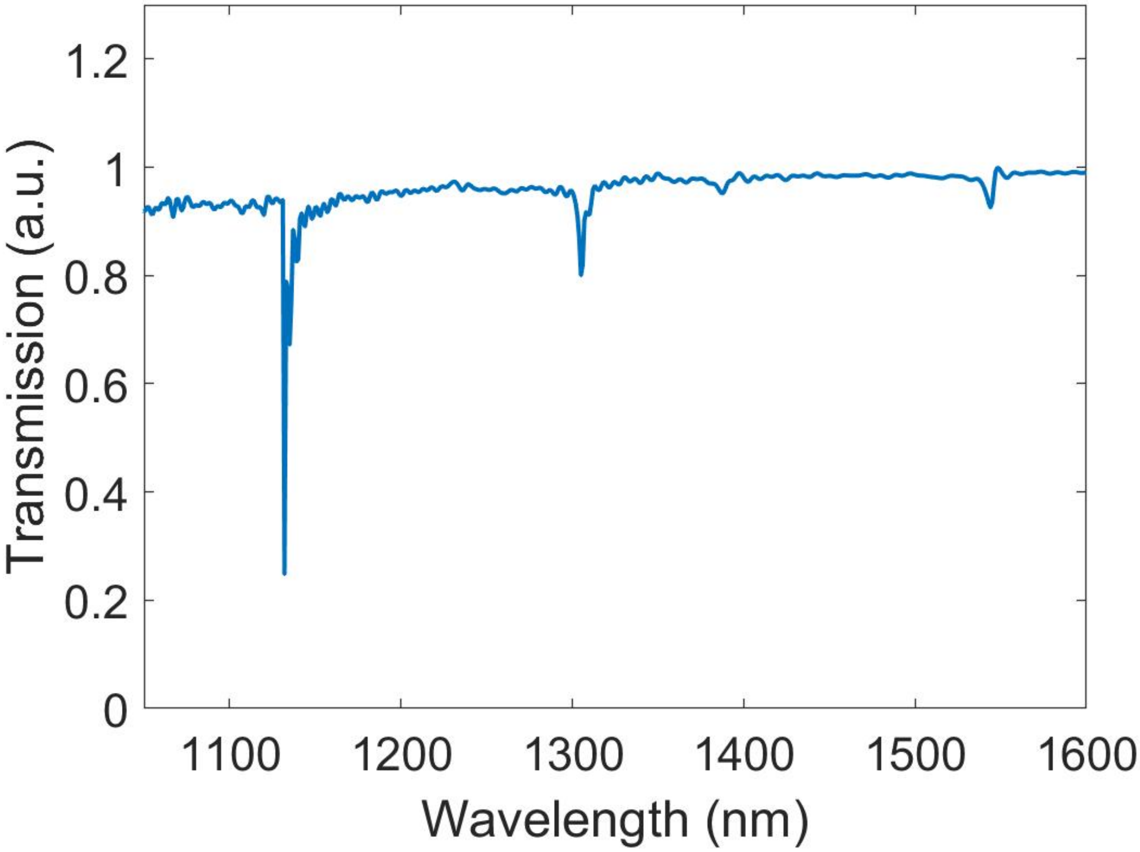

Figure 1: The selected wavelengths are 1134 nm, 1310 nm, and 1555 nm.

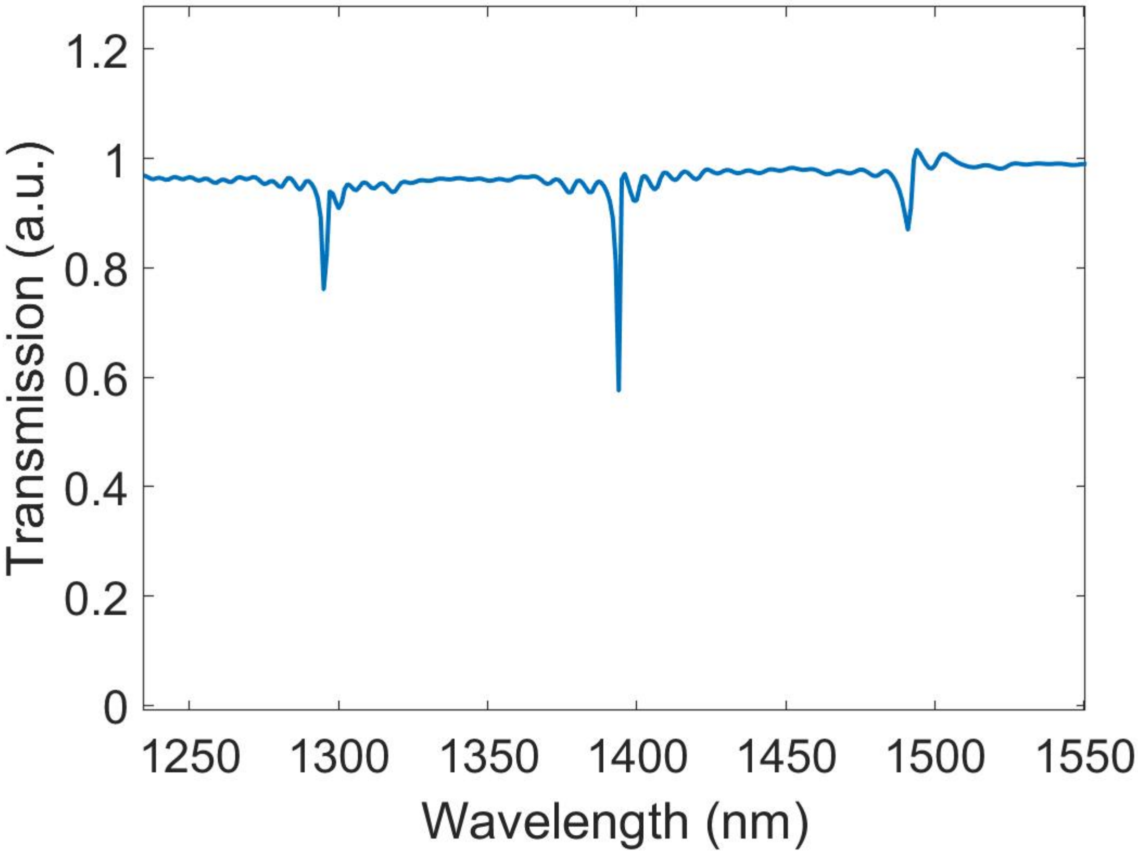

Figure 2: The selected wavelengths are 1300 nm, 1400 nm, and 1500 nm.

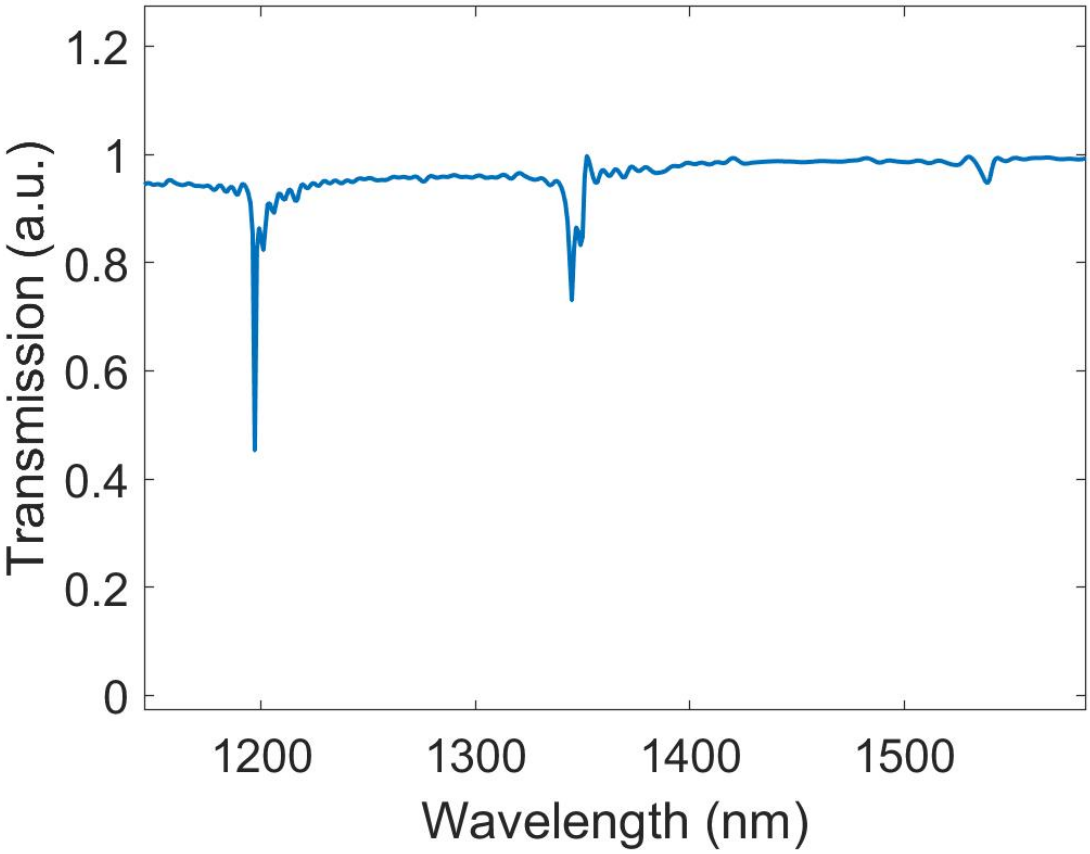

Figure 3: The selected wavelengths are 1200 nm, 1350 nm, and 1550 nm.

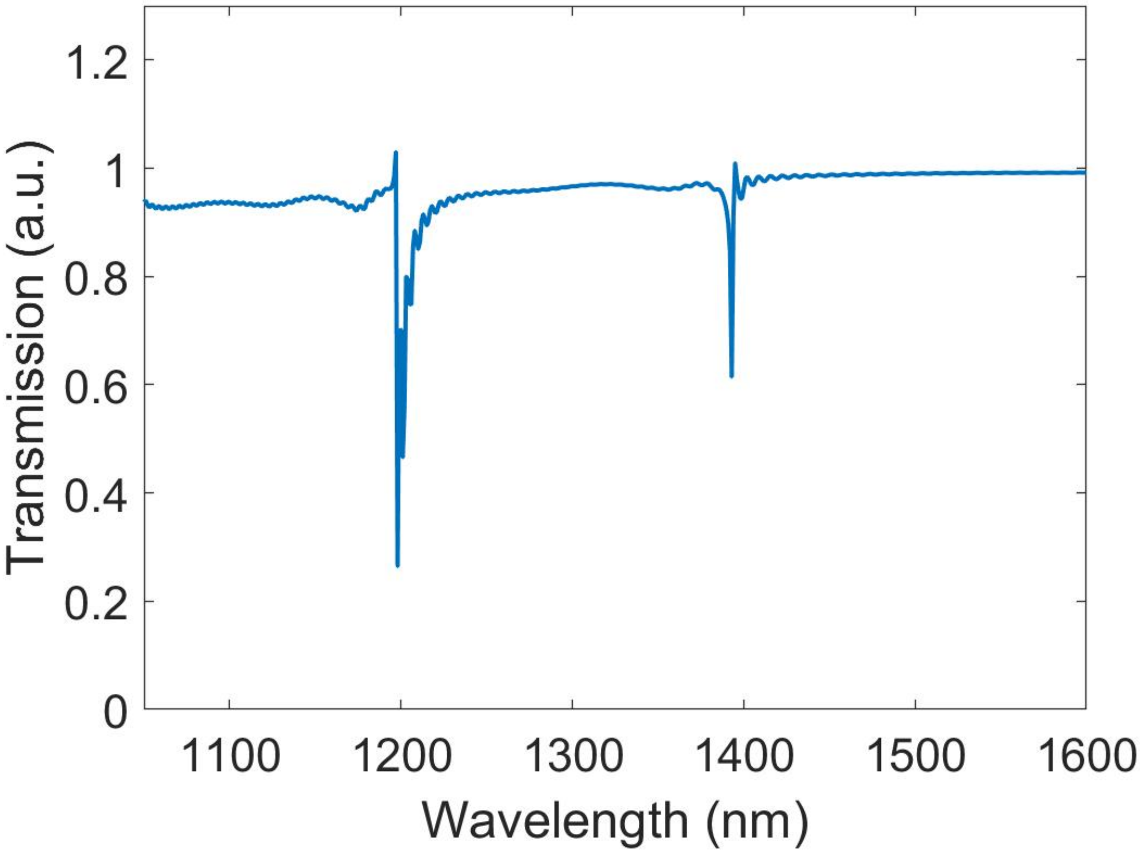

Figure 4: The selected wavelengths are 1200 nm, and 1400 nm.

Chapter 6

Conclusion and Future Works

This thesis has described my two research projects: energy transfer between two beams in an ENZ material based on adiabatic frequency conversion and developed an efficient metasurface design scheme where the desired resonance spectrum alone can determine the necessary metasurface design.

We first introduce the recent advances of unprecedentedly large optical nonlinearity and ultrafast time responses of ENZ materials, leading to significant time-varying effects such as AFC in Chapter 2. Using such materials, in Chapter 3 we have created a model for the energy transfer between two beams without the usual approaches of the beams having distinct frequencies or any external changes such as chirp, instead creating a model where the AFC generated by the significant nonlinearity of the ENZ material would be sufficient to produce significant two beam coupling. In other words, what we learned from this work that the laser beams themselves altered the refractive index of ITO, which caused AFC to occur and led to effective energy transfer. This approach to energy transfer is impossible for conventional materials such as fused silica but we demonstrated it experimentally in ITO. Using the mathematical treatment of TBC developed from Ref. [36], the extracted n_2 and β_2 are 1.1×10^{-3} cm^2/GW and -75 cm/GW, respectively, for the input intensity of 70 GW/cm^2. Our results are in good agreements with Ref. [7].

There are a several research topics building on this approach to TBC that could be investigated in the near future. For example, using AFC-induced TBC to boost the efficiency of ultrafast temporal hologram [41, 43]. Furthermore, this work provides a platform to study time-varying media, for which further exploration would necessarily take into account the self-manifesting TBC effect when considering multi-beam interactions even for the system that is chirp-free [68].

For Fourier-engineered plasmonic lattice resonance, the design scheme we introduced enables lattice resonance generation with flexible spectral position placings by having the nanoantenna placement be entirely dictated by the Fourier transform of the desired spectrum. In Chapter 4, we give an introduction to metasurfaces composed of plasmonic nanoantenna with different resonances including LSPR and SLR modes, motivating the potential for higher quality factors from the latter. We also introduced how such metasurfaces are fabricated and optically characterized. We also explored how multiple high Q SLRs in a single metasurface could be generated, motivating the need for metasurface designes that could independently position each resonance, and finally proposing our technique for doing so: the Fourrier lattice resonance technique.

Chapter 5 presented our published manuscript proposing and experimentally confirming our Fourier lattice resonance technique for designing metasurfaces entirely from the desired transmission spectrum. In this chapter, we have experimentally demonstrated this design scheme by fabricating the corresponding devices, and the experimental results are in excellent agreement with our LSA predictions. While other design methods could also enable near-arbitrary resonance placements, such as inverse-design [69] and full-FT design [70], these methods typically require labour-intensive design techniques [70], rather more complicated shapes of the nanoparticles [71], or advanced calculations methods [69]. Compared to the mentioned techniques, one of the advantages of our method is that our fabricated devices require only a standard fabrication procedure, and they can be easily expanded upon to generate multiple SLR modes that can be tuned nearly flexibly within a spectral octave. Furthermore, our method only required a single semi-analytical simulation process by combining the LSA model and FT anaylsis; thus, the simulation only requires a relatively short computation time compared to 3D full-wave FDTD simulations [69, 16].

Many future directions can be investigated based on our method. For example, our spectrum only considers the same extinction ratio for all desired resonances; we could investigate the effects induced by considering different extinction ratios. Moreover, we can study the overall electric field profiles of SLR modes with aperiodic lattices, and study SLR modes when different input field polarizations are applied. Also, we can include multilayer thin film stacks tuned by FT analysis [72] with our method, extending our method to 3D lattices using only semi-analytical method. Therefore, we anticipate that the FLR design method will have much potential to realize fully customizable metasurfaces for many optical applications.

In summary, we have studied exotic light-matter interactions in two different media: highly nonlinear thin films and artificial metasurfaces. Although the discussions in these two media are completely separated in this thesis, there are also many efforts to combine them and take advantage of both for some applications. For example, Ref. [41] coupled an LSPR mode with ENZ mode to boost the nonlinear change of refractive index despite high losses due to the low Q-factor of LSPR. We could investigate in a similar manner the coupling of SLR modes with an ENZ mode. Our FLR method could help to set an SLR wavelength of a metasurface at or near the ENZ wavelength of an ENZ thin film, leading to low-loss enhancement of this coupled system. This is just one possible example for such combined highly nonlinear, highly designable metasurfaces. We can envision that a broad range of similar ideas could be realized in the near future.

Appendix A

Appendix A: The mathematical description of two-beam coupling

In this appendix, we discuss the standard mathematical description of TBC in continuous-wave limit, which gives basic idea how one describe TBC effect. IT is closely followed Ref.[18]. We first consider the basic geometry shown in Fig. 2.7: assuming two beams with different wavelengths (ω_1, ω_2) interact and form an interference pattern on the surface of a nonlinear medium, resulting in a moving transient grating with a wavevector difference of q and a phase velocity δ, where $q = \; k_2 - k_1$ and $\delta = \; \omega_2 - \omega_1$. Thus, the total electric field can be shown as follows:

$$\tilde{E}(\mathbf{r}, t) = A_1 e^{i(\mathbf{k}_1 \cdot \mathbf{r} - \omega_1 t)} + A_2 e^{i(\mathbf{k}_2 \cdot \mathbf{r} - \omega_2 t)} + \text{c.c.}. \tag{A.1}$$

To determine the intensity distribution on the surface, if we know that intensity can be shown as:

$$I = n_0 \epsilon_0 c \left\langle \tilde{E}^2 \right\rangle, \tag{A.2}$$

substituting Eq. A.1 into Eq. A.2, we obtained the intensity distribution:

$$I = 2 n_0 \epsilon_0 c \left\{ A_1 A_1^* + A_2 A_2^* + \left[A_1 A_2^* e^{i(\mathbf{q} \cdot \mathbf{r} - \delta t)} + \text{ c.c. } \right] \right\}. \tag{A.3}$$

We are interested in the nonlinear index variation of the moving transient grating. If there is no instantaneous material time responses contribution to TBC effect, we then assume that nonlinear portion of the energy transfer between two beams follows Debye relaxation model:

$$\tau \frac{d n_{\text{NL}}}{dt} + n_{\text{NL}} = n_2 I, \tag{A.4}$$

where τ is the time response of a material. To solve this equation, one can use Green's function method, and obtain the following form for the nonlinear refractive index:

$$n_{\text{NL}} = 2 n_0 n_2 \epsilon_0 c \left[(A_1 A_1^* + A_2 A_2^*) + \frac{A_1 A_2^* e^{i(\mathbf{q} \cdot \mathbf{r} - \delta t)}}{1 - i \delta \tau} + \frac{A_1^* A_2 e^{-i(\mathbf{q} \cdot \mathbf{r} - \delta t)}}{1 + i \delta \tau} \right], \tag{A.5}$$

we now move onto determining the coupled-amplitude equation for TBC. we first consider wave equation:

$$\nabla^2 \tilde{E} - \frac{n^2}{c^2} \frac{\partial^2 \tilde{E}}{\partial t^2} = 0, \tag{A.6}$$

where the total refractive index, n, is taken into account of linear and nonlinear contribution:

$$n = n_0 + n_{NL}, \tag{A.7}$$

and

$$n^2 = n_0^2 + 2n_0 n_{NL} + n_{NL}^2, \tag{A.8}$$

where n_0 is a linear refractive index of a material and n_{NL} is a nonlinear refractive index variation of a material.

In this appendix, we show the TBC calculation with weak nonlinear contribution approximation, meaning that $n_{NL} << n_0$. This approximation works particularly well to the typical materials with weak nonlinearity.

A.1 TBC derivation with weak nonlinear refractive index approximation

For the typical materials, their nonlinear contribution is weak, thus we can assume that $n_{NL} << n_0$, and Eq. A.8 will be simplified as:

$$n^2 = n_0^2 + 2n_0 n_{NL}, \tag{A.9}$$

by substituting Eq. A.9 into the Eq. A.6, we will get portion of coupled-amplitude equation (we are only interested in A_2)

$$\begin{aligned} &\frac{d^2 A_2}{dz^2} + 2ik_2 \frac{dA_2}{dz} - k_2^2 A_2 + \frac{n_0^2 \omega_2^2}{c^2} A_2 \\ &= -\frac{4n_0^2 n_2 \omega_2^2 \epsilon_0}{c} \left(|A_1|^2 + |A_2|^2 \right) A_2 - \frac{4n_0^2 n_2 \omega_1^2 \epsilon_0}{c} \frac{|A_1|^2 A_2}{1 + i\delta\tau}, \end{aligned} \tag{A.10}$$

using slowly varying amplitude approximation, first term on the left-hand side of Eq. A.10 can be neglected. Furthermore, the third and fourth terms get cancelled with each other, leaving us with (we have also approximated ω_1 and ω_1 to be ω):

$$\frac{dA_2}{dz} = 2in_0 n_2 \omega \epsilon_0 \left[\left(|A_1|^2 + |A_2|^2 \right) A_2 + \frac{|A_1|^2 A_2}{1 + i\delta\tau} \right], \tag{A.11}$$

to calculate the spatial variation of Intensity, We use

$$\frac{dI_2}{dz} = 2n_0 \epsilon_0 c \left(A_2^* \frac{dA_2}{dz} + A_2 \frac{dA_2^*}{dz} \right), \tag{A.12}$$

Now, if we substitute Eq. A.11 and its complex conjugate in Eq. A.12, then we will get

$$\begin{aligned} \frac{1}{2n_0 \epsilon_0 c} \frac{dI_2}{dz} &= 2i\omega n_0 n_2 \epsilon_0 \left[|A_1|^2 + |A_2|^2 + \frac{|A_1|^2}{1 + i\delta\tau} \right] |A_2|^2 \\ &- 2i\omega n_0 n_2 \epsilon_0 \left[|A_1|^2 + |A_2|^2 + \frac{|A_1|^2}{1 - i\delta\tau} \right] |A_2|^2 , \end{aligned} \tag{A.13}$$

after simplifying Eq. A.13, we get

$$\frac{1}{2n_0\epsilon_0 c}\frac{dI_2}{dz} = 2i\omega n_0 n_2 \epsilon_0 \left[\frac{|A_1|^2}{1+i\delta\tau} - \frac{|A_1|^2}{1-i\delta\tau}\right]|A_2|^2, \tag{A.14}$$

and using $I_i = 2n_0\epsilon_0 c A_i A_i^*$, we will get

$$\frac{dI_2}{dz} = \frac{2n_2\omega}{c}\frac{\delta\tau}{1+\delta^2\tau^2}I_1 I_2. \tag{A.15}$$

Appendix B

Finite-difference time-domain method

Three-dimensional finite-difference time-domain (FDTD) is a well-known method to solve electrodynamics of a system numerically by discretizing Maxwell equation in time domain using central-difference approximation (sometimes it is referred to as Yee lattice) [57, 58]. We used a commercial FDTD software package, known as Lumerical FDTD solver, to calculate the transmission spectra for the targeted metasurface.

Figure B.1 shows an example of our FDTD simulation. The images are the software package interface; it typically shows the system layout from different views. First, the left panel of Fig. B.1 shows the X-Y view of a single unit cell. We defined an FDTD region and the rectangular particles with a mesh region (orange box) surrounding them. For the particles, we used gold as the material, and the material properties of gold are referred to Ref. [73]. The dimension of the FDTD region is equivalent to the periodicity of the lattice arrangement. We added a cladding layer because our sample is sputtered with a layer of glass, with the material properties defined by Ref. [73].

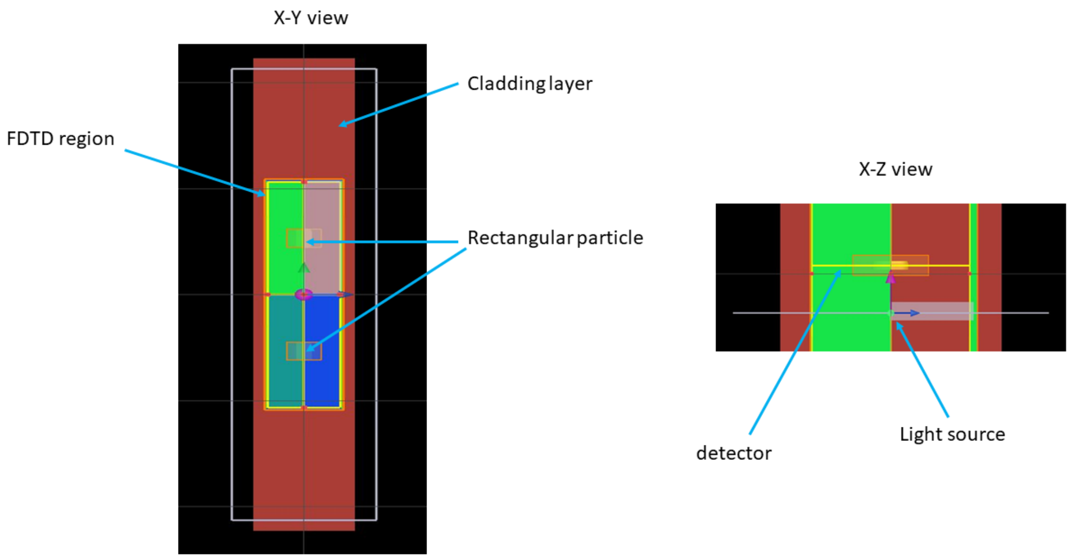

Figure B.1: Example of FDTD simulation for gold rectangular particles system.

The right panel of Fig. B.1 illustrates the X-Z view, we defined the light source as a plane wave source, and the source is set to be x-polarized. Finally, we installed a "detector" to record the transmission spectra of the system. We set periodic boundary conditions in the X-Y dimension; hence, the system is treated to have infinite array size. For the X-Z dimension, we set perfectly matched layers (PML). Minimal artificial absorption ($\mathrm{Im}(n) \approx 10^{-4}$) was added to the background medium to reduce numerical divergences. We then calculated transmission spectra of the periodic and modulated metasurfaces using this method.

Appendix C

Lattice Sum Approach

Lattice sum approach (LSA) is a simplified variant of discrete-dipole approximation (DDA) method [59, 60]. Therefore, we first consider the mathematical treatment of DDA (the treatment is closely followed Ref.[13, 74]). Lets assume that an array of N particles and an incident electric field, with a magnitude of E_0, interact with them. In this approximation, we only take into account dipole interaction, this the induced dipole electric field can be shown as:

$$\mathbf{P}_i(\omega) = \epsilon_0 \alpha_i(\omega) \mathbf{E}_{\text{loc},v} (v = 1, 2, \ldots, N), \tag{C.1}$$

where $\alpha_i(\omega)$ is the polarizability of the particle as a function of laser frequency,ω, and $E_{\text{loc},v}$ is the local electric field of a particle experienced by other N-1 dipoles. We can express the local electric field of a particle as:

$$\mathbf{E}_{\text{loc},v} = \mathbf{E}_{\text{inc},v} + \mathbf{E}_{\text{dipole},v} = \mathbf{E}_0 \exp\left(i\mathbf{k} \cdot \mathbf{r}_v\right) - \epsilon_0 \sum_{\substack{j=1 \\ j \neq v}}^{N} A_{vj} \cdot \mathbf{P}_j(\omega), \tag{C.2}$$

where r_{ij} is the position vector of dipole i and j, k is the wavevector of the incident field, and A is dipole interaction matrix. The last term of the equation can be described as:

$$\begin{aligned} A_{vj} \cdot \mathbf{P}_j(\omega) = k^2 \exp\left(ik \cdot r_{vj}\right) \frac{\mathbf{r}_{vj} \times \left(\mathbf{r}_{vj} \times \mathbf{P}_j(\omega)\right)}{r_{vj}^3} + \exp\left(ik \cdot r_{vj}\right) \\ \left(1 - ik \cdot r_{vj}\right) \frac{\left[r_{vj}^2 \mathbf{P}_j(\omega) - 3\mathbf{r}_{vj}\left(\mathbf{r}_{vj} \cdot \mathbf{P}_j(\omega)\right)\right]}{r_{vj}^5}, \end{aligned} \tag{C.3}$$

if we assumed that the array is infinite with identical particles, meaning that their polarizability is identical, we can solve equation C.3 analytically, and obtain:

$$\mathbf{P}(\omega) = \frac{\epsilon_0 \alpha(\omega) \mathbf{E}_0}{1 - \epsilon_0 \alpha(\omega) S(\omega)}, \tag{C.4}$$

where $S(\omega)$ is retarded dipole sum term:

$$S(\omega) = \sum_{j \neq v} \left[\frac{\left(1 - ikr_{vj}\right)\left(3\cos^2\theta_{vj} - 1\right) e^{ikr_{vj}}}{r_{vj}^3} + \frac{k^2 \sin^2\theta_{vj} e^{ikr_{vj}}}{r_{vj}} \right], \tag{C.5}$$

in LSA model, we assume that all dipoles are identical, which means that $v = j$, we can further simplified $S(\omega)$ to:

$$S(\omega) = \sum_{j=1}^{N} \frac{\exp\left(\mathrm{i}kr_j\right)}{\epsilon_0 r_j} \left[k^2 + \frac{\left(1 - \mathrm{i}kr_j\right)\left(3\cos^2\theta_j - 1\right)}{r_j^2} \right]. \tag{C.6}$$

This approximation has been proven that its accuracy in predicting properties of lattice resonance [14, 16, 13]. Furthermore, one of the main advantages of LSA method is that the computation time is much faster compared to a standard FDTD simulation with a superlattice element with periodic boundary conditions [16, 14].

Bibliography

[1] Nina Meinzer, William L Barnes, and Ian R Hooper. Plasmonic meta-atoms and metasurfaces. *Nature Photonics*, 8(12):889–898, 2014.

[2] Kirill Koshelev, Sergey Kruk, Elizaveta Melik-Gaykazyan, Jae-Hyuck Choi, Andrey Bogdanov, Hong-Gyu Park, and Yuri Kivshar. Subwavelength dielectric resonators for nonlinear nanophotonics. *Science*, 367(6475):288–292, 2020.

[3] Ashok Kodigala, Thomas Lepetit, Qing Gu, Babak Bahari, Yeshaiahu Fainman, and Boubacar Kanté. Lasing action from photonic bound states in continuum. *Nature*, 541(7636):196–199, 2017.

[4] Mohammadreza Khorasaninejad, Wei Ting Chen, Robert C Devlin, Jaewon Oh, Alexander Y Zhu, and Federico Capasso. Metalenses at visible wavelengths: Diffraction-limited focusing and subwavelength resolution imaging. *Science*, 352(6290):1190–1194, 2016.

[5] Shulin Sun, Kuang-Yu Yang, Chih-Ming Wang, Ta-Ko Juan, Wei Ting Chen, Chun Yen Liao, Qiong He, Shiyi Xiao, Wen-Ting Kung, Guang-Yu Guo, et al. High-efficiency broadband anomalous reflection by gradient meta-surfaces. *Nano letters*, 12(12):6223–6229, 2012.

[6] Nanfang Yu, Patrice Genevet, Mikhail A Kats, Francesco Aieta, Jean-Philippe Tetienne, Federico Capasso, and Zeno Gaburro. Light propagation with phase discontinuities: generalized laws of reflection and refraction. *science*, 334(6054):333–337, 2011.

[7] M Zahirul Alam, Israel De Leon, and Robert W Boyd. Large optical nonlinearity of indium tin oxide in its epsilon-near-zero region. *Science*, 352(6287):795–797, 2016.

[8] Yiyu Zhou, M Zahirul Alam, Mohammad Karimi, Jeremy Upham, Orad Reshef, Cong Liu, Alan E Willner, and Robert W Boyd. Broadband frequency translation through time refraction in an epsilon-near-zero material. *Nature communications*, 11(1):1–7, 2020.

[9] Sylvia Smolorz and Frank Wise. Femtosecond two-beam coupling energy transfer from raman and electronic nonlinearities. *JOSA B*, 17(9):1636–1644, 2000.

[10] J. Paul, M. Miscuglio, Y. Gui, V. J. Sorger, and J. K. Wahlstrand. Two-beam coupling by a hot electron nonlinearity. *Opt. Lett.*, 46(2):428–431, Jan 2021.

[11] Peter E Powers. Field guide to nonlinear optics. Society of Photo-Optical Instrumentation Engineers (SPIE), 2013.

[12] Mark W Knight, Lifei Liu, Yumin Wang, Lisa Brown, Shaunak Mukherjee, Nicholas S King, Henry O Everitt, Peter Nordlander, and Naomi J Halas. Aluminum plasmonic nanoantennas. *Nano letters*, 12(11):6000–6004, 2012.

[13] V. G. Kravets, A. V. Kabashin, W. L. Barnes, and A. N. Grigorenko. Plasmonic Surface Lattice Resonances: A Review of Properties and Applications. *Chemical Reviews*, 118(12):5912–5951, 2018.

[14] M Saad Bin-Alam, Orad Reshef, Yaryna Mamchur, M Zahirul Alam, Graham Carlow, Jeremy Upham, Brian T Sullivan, Jean-Michel Ménard, Mikko J Huttunen, and Robert W Boyd. Ultra-high-Q resonances in plasmonic metasurface. *Nature Communications*, 12:974, 2021.

[15] Ran Li, Marc R Bourgeois, Charles Cherqui, Jun Guan, Danqing Wang, Jingtian Hu, Richard D Schaller, George C Schatz, and Teri W Odom. Hierarchical hybridization in plasmonic honeycomb lattices. *Nano letters*, 19(9):6435–6441, 2019.

[16] Orad Reshef, Md Saad-Bin-Alam, Mikko J. Huttunen, Graham Carlow, Brian T. Sullivan, Jean Michel Ménard, Ksenia Dolgaleva, and Robert W. Boyd. Multiresonant High- Q Plasmonic Metasurfaces. *Nano Letters*, 19(9):6429–6434, 2019.

[17] Danqing Wang, Ankun Yang, Alexander J. Hryn, George C. Schatz, and Teri W. Odom. Superlattice Plasmons in Hierarchical Au Nanoparticle Arrays. *ACS Photonics*, 2(12):1789–1794, 2015.

[18] Robert W Boyd. *Nonlinear optics*. Academic press, 2020.

[19] Mike Melnichuk and Lowell T Wood. Direct kerr electro-optic effect in noncentrosymmetric materials. *Physical Review A*, 82(1):013821, 2010.

[20] John Kerr LL.D. Xl. a new relation between electricity and light: Dielectrified media birefringent. *The London, Edinburgh, and Dublin Philosophical Magazine and Journal of Science*, 50(332):337–348, 1875.

[21] PP Ho and RR Alfano. Optical kerr effect in liquids. *Physical Review A*, 20(5):2170, 1979.

[22] Orad Reshef, Israel De Leon, M. Zahirul Alam, and Robert W. Boyd. Nonlinear optical effects in epsilon-near-zero media, 2019.

[23] Wenshan Cai and Vladimir M Shalaev. *Optical metamaterials*, volume 10. Springer, 2010.

[24] Vladimir M. Shalaev, Wenshan Cai, Uday K. Chettiar, Hsiao-Kuan Yuan, Andrey K. Sarychev, Vladimir P. Drachev, and Alexander V. Kildishev. Negative index of refraction in optical metamaterials. *Opt. Lett.*, 30(24):3356–3358, Dec 2005.

[25] David Schurig, Jack J Mock, BJ Justice, Steven A Cummer, John B Pendry, Anthony F Starr, and David R Smith. Metamaterial electromagnetic cloak at microwave frequencies. *Science*, 314(5801):977–980, 2006.

[26] N I Landy, S Sajuyigbe, Jack J Mock, David R Smith, and Willie J Padilla. Perfect metamaterial absorber. *Physical review letters*, 100(20):207402, 2008.

[27] Yuandan Dong and Tatsuo Itoh. Metamaterial-based antennas. *Proceedings of the IEEE*, 100(7):2271–2285, 2012.

[28] Marta Gil, Jordi Bonache, and Ferran Martin. Metamaterial filters: A review. *Metamaterials*, 2(4):186–197, 2008.

[29] Hou-Tong Chen, Antoinette J Taylor, and Nanfang Yu. A review of metasurfaces: physics and applications. *Reports on progress in physics*, 79(7):076401, 2016.

[30] Guangyu Qiu, Zhibo Gai, Lanja Saleh, Jiukai Tang, Ting Gui, Gerd A Kullak-Ublick, and Jing Wang. Thermoplasmonic-assisted cyclic cleavage amplification for self-validating plasmonic detection of sars-cov-2. *ACS nano*, 15(4):7536–7546, 2021.

[31] M. Dressel. *Electrodynamics of solids: optical properties of electrons in matter*. Cambridge University Press, 2002.

[32] Yi Liu, Magali Durand, Shihua Chen, Aurélien Houard, Bernard Prade, Benjamin Forestier, and André Mysyrowicz. Energy exchange between femtosecond laser filaments in air. *Physical review letters*, 105(5):055003, 2010.

[33] BD Strycker, M Springer, C Trendafilova, X Hua, M Zhi, AA Kolomenskii, Hartmut Schröder, J Strohaber, Hans A Schüssler, GW Kattawar, et al. Energy transfer between laser filaments in liquid methanol. *Optics letters*, 37(1):16–18, 2012.

[34] A Dogariu, T Xia, DJ Hagan, AA Said, EW Van Stryland, and N Bloembergen. Purely refractive transient energy transfer by stimulated rayleigh-wing scattering. *JOSA B*, 14(4):796–803, 1997.

[35] Mark A Kramer, Wayne R Tompkin, and Robert W Boyd. Nonlinear-optical interactions in fluorescein-doped boric acid glass. *Physical Review A*, 34(3):2026, 1986.

[36] J-K Wang, T-L Chiu, C-H Chi, and C-K Sun. Nonlinear refraction and absorption measurements with chirped femtosecond laser pulses: experiments and simulations. *JOSA B*, 16(4):651–661, 1999.

[37] Gauri N Patwardhan, Jared S Ginsberg, Cecilia Y Chen, M Mehdi Jadidi, and Alexander L Gaeta. Nonlinear refractive index of solids in mid-infrared. *Optics Letters*, 46(8):1824–1827, 2021.

[38] Andrew Weiner. *Ultrafast optics*, volume 72. John Wiley & Sons, 2011.

[39] Inuk Kang, Todd Krauss, and Frank Wise. Sensitive measurement of nonlinear refraction and two-photon absorption by spectrally resolved two-beam coupling. *Optics letters*, 22(14):1077–1079, 1997.

[40] M. Zahirul Alam, Israel De Leon, and Robert W. Boyd. Large optical nonlinearity of indium tin oxide in its epsilon-near-zero region. *Science*, 352(6287):795–797, 2016.

[41] M Zahirul Alam, Sebastian A Schulz, Jeremy Upham, Israel De Leon, and Robert W Boyd. Large optical nonlinearity of nanoantennas coupled to an epsilon-near-zero material. *Nature Photonics*, 12(2):79–83, 2018.

[42] Junhong Deng, Yutao Tang, Shumei Chen, Kingfai Li, Anatoly V Zayats, and Guixin Li. Giant enhancement of second-order nonlinearity of epsilon-near-zero medium by a plasmonic metasurface. *Nano Letters*, 20(7):5421–5427, 2020.

[43] Takeo Sasaki, Masashi Ikegami, Tatsuya Abe, Daisuke Miyazaki, Satoshi Kajikawa, and Yumiko Naka. Real-time dynamic hologram in photorefractive ferroelectric liquid crystal with two-beam coupling gain coefficient of over 800 cm–1 and response time of 8 ms. *Applied Physics Letters*, 102(6):31, 2013.

[44] Eliza Hutter and Janos H. Fendler. Exploitation of localized surface plasmon resonance. *Advanced Materials*, 16(19):1685–1706, 2004.

[45] Stefan Alexander Maier. *Plasmonics: fundamentals and applications.* Springer Science & Business Media, 2007.

[46] S. J. Oldenburg, R. D. Averitt, S. L. Westcott, and N. J. Halas. Nanoengineering of optical resonances. *Chemical Physics Letters*, 288(2-4):243–247, 1998.

[47] Sozo Yokogawa, Stanley P. Burgos, and Harry A. Atwater. Plasmonic color filters for CMOS image sensor applications. *Nano Letters*, 12(8):4349–4354, 2012.

[48] Beibei Zeng, Yongkang Gao, and Filbert J. Bartoli. Ultrathin nanostructured metals for highly transmissive plasmonic subtractive color filters. *Scientific Reports*, 3:2840, 2013.

[49] Stefano Palomba, Matthias Danckwerts, and Lukas Novotny. Nonlinear plasmonics with gold nanoparticle antennas. *Journal of Optics A: Pure and Applied Optics*, 11(11), 2009.

[50] Guangyu Qiu, Zhibo Gai, Lanja Saleh, Jiukai Tang, Ting Gui, Gerd A. Kullak-Ublick, and Jing Wang. Thermoplasmonic-Assisted Cyclic Cleavage Amplification for Self-Validating Plasmonic Detection of SARS-CoV-2. *ACS Nano*, 15(4):7536–7546, 2021.

[51] Brock Doiron, Mónica Mota, Matthew P. Wells, Ryan Bower, Andrei Mihai, Yi Li, Lesley F. Cohen, Neil Mc N. Alford, Peter K. Petrov, Rupert F. Oulton, and Stefan A. Maier. Quantifying Figures of Merit for Localized Surface Plasmon Resonance Applications: A Materials Survey. *ACS Photonics*, 6(2):240–259, 2019.

[52] Baoqing Wang, Peng Yu, Wenhao Wang, Xutao Zhang, Hao-Chung Kuo, Hongxing Xu, and Zhiming M Wang. High-q plasmonic resonances: Fundamentals and applications. *Advanced Optical Materials*, 9(7):2001520, 2021.

[53] P.R. West, S. Ishii, G.V. Naik, N.K. Emani, V.M. Shalaev, and A. Boltasseva. Searching for better plasmonic materials. *Laser & Photonics Reviews*, 4(6):795–808, 2010.

[54] Svetlana V. Boriskina, Thomas Alan Cooper, Lingping Zeng, George Ni, Jonathan K. Tong, Yoichiro Tsurimaki, Yi Huang, Laureen Meroueh, Gerald Mahan, and Gang Chen. Losses in plasmonics: from mitigating energy dissipation to embracing loss-enabled functionalities. *Adv. Opt. Photon.*, 9(4):775–827, Dec 2017.

[55] Rupert F Oulton. Loss and gain. *Nature Photonics*, 6(4):219–221, 2012.

[56] Anton D. Utyushev, Vadim I. Zakomirnyi, and Ilia L. Rasskazov. Collective lattice resonances: Plasmonics and beyond. *Reviews in Physics*, 6(January):100051, 2021.

[57] Dennis M Sullivan. *Electromagnetic simulation using the FDTD method.* John Wiley & Sons, 2013.

[58] Stephen D Gedney. Introduction to the finite-difference time-domain (fdtd) method for electromagnetics. *Synthesis Lectures on Computational Electromagnetics*, 6(1):1–250, 2011.

[59] Bruce T. Draine and Piotr J. Flatau. Discrete-Dipole Approximation For Scattering Calculations. *Journal of the Optical Society of America A*, 11(4):1491, 1994.

[60] Shengli Zou, Nicolas Janel, and George C. Schatz. Silver nanoparticle array structures that produce remarkably narrow plasmon lineshapes. *Journal of Chemical Physics*, 120(23):10871–10875, 2004.

[61] Yoshitomo Okawachi, Kasturi Saha, Jacob S. Levy, Y. Henry Wen, Michal Lipson, and Alexander L. Gaeta. Octave-spanning frequency comb generation in a silicon nitride chip. *Optics Letters*, 36(17):3398, 2011.

[62] T. J. Kippenberg, R. Holzwarth, and S. A. Diddams. Microresonator-based optical frequency combs. *Science*, 332(6029):555–559, 2011.

[63] Jacson W. Menezes, Jacqueline Ferreira, Marcos J.L. Santos, Lucila Cescato, and Alexandre G. Brolo. Large-area fabrication of periodic arrays of nanoholes in metal films and their application in biosensing and plasmonic-enhanced photovoltaics. *Advanced Functional Materials*, 20(22):3918–3924, 2010.

[64] G. Vecchi, V. Giannini, and J. Gómez Rivas. Shaping the fluorescent emission by lattice resonances in plasmonic crystals of nanoantennas. *Physical Review Letters*, 102(14):2–5, 2009.

[65] Chia Wei Hsu, Bo Zhen, Wenjun Qiu, Ofer Shapira, Brendan G. DeLacy, John D. Joannopoulos, and Marin Soljačić. Transparent displays enabled by resonant nanoparticle scattering. *Nature Communications*, 5:3152, 2014.

[66] Lauren Zundel, Asher May, and Alejandro Manjavacas. Lattice resonances induced by periodic vacancies in arrays of nanoparticles. *ACS Photonics*, 8(1):360–368, 2021.

[67] Mikko J Huttunen, Orad Reshef, Timo Stolt, Ksenia Dolgaleva, Robert W Boyd, and Martti Kauranen. Efficient nonlinear metasurfaces by using multiresonant high-q plasmonic arrays. *JOSA B*, 36(7):E30–E35, 2019.

[68] Emanuele Galiffi, Romain Tirole, Shixiong Yin, Huanan Li, Stefano Vezzoli, Paloma A Huidobro, Mário G Silveirinha, Riccardo Sapienza, Andrea Alù, and JB Pendry. Photonics of time-varying media. *Advanced Photonics*, 4(1):014002, 2022.

[69] Sean Molesky, Zin Lin, Alexander Y Piggott, Weiliang Jin, Jelena Vucković, and Alejandro W Rodriguez. Inverse design in nanophotonics. *Nature Photonics*, 12(11):659–670, 2018.

[70] Nolan Lassaline, Raphael Brechbühler, Sander J.W. Vonk, Korneel Ridderbeek, Martin Spieser, Samuel Bisig, Boris le Feber, Freddy T. Rabouw, and David J. Norris. Optical Fourier surfaces. *Nature*, 582(7813):506–510, 2020.

[71] Alexander Y Piggott, Jesse Lu, Konstantinos G Lagoudakis, Jan Petykiewicz, Thomas M Babinec, and Jelena Vučković. Inverse design and demonstration of a compact and broadband on-chip wavelength demultiplexer. *Nature Photonics*, 9(6):374–377, 2015.

[72] J. A. Dobrowolski and D. Lowe. Optical thin film synthesis program based on the use of Fourier transforms. *Applied Optics*, 17(19):3039, 1978.

[73] P. B. Johnson and R. W. Christy. Optical Constant of the Nobel Metals. *Physical Review B*, 6(12):4370–4379, 1972.

[74] Shengli Zou, Nicolas Janel, and George C. Schatz. Silver nanoparticle array structures that produce remarkably narrow plasmon lineshapes. *The Journal of Chemical Physics*, 120(23):10871–10875, 2004.